Cavity Cooling of Leptons for Increased Antihydrogen Production at ALPHA

by

Nathan Evetts

B.Sc., The University of British Columbia, 2011

A THESIS SUBMITTED IN PARTIAL FULFILLMENT OF
THE REQUIREMENTS FOR THE DEGREE OF

MASTER OF SCIENCE

in

The Faculty of Graduate and Postdoctoral Studies

(Physics)

THE UNIVERSITY OF BRITISH COLUMBIA

(Vancouver)

August 2015

Abstract

Precise spectroscopic measurements of anti-hydrogen at the ALPHA experiment are hindered by small numbers of cold anti-atoms. This thesis describes a cooling technique for positron plasmas which can be used to increase the number of trappable anti-hydrogen atoms. The technique builds on previous work which allows control of spontaneous emission via the Purcell Effect. Our implementation incorporates a novel microwave resonator into an existing Penning trap to enhance spontaneous emission. Preliminary data suggests that temperatures and cooling rates for these plasmas can be improved by at least a factor of 10. Eventually this work could result in an order of magnitude increase in anti-hydrogen production at ALPHA

Preface

Chapter 7 details measurements of electron plasma temperatures and cooling rates at resonances within the cavity presented in chapter 3. The data presented in chapter 7 was taken primarily by Eric Hunter at Berkeley. The plasma apparatus (with the exception of the cavity) was built and maintained by Alex Povilus at Berkeley.

The cavity was conceptualized at the University of British Columbia by Walter Hardy. Later I designed, simulated and characterized the cavity presented in this thesis.

The electro-deposition (described in section 3.4) of a nichrome-like alloy onto the cavity was conducted by Isaac Martens.

The nuclear magnetic resonance measurements of chapter 6 were performed by Carl Michal.

Table of Contents

Appendices

List of Tables

List of Figures

Acknowledgements

A special thanks to my supervisor, Prof. Walter Hardy. I learned a great deal from Walter. In particular I am grateful for his willingness to "get his hands dirty" working on new, possibly crazy ideas. Without his support none of this work would be possible.

Thanks also to Makoto Fujiwara for consistent support (both moral and financial). Makoto displayed a quiet confidence in this project and in me which called out for success.

Finally I'd like to acknowledge the Berkeley crowd: Alex Povilus, Eric Hunter, and Joel Fajans have all worked long and hard on this collaboration. Without them, we would not have a plasma experiment!

Chapter 1

Introduction

1.1 Antimatter

At the time of the big bang when the universe was very hot and very dense, matter-antimatter particle pairs are believed to have been created in abundance and to have eventually cooled to produce today's observable universe. This paradigm has the fundamental problem of predicting a universe populated with equal parts matter and antimatter. The postulate remains in stark contrast with our matter dominated universe and has posed a mystery which cries out for investigation.

Formally the equivalence of matter and antimatter is expressed via the CPT theorem. CPT symmetry states that any local Lorentz-invariant quantum field theory is invariant under combined operations of charge-conjugation (C), parity (P), and time-reversal (T) [38]. Antimatter is what results when these operations are performed on matter. Every particle, therefore, has an antimatter counter particle with identical mass but opposite charge and spin. The invariant nature of the symmetry would demand that the physics of a pure antimatter system be identical to that of its matter analogue. In essence, the goal of the ALPHA experiment is to observe a violation of this symmetry. That is, we are attempting to detect a difference between antimatter and matter, or at least to place constraints on possible differences.

Our chosen antimatter system is anti-hydrogen: the bound state of a positron (anti-electron) to an anti-proton. Multiple measurements on other antimatter systems have already been made and place upper bounds on the possible discrepancies between certain quantities (for examples, see table 1.1).[1]

Hydrogen, however, has the advantage that it is a very simple, neutral system. As a result spectroscopic properties of hydrogen have been measured

[1] Signals of CPT violation have also been observed in the cosmic microwave background (CMB) at 2σ [23] and by the BaBar collaboration using $\overline{B^o} - B^o$ oscillations at 2.2σ [15].

to extremely high precision. The most promising measurements are the 1S - 2S transition (which has been done to a relative precision of 4.2×10^{-15} [45]), and the ground state hyperfine splitting (with a relative precision of 10^{-12} [31]).

	Quantity	Relative precision	Absolute Energy Difference	Reference
$\overline{K^o} - K^o$	mass	4×10^{-18}	300 kHz	[3]
e^+-e	mass	8×10^{-9}	0.9 THz	[22]
	charge	4×10^{-8}	-	[32]
	gyromagnetic moment	2.1×10^{-12}	-	[54]
$\bar{p} - p$	mass	7×10^{-10}	159 THz	[16]
	charge	7×10^{-10}	-	[16]

Table 1.1: A summary of matter-antimatter measurements. Where applicable I have included absolute energy difference (in frequency units) since it has been argued to be the relevant figure of merit [6] rather than the relative precision.

ALPHA is not likely to reach these precisions any-time soon, however a first step towards hyperfine spectroscopy has been taken in 2012 when the spin of antihydrogen atoms was likely flipped [18]. Since demonstrating an ability to trap ground state antihydrogen atoms for long periods of time (up to 15 minutes) [20, 19], the ALPHA apparatus has been modified to incorporate laser windows for optical spectroscopy. In particular 1S-2S, 1S-2P and hyperfine spectroscopy measurements are being pursued. All of these measurements, however, are greatly hindered by the small number of antiatoms which can be trapped. Typically only one or two atoms are contained at any given time!

The goal of this work is to demonstrate a cooling technique which can alleviate this problem by increasing the number of trappable antihydrogen atoms at ALPHA.

1.2 Thesis overview

This chapter is intended to provide background, motivation, and context for the work of this thesis. The backdrop is, of course, antimatter measure-

ments, CPT violation and the ALPHA experiment. Section 1.1 provides a terse summary of antimatter mysteries and measurements. Section 1.3 will give a very brief overview of the ALPHA apparatus and the antihydrogen production procedure.

Chapter 2 is an overview of the Purcell effect. At heart a method for resonantly enhancing a spontaneous emission rate, this effect is the foundation on which our proposed cooling technique is built. The original theoretical framework as presented by Purcell is given and many of the original experiments are discussed. This chapter also characterizes a failed 2011 search for spontaneous emission enhancement at ALPHA. Finally, our own classical model of the Purcell effect, specific to the case of a positron in cyclotron motion, is developed and predictions about possible cooling enhancements are made.

Chapter 3 describes a novel microwave resonator designed for compatibility with a Penning trap. Resonator design considerations are presented along with cavity resonance characterization both via numerical simulation and observation. Considerations for enhancing the cooling power of this resonator with unique surface preparations are detailed.

Chapter 4 models many body effects unique to this refrigerative implementation of the Purcell effect. Namely, if there are too many particles radiating energy into our cavity, its refrigeration powers will be diminished. This is a many body problem in the vicinity of a resonance. Numerical results are shown from systems of a few particles up to a few hundred particles. The results are extrapolated in order to make predictions about the maximum number of particles our technique is capable of cooling.

Chapter 5 describes a "laser pass - microwave filter" device we have constructed. This filter is designed with a tubular geometry intended to allow laser access to antihydrogen trapping regions while attenuating unwanted microwave radiation which might cause heating of the positron plasma.

Chapter 6 describes measurements which characterize the magnetic properties of the ALPHA Penning trap electrodes.

Chapter 7 presents preliminary data which confirms our assertion that positrons can be cooled via the Purcell effect.

1.3 ALPHA apparatus

The ALPHA apparatus is, at its heart, a Penning trap superimposed with a magnetic minimum trap. The Penning trap is an apparatus for controlling charged particles: positrons and antiprotons. Once these are mixed and (neutral) antihydrogen is formed, a magnetic minimum trap is used to contain the antiatom(s).

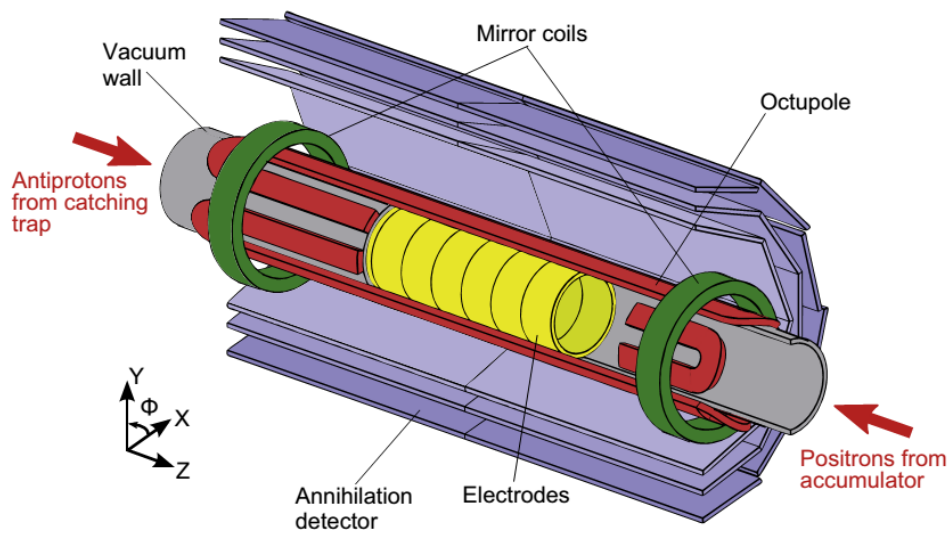

Figure 1.1: The Penning trap of the ALPHA apparatus is shown surrounded by Octupole and mirror coils which impose a magnetic minimum trap for anti atoms. Also shown is the silicon detector used to reconstruct annihilation events. Figure adapted from [2].

Antiprotons are created by colliding high energy protons on an iridium target. The antiprotons produced by these collisions are decelerated to energies of $\simeq 5.3$ MeV by a facility called the Antiprotron Decelerator (AD) [39]. These low energy antiprotons are shared between a number of antimatter and antihydrogen experiments which have developed around this unique facility. At ALPHA we direct antiprotons from the AD into a dedicated

Penning trap (called the "catching trap") where they are cooled, both sympathetically by an electron plasma and, afterwards by evaporation. Once cooled, antiprotons are transferred to the "mixing trap" shown in figure 1.1.

Positrons are emitted via beta decay from a radioactive sodium-22 source. A Surko-type positron accumulator [43] stores these positrons for injection into the mixing trap.

Once both antiprotons and positrons are in the same central Penning trap, the two species are mixed using a technique called auto-resonant mixing [17]. The technique is tuned to mix the particles while heating them minimally. During mixing antihydrogen forms, likely through three body collisions [49] between two positrons and one antiproton.

Most of the antiatoms which are created in this manner likely annihilate on the inner wall of the Penning trap. However, those in either of the upper two spin states, with a kinetic energy less than about 0.5 K can be trapped. (The trap depth is set by the strength of the octupole magnetic field at the Penning trap wall: Antiatoms with enough energy to reach higher fields will annihilate here and be lost.)

The ALPHA apparatus in its entirety is an extremely complex device and many important aspects have been left out of this description. Some of the omitted subsystems include: particle detectors (silicon, caesium-iodide, plastic scintillators); plasma diagnostics (faraday cup, micro-channel plates, phosphor screens); vacuum and cryogenics; microwave equipment, lasers and optics. Greater detail can be found in [2, 41].

1.4 The Penning trap

Because of its central importance to both the ALPHA experiment and the present work, a more detailed overview of the Penning trap is provided here.

The Penning trap is merely a segmented hollow metal tube which traps charged particles using static electric and magnetic fields. Each segment, or electrode, of the tube is electrically isolated from all the others. This isolation allows each electrode to be held at a different voltage. To trap positrons, for example, a central electrode (or group of electrodes) is held at some low voltage (ground in figure 1.2) while outer electrodes are held at high voltage. If the potential energy “hill” provided by the end electrodes is high enough, particles will be axially confined.

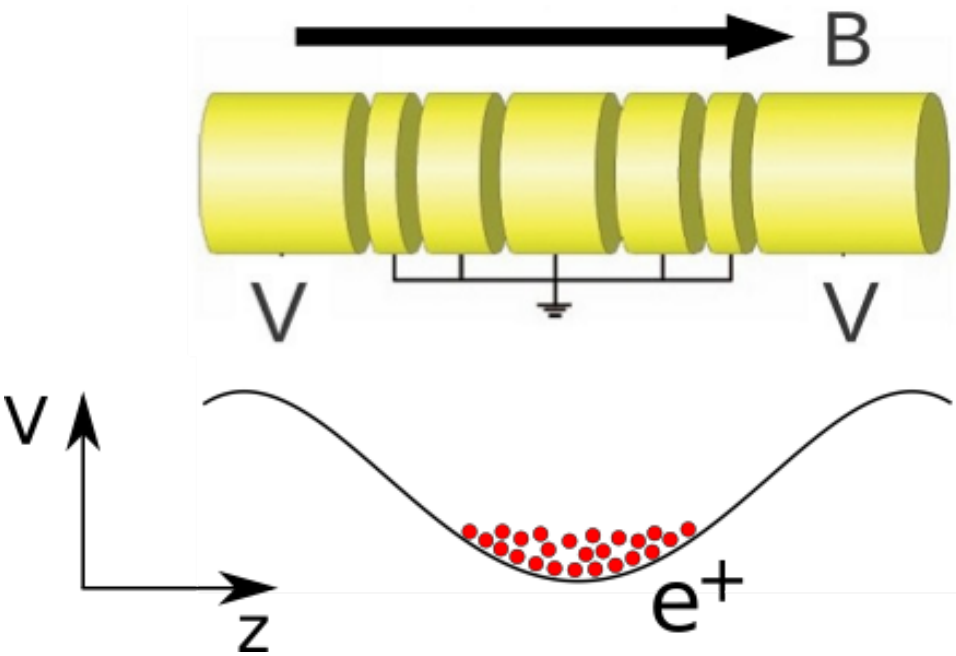

Figure 1.2: A sketch of a Penning trap which contains positrons axially via electrostatic forces. Figure adapted from [10].

To obtain 3-dimensional confinement, a large axial magnetic field is applied. This field imposes a centripetal Lorentz force:

$$F = q\vec{v} \times \vec{B} \tag{1.1}$$

which causes the charged particles to oscillate in a circular motion (cyclotron motion) as in figure 1.3. [2]

Because these charged particles are accelerating, they are also radiating. This radiation is the primary cooling mechanism for positron plasmas at ALPHA. Until very recently [3] the positron temperatures were typically 50 - 100 K. Speculation is that radiative heating from objects in poor thermal contact with the cryostat, electronic noise, and/or magnetic field inhomogeneities could prevent positrons from reaching temperatures set by the Penning trap wall at $\simeq 7 - 10$ K.

[2] A "magnetron" motion, where the plasma as a whole, spins about its axis, is also present in trapped plasmas, though not discussed in this thesis.

[3] Near the end of 2014, ALPHA saw positrons with temperatures as low as 30 K.

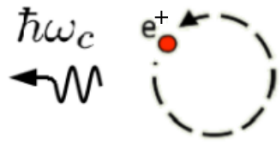

Figure 1.3: An axial magnetic field imposes a centripetal force which causes circular motion. Radiation is emitted at the cyclotron frequency.

A competition between these heating mechanisms with cooling due to radiation sets the positron temperature. In this light, Chapter 3 will point out that a cavity can reduce the equilibrium positron temperature on two fronts. First the cooling rate will be greatly enhanced. Second, radiative heating can be reduced since photons from warm external objects tend not to couple into the cavity. In the absence of any other heating mechanisms, the positrons would cool to the temperature of the Penning trap electrodes.

Chapter 2

Overview of the Purcell Effect

2.1 Theory and history

The historical beginnings of this work lie in a 1946 abstract for a paper published by Purcell [1]. Purcell noted that nuclear magnetic resonance (NMR) transitions could be enhanced by a large factor if the sample under measurement is coupled to a resonant circuit [4]. In that work Purcell pointed out that the decay rate of some excited state $|i>$ to some lower state $|f>$ is modified under this resonant coupling. This decay rate is expressed according to Fermi's Golden rule as

$$\Gamma = 2\pi\rho(E)\frac{|<f|H|i>|^2}{\hbar} \tag{2.1}$$

where H is a perturbing Hamiltonian; $\rho(E)$ is the density of states at energy $E_f - E_i = h\nu$, for frequency ν; and where $2\pi\hbar$ is Plank's constant.

If an excited state of some system decays in a free space environment, the density of states for the emitted photon is $8\pi\nu^2/c^3$. In the case of coupling to a resonator, however, there now exists only *one* state in the frequency bandwidth of the resonator $\Delta\omega$. The enhancement factor Purcell derived is

$$\frac{3Q\lambda^3}{4\pi^2 V} \tag{2.2}$$

where λ is the resonant wavelength of radiation emitted by NMR transitions, Q is the resonator quality factor and V is the resonator volume.

Decades later, Kleppner [37] would elucidate a physical interpretation for this effect: that the resonator has enhanced vacuum field fluctuations at the resonant frequency (ν) which "stimulate" spontaneous emission. Indeed the state transition frequency must be matched to a resonance of the environment for *enhancement* to occur. If the emission frequency is off resonance the density of states approaches zero and spontaneous emission can be greatly *inhibited*.

[4] In NMR this effect is usually termed "radiation damping" [4].

Environments inhibiting and enhancing spontaneous emission are sketched qualitatively in figure 2.1 alongside a free space environment. Both inhibited and enhanced spontaneous emission have been observed across a number of diverse systems throughout the 1980's. These experiments (to be discussed further in the next section) involve electron plasmas, Rydberg atoms, semiconductor devices and dye molecules.

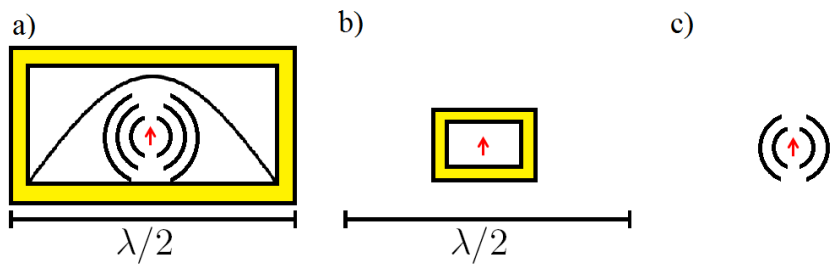

Figure 2.1: Three separate environments are sketched. a) shows a metallic two dimensional box which constrains the density of states for photons emitted from a radiating dipole (red arrow). If the electromagnetic resonance frequency of the box is tuned to the characteristic emission frequency of the dipole, spontaneous emission is enhanced. b) Shows the same dipole in a box significantly smaller than the resonant wavelength. No states exist for photons at this frequency and the dipole will not emit. c) Free space boundary conditions allow the dipole to emit "normally".

Although not the focus of this thesis, it would be imprudent to omit two other main features of this theoretical framework. Firstly, in addition to affecting the spontaneous emission rate of a multi-state system, a cavity also affects the energy levels of that system. That is, the energies of states $|i>$ and $|f>$ when coupled to a cavity are different than in free space. Fortunately (for this work) the energy shift is a higher order effect which can be ignored when one is solely interested in the decay rate, Γ.

Secondly, and more importantly, all these cavity effects fall under the larger branch of what is now known as Cavity Quantum Electrodynamics, or Cavity QED. Cavity QED represents a large and interesting field in its own right. While emission rate and energy level shifts typically occur under weak cavity coupling, the strong coupling regime offers an even richer variety of physics. Under strong coupling, cavity photons can become entangled with a matter system. These systems offer opportunities for tests of quantum mechanics, quantum non-demolition measurements, and potential

applications in quantum information [56]. Most of cavity QED, however, lies beyond the scope of this thesis and will not be considered further.

Finally, applications of the Purcell effect are also widespread in solid state systems where device performance is often limited by spontaneous emission. Much work been done to improve these limits using cavities or cavity-like structures [62].

2.2 Some experiments

Although the first experiment was actually performed with dye molecules [13], experimental Cavity QED has largely resided within the realms of atomic and solid state physics. This section will therefore provide a brief review of experiments from these fields which demonstrate control of spontaneous emission before moving on to the context of lepton plasmas with which we are primarily concerned. For a more comprehensive review see [56].

2.2.1 Rydberg atoms

In 1981 Kleppner first proposed that Rydberg atoms would make good candidates for observations of spontaneous emission control [37]. Rydberg atoms were attractive candidates since transitions between closely spaced energy levels would produce resonance frequencies of hundreds of GHz. This meant that the wavelength of the emitted radiation would be on the scale of μm or mm and that cavities could therefore be easily constructed to constrain or enhance this radiation. The environment Kleppner proposed was a waveguide in the vicinity of cut-off.

Given that the mode structure of waveguides is well known [48], Kleppner was able to analytically calculate the density of states (see figure 2.2). The high frequency, long wavelength limit approaches free space conditions but large departures from this limit appear near waveguide cut-off frequencies where the density of states for photons is very high.

With this geometry in mind, prototypical Rydberg atom experiments were conceived as in figure 2.3. Generally some atomic Rydberg state is created in an atomic beam by use of appropriate laser excitation. Next the beam is directed into a cavity consisting of two metallic plates or mirrors which constrain the density of states for photons in that region. After some transit time the states of atoms in the beam are analysed usually by a combination of laser induced transitions and ionization. A signal is produced in the detection region by tuning the laser or ionizing electric field such that

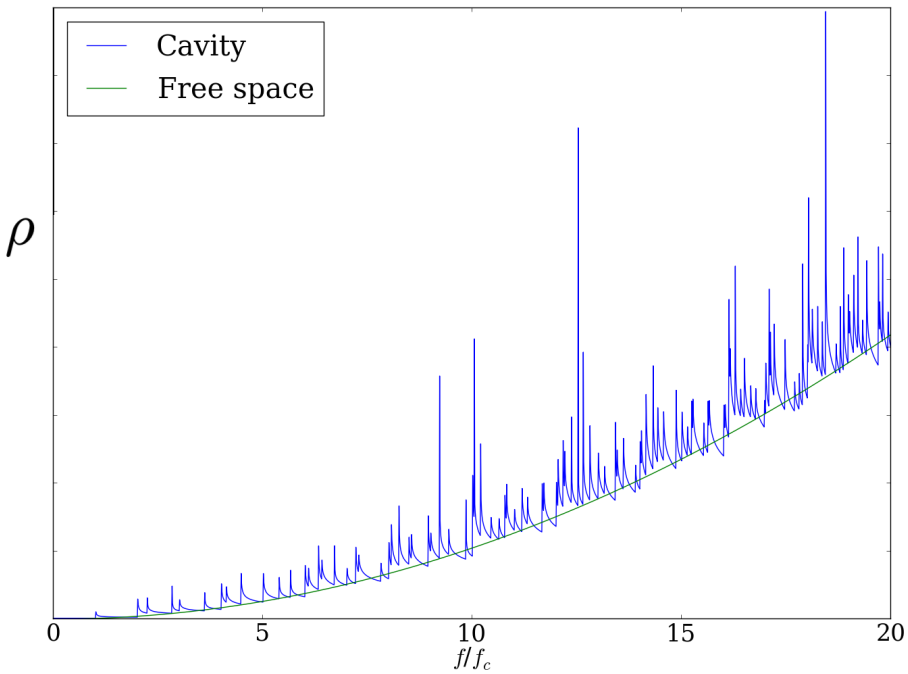

Figure 2.2: A reproduction of Kleppner's 1981 calculation for the photonic density of states in a rectangular waveguide. The result is compared with the free space case

atoms are ionized according to their state. By comparing the transit time for atoms to cross the cavity to the spontaneous emission rate in free space, inhibition or enhancement can be observed.

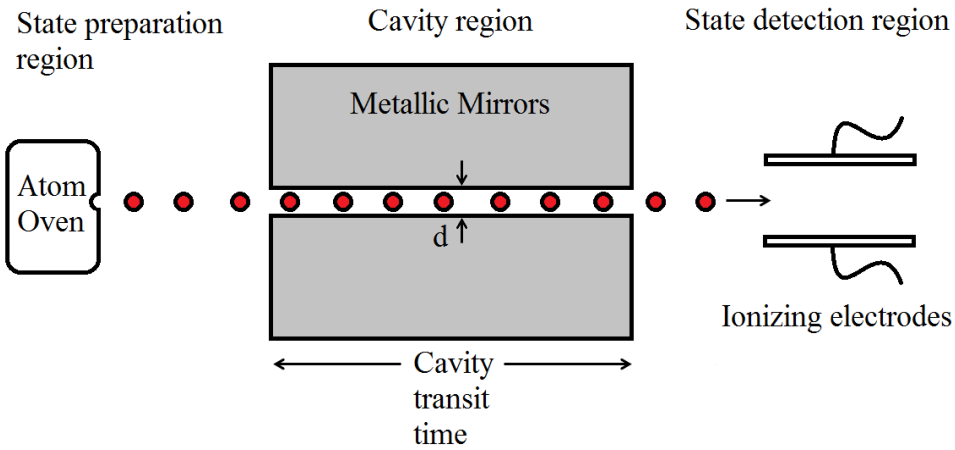

Figure 2.3: A typical experiment exhibiting spontaneous emission control of Rydberg atoms.

In [33] inhibited spontaneous emission was inferred when Caesium atoms in state $|n, |m| >= |22, 21>$ were observed to transit a cavity without decaying. The cavity transit time being about equal to the free space decay time meant that more $|22, 21>$ atoms arrived on the other side of the cavity than should have. The transition resonance was tuned using the Stark effect: by applying an electric field to the Rydberg atom, the resonant transition frequency could be shifted above and below the cut-off of the cavity.

A similar experiment was performed in [35] using Caesium atoms in the $5D_{5/2}$ state. Although multiple atomic decay channels from that state exist, spontaneous emission inhibition was observed when some of those channels are blocked. Decay channels with $\Delta m = \pm 1$ emit photons polarized differently than those with $\Delta m = 0$, and coupling to these decay channels could be tuned by varying a background magnetic field such that this field direction was either parallel or perpendicular to the cavity plates.

The first observation of enhanced spontaneous emission [26] followed the archetypal set-up of figure 2.3 except that the cavity transit time was shorter than the free space decay time. Sodium atoms prepared in the 23S state were observed in the detection region to have decayed to states $22P_{1/2}$ and $22P_{3/2}$, much faster than predicted by free space spontaneous emission. An addi-

tional difference between this and previous work includes the low temperature nature of the apparatus. Superconducting niobium plates in contact with a liquid helium bath were used to form the cavity. The superconducting plates set a cavity $Q \simeq 10^6$. Additionally, the atomic production region was separated from cavity and state detection region by thermal shields and microwave absorbers. This cold environment had the advantage that background (blackbody) radiation induced emission from the Rydberg atoms was negligible. The radiation temperature was set by the temperature of the cavity plates (about 7 K). Tuning the cavity on or off the transition resonance was achieved by moving one plate with a fine tuning screw (with the greatest enhancement observed on resonance).

Later, transitions at optical frequencies in ytterbium atoms were observed in a Fabry-Perot cavity [30]. For some time these resonators were thought to be impractical since the enhancement factor (λ^3/V from equation 2.2) is small at optical frequencies. To counteract this effect the experiment uses a large number of degenerate (transverse mode) resonances. They observe control of spontaneous emission by measuring florescence emitted from atoms in the resonator.

In a similar set up, this group was able to observe energy level shifts in Barium atoms resulting from cavity interactions [29]. Energy levels are mapped by weakly coupling a laser into the Fabry-Perot resonator, and scanning both the cavity length and laser frequency. When the cavity comes into resonance with the atomic transition, many excited atoms suddenly decay and a lower intensity of florescence is measured.

2.2.2 Solid state systems

Soon after the initial results in atomic and plasma physics Yablonovitch [61] noted that it might be beneficial to control spontaneous emission in electron-hole pairs in semiconductors. These electron-hole pairs form dipoles with energy levels and radiation patterns not dissimilar to atomic systems. The practical devices (lasers, transistors, solar cells etc) based on these materials often exhibit performance limited by spontaneous emission.

Enhancing spontaneous emission rates can provide lasers with larger bandwidth (when tunability is desired), lower lasing thresholds, and increased quantum efficiency [62]. Inhibited spontaneous emission rates can be used to sharpen spectral features and enhance operation speeds of light emitting diodes (LEDs). In the strong coupling regime where Cavity QED effects produce entanglement of emitters and photons, quantum cryptography applications result [57].

Yablonovitch proposed that a Fabry-Perot type resonator with distributive Bragg reflectors (DBR) in place of mirrors surrounding a semi-conductor filed cavity (see figure 2.4) would provide the sought after control.[5]

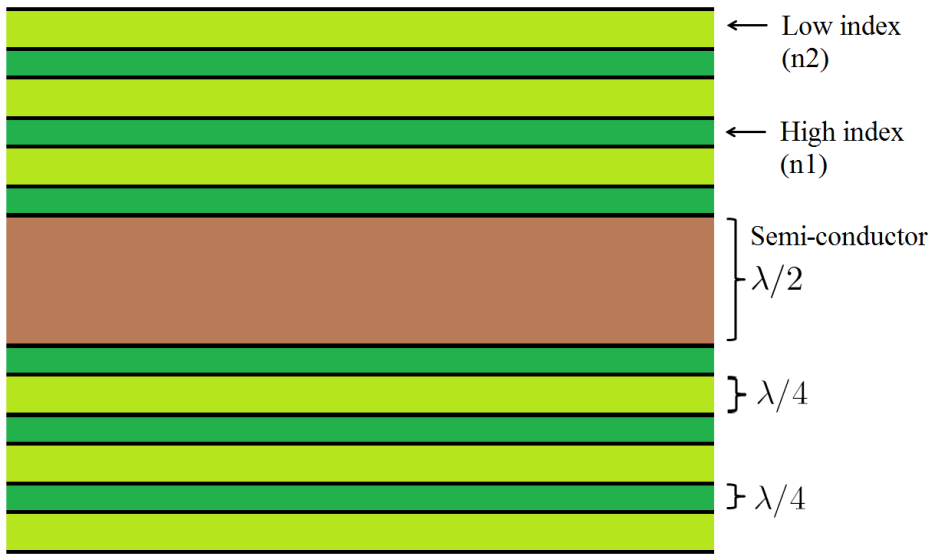

Figure 2.4: A distributive Bragg reflector is constructed of alternating layers of high and low dielectric materials. Each layer has a thickness $\lambda/4$ which enforces an interference pattern demanding reflection. If two such structures were placed on either side of a semi conducting slab, a Fabry Perot cavity is formed which constrains spontaneous emission.

Demonstration of spontaneous emission control came soon afterwards [60] with a different experiment than proposed above. These authors placed thin semi-conducting films on a variety of different substrates in an effort to change the local electric field which induces spontaneous emission. As motivation, the authors note that the electric field creation operator (E^+) within Fermi's Golden rule (expressed as $\Gamma = 2\pi\rho(E)\frac{|<xE^+>|^2}{\hbar}$, with x the dipole operator) is also modified by the environment.[6]

[5] Yablonovitch thought of the DBR as having a "photonic band gap" - a range of frequencies for which electromagnetic wave propagation was forbidden. This thought foreshadows the field of photonic crystals where 3-dimensional periodic structures exhibit photonic band gaps with widespread applications, among them control of spontaneous emission [44].

[6] We also hope to capitalize on this type of enhancement. See section 2.4 for a discussion

As an example, if a semi-conducting sphere is surrounded by some external material with a different index of refraction η (rather than an index matched material), then the field needed to be rescaled according to standard results from electrostatics:

$$E^{+}_{int} = \frac{3}{\eta^3_{int}/\eta^3_{ext} + 2} E^{+}_{ext} \tag{2.3}$$

By varying the substrate which supports the semi-conductor sample, radiative recombination was inhibited by a factor of about 5.

2.2.3 Plasmas

In 1985 Gabrielse observed the microwave cavity formed by a set of Penning trap electrodes to inhibit spontaneous emission [25].Those electrodes took the form of a metallic box with hyperbolic walls [7] as in figure 2.5. The experiment was conducted in a magnetic field of 6 T which sets the cyclotron wavelength to be about 2 mm. Due to the hyperbolic shape of the electrodes, the exact microwave mode structure was not known. It was, however, inferred that cavity effects must play a role since the distance between the electron and metal wall ($\simeq$ 6.7 mm) was comparable to the cyclotron wavelength.

This work was carried out in the context of precision measurements of the electron g-factor. Measurements of g required precision measurements of the cyclotron frequency (ω_c). As with Rydberg atoms, the cavity significantly perturbed the energy levels of the system (which, in this case, set the cyclotron frequency). Cavity effects had to be accounted for [9, 46] and much experimental and theoretical work was devoted to this end.

To make theoretical predictions about this effect, the authors included electric forces resulting from microwave resonances in the Penning trap in the equations of motion for their trapped electron [9, 8] (equation 2.4). Other terms in equation 2.4 result from the usual trapping forces; namely, the applied magnetic and electrostatic field.

$$\dot{\vec{v}} - \vec{\omega_c} \times \vec{v} + (e/m)\nabla V(\vec{r}) + \frac{1}{2}\gamma_c \vec{v} = (e/m)\vec{E}(\vec{r}) \tag{2.4}$$

By changing to a circular cylindrical Penning trap geometry the microwave resonances of the system became analytically tractable. Solving for $\vec{E}(\vec{r})$ with the method of images the authors were able to predict shifts in ω_c and

of our fill factor.

[7] This choice of electrode geometry was selected to obtain a quadrupole electrostatic potential.

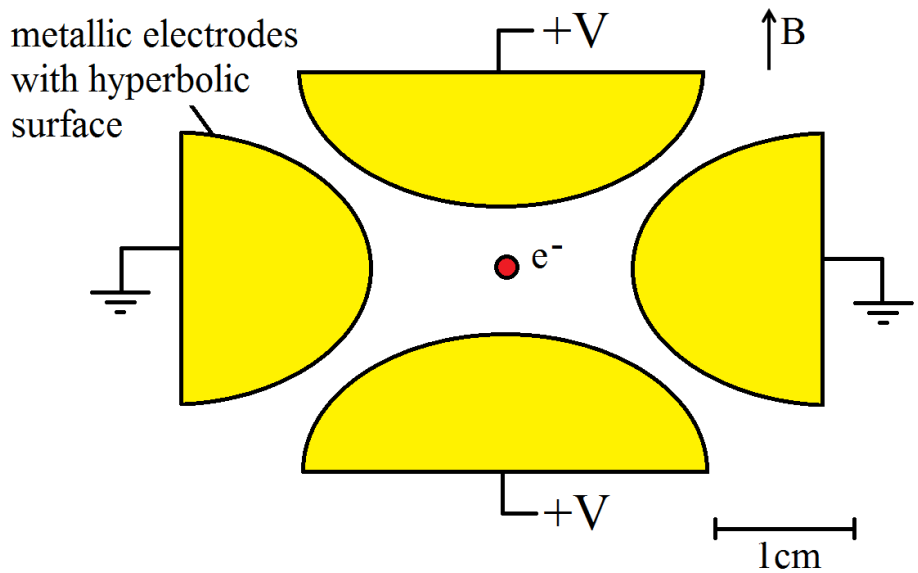

Figure 2.5: Hyperbolic electrodes were used to create a harmonic axial potential. The electrodes are circularly symmetric about the vertical axis.

γ_c resulting from interaction with microwave resonances of the trap. In particular those resonances with strong transverse electric fields at the location of the electron were shown to strongly perturb the cyclotron frequency and enhance the spontaneous emission rate.

Methods for detecting cavity modes in-situ were developed [53, 50, 51, 27]. These methods made use of equivalent circuit analyses [12, 59], and the perturbative coupling of the axial plasma oscillation to the cyclotron and spin degrees of freedom via magnetic nickel strips. Voltage measurements across electrodes at the axial plasma frequency, ω_z (typically in the MHz regime), allow inference of the cyclotron spontaneous decay rate and a mapping of the cavity resonance frequencies.

2.3 A null result at ALPHA

The first attempt to realize the Purcell Effect as a cooling technique at ALPHA occurred in 2011.

By matching the cyclotron frequency of positron plasmas to a microwave resonance of the ALPHA Penning trap (measured in [21]) we hoped to observe plasma temperatures drop to a new equilibrium temperature set by the Penning trap wall. The drop should occur at a much enhanced (relative to free space) rate set by the Purcell Effect.

By slowly incrementing the axial magnetic field we were able to scan the cyclotron frequency over a region thought to contain microwave resonances. We simultaneously monitor the temperature via a non-destructive technique [14] sketched in figure 2.6.

The technique excites and measures the quadrupole mode of electrostatic oscillation in the plasma. Detection is achieved through voltages induced by the plasma oscillation on a nearby electrode.

The quadrupole mode frequency, f_2, depends on the plasma temperature (T) according to

$$(f_2')^2 - (f_2)^2 = 5\left(3 - \frac{\alpha^2}{2}\frac{f_p^2}{(f_2^c)^2}\frac{\partial^2 g(\alpha)}{\partial\alpha^2}\right)\frac{k_B\Delta T}{m\pi^2 L^2} \tag{2.5}$$

where $\alpha = L/2r$ is the plasma aspect ratio, f_2^c is the quadrupole frequency in the cold fluid limit, k_B is the Boltzmann constant, and $g(\alpha) = 2Q_1\left(\alpha/\sqrt{\alpha^2-1}\right)/(\alpha^2-1)$ with Q_1 the first order Legendre function of the second kind. The plasma frequency is $f_p = \frac{1}{2\pi}\sqrt{ne^2/m\epsilon_o}$, where n is the plasma number density.

In the limit $\frac{f_2'-f_2}{f_2} \ll 1$, changes in the plasma quadrupole oscillation frequency are proportional to changes in the plasma temperature.

$$\Delta f_2 \simeq \beta \Delta T \tag{2.6}$$

By measuring changes in this oscillation frequency, the relative plasma temperature can be monitored.

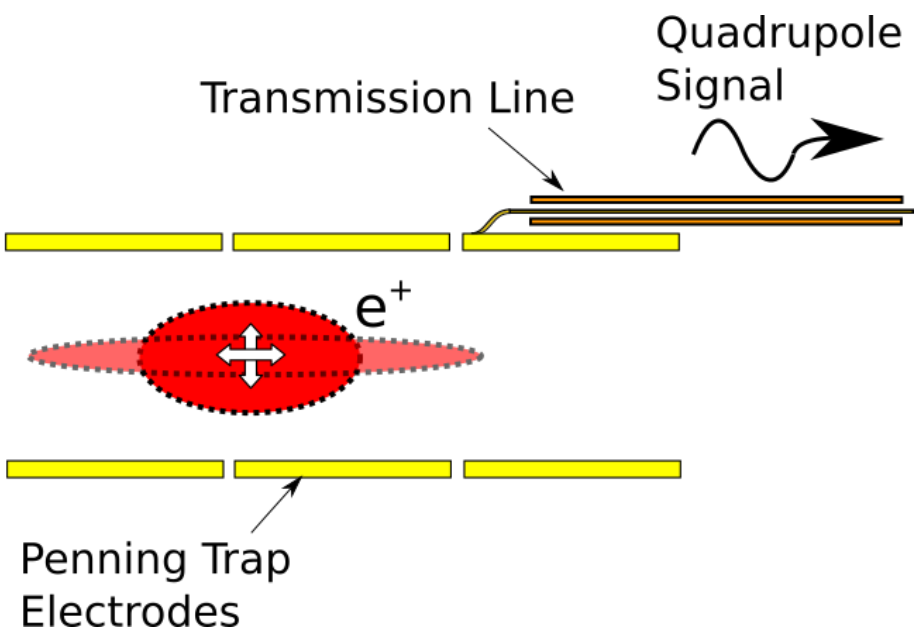

Figure 2.6: The plasma quadrupole mode inside a Penning trap is sketched . A transmission line attached to a nearby electrode detects this oscillation signal via image charges induced in the electrode.

Figure 2.7 shows the plasma temperature and quadrupole frequency versus the cyclotron frequency. The plot reveals complicated structure not consistent with the resonant frequencies of the trap. Additionally the temperature shows no great drop at any frequency. Multiple cross checks were made on this measurement involving alternate temperature measurement methods, magnetic field calibrations, reduction of positron number within the plasma, and simple repetition, none of which revealed an obvious result. A more detailed description of that test can be found in [24].

Two candidates for potential disruption of the cavity cooling effect at ALPHA have been identified. Firstly, these experiments were conducted with $N \simeq 10^5$ - 10^6 positrons, a number much greater than other experiments

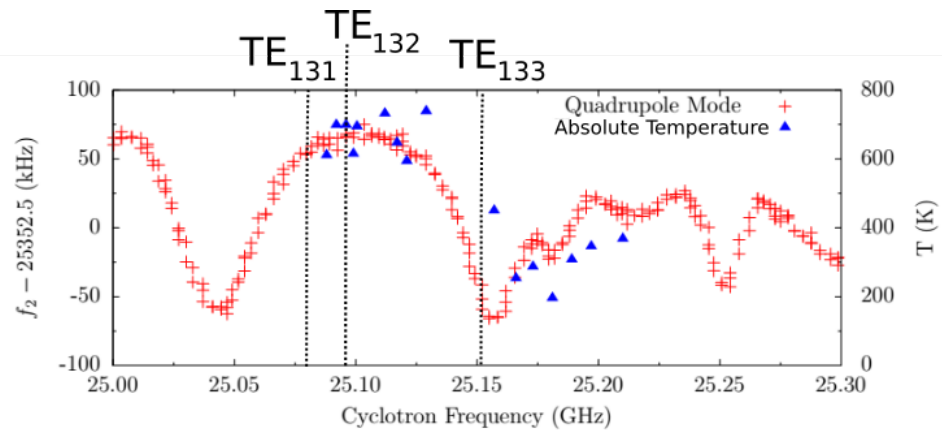

Figure 2.7: The quadrupole mode is monitored while scanning the cyclotron frequency across the measured frequencies of three cavity modes. No obvious mode structure revealed itself in the positron temperature measurements. Figure adapted from [24].

mentioned above. If the cooling effect is distributed over too many electrons then it could feasibly become ineffective and negligible. This many body effect is discussed in Chapter 4 and, using different techniques , in [47] . Our chosen solution is outlined in section 3.4.

Secondly, the properties of microwave resonances in the replica ALPHA stack may vary significantly depending on the environment. This seems likely since microwaves were found to leak through the gaps between electrodes allowing environmental factors to influence cavity resonances. For example, a number of striplines run axially down the outside of the ALPHA stack at CERN which were not present for the measurements in [21]. These striplines could act as antennas, carrying energy away and reducing both the Q and the positron-cavity coupling (the fill factor, χ, of section 2.4). To mitigate possible microwave leakage at gaps between electrodes and desensitize the cavity to its surrounding environment, choke structures have been incorporated into the cavity presented in chapter 3.

2.4 Circuit formulation of the Purcell Effect for a cyclotron oscillator

This section presents our own formulation of the Purcell effect for the case of a single charged particle in a strong magnetic field. For comparison's sake, we first derive the free space decay rate. Both models are purely classical.

2.4.1 Cooling in free space

The cyclotron cooling rate of a particle in a field B, due to radiation into free space is given by

$$1/\tau_c = \frac{P}{E_{KE}} \tag{2.7}$$

where P is the power radiated by a charged particle in a circular orbit and E_{KE} is the kinetic energy of the particle. Combining the Larmor formula for the radiation of an accelerated particle

$$P = \frac{e^2 a^2}{6\pi\epsilon_o c^3} \tag{2.8}$$

with $E_{KE} = \frac{1}{2}m\omega^2 r^2$, one obtains the well known formula

$$1/\tau_c = \frac{e^2\omega^2}{3\pi\epsilon_o c^3 m} = \frac{e^4 B^2}{3\pi\epsilon_o c^3 m^3}. \tag{2.9}$$

For a plasma sufficiently dense that the (two) cyclotron degrees of freedom easily equilibrate with the (third) axial degree of freedom, this cooling rate has to be multiplied by a factor 2/3 to give:

$$1/\tau_{net} = \frac{2e^4 B^2}{9\pi\epsilon_o c^3 m^3}. \tag{2.10}$$

For electrons and positrons in a 1 Tesla field this gives $\tau_c = 3.87$ sec, to be compared to measured values of about 4 sec in the ALPHA apparatus.

Note that this result is derived for a single charged particle. It is applicable to a dilute plasma under the assumption that the individual phases of the cyclotron orbits of the particles are randomly distributed. Also, the formula is only valid in the classical limit, where $\hbar\omega$ is much less than the average excitation energy of the cyclotron levels. For electrons and positrons in a 1 Tesla field, $\hbar\omega \simeq 1.5$ Kelvin, so that we expect the results to apply to the ALPHA lepton plasmas.

2.4.2 Cyclotron cooling of a particle inside a resonant cavity

A cavity with conducting walls can strongly perturb the spectrum of the final states into which a particle can decay. We use a very simple model of a charged particle in a B-field parallel to the plates of a capacitor (figure 2.8, and then generalize the result to an arbitrarily shaped cavity.

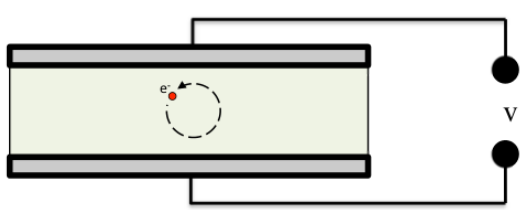

Figure 2.8: An electron in circular orbit in a capacitor

The oscillating component of the charge on the capacitor is $2er\cos(\omega t)/d$ so that the open circuit voltage across the capacitor is

$$v = \frac{q}{C} = \frac{2er\cos(\omega t)}{d \times (\epsilon_o A/d)} = \frac{er\cos(\omega t)}{\epsilon_o A} \tag{2.11}$$

where ω is the cyclotron frequency eB/m, and d is the gap between capacitive plates of area A.

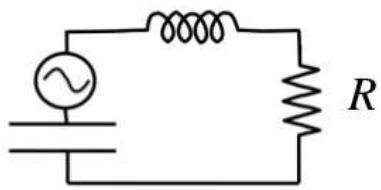

Figure 2.9: The capacitor of figure 2.8 in a resonant circuit.

If we now put the capacitor in a series resonant circuit (see figure 2.9) such that $\omega_o = 1/\sqrt{LC}$ coincides with the cyclotron frequency, then the average power delivered to the resistance R is

$$P = \frac{< v^2 >}{R} = \frac{4e^2r^2}{2\epsilon_o^2 A^2 R} \tag{2.12}$$

Therefore the damping rate of the cyclotron motion is

$$1/\tau_c = \frac{P}{E_{KE}} = \frac{4e^2}{\epsilon_o A^2 m\omega^2 R}. \tag{2.13}$$

Using $R = 1/(\omega CQ)$ we obtain

$$1/\tau_c = \frac{4e^2 Q}{\epsilon_o m\omega V_c}. \tag{2.14}$$

where $V_c = Ad$ is the volume of the capacitor.

Using $\omega = eB/m$ and including the factor of $2/3$ to account for the axial degree of freedom one obtains

$$1/\tau_{net} = \frac{8eQ}{3\epsilon_o B V_c}. \tag{2.15}$$

For a cavity with non-uniform values of the electric field $\vec{E}$, this generalizes to

$$1/\tau_{net} = \frac{8eQ}{3\epsilon_o B V_c} \frac{E_o^2}{< E^2 >} \tag{2.16}$$

or more formally

$$1/\tau_{net} = \frac{8eQ}{3\epsilon_o B} \frac{E_o^2}{\int E^2 \, \mathrm{d}V} \tag{2.17}$$

Here, for a particular cavity mode, E_o is the value of the electric field normal to the cyclotron orbit when the cavity is excited and, at the same excitation level, $< E^2 >$ is the mean square electric field in the cavity. For a simple capacitor with $d \ll \sqrt{A}$, $\vec{E}$ is uniform and $\chi = 1/V$. For the bulge resonator proposed in section 3 (with $V = 26\mathrm{cm}^3$) the fill factor is seen to vary by factors of 10 depending on mode type. Simulation and measurements of χ yield

$$\chi = \frac{E_o^2}{\int E^2 \, \mathrm{d}V} \simeq 10^6 \frac{1}{\mathrm{m}^3}. \tag{2.18}$$

for the TE_{1lm} modes.

As an example, a cavity with the above fill factor, a resonant frequency at 28 GHz with $Q = 4000$ predicts a cooling time of

$$1/\tau_{net} \simeq 5\mathrm{ms} \tag{2.19}$$

representing an improvement over the free space case by a factor of about 1000.

2.4.3 Decay rate for an oscillator inside a cavity with non-uniform fields

Consider the case of a physically small LC circuit inside the capacitor of a physically large LRC circuit as in figure 2.10. The mutual capacitance will be used to calculate the voltage induced on the latter resonator by the former. The cooling rate will be derived in this context in order to motivate the fill factor, χ.

The decay rate is now

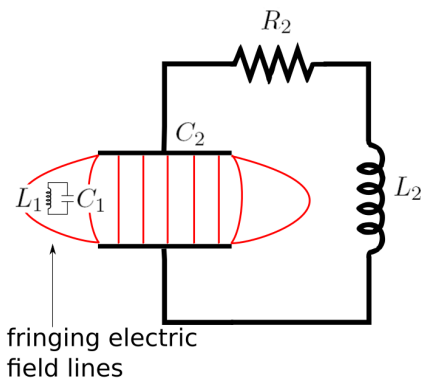

Figure 2.10: A small loss-less LC resonator is placed near the capacitive edge of a large, lossy LRC resonator.

$$1/\tau = \frac{P}{U_1} \tag{2.20}$$

where $P =< V_2^2 > /R_2$ is the power dissipated in the large resonator and $U_1 = \frac{q_1^2}{2C_1}$ is the energy stored in the small resonator.

The voltages across these capacitors (for respective charges q_1 and q_2) are

$$\begin{aligned} V_1 =& \frac{q_1}{C_1} + \frac{q_2}{C_{21}} \\ V_2 =& \frac{q_2}{C_2} + \frac{q_1}{C_{12}} \end{aligned}$$

Neglecting the self-capacitive terms we have

$$P = \frac{q_1^2}{2C_{12}^2 R_2} \tag{2.21}$$

so that the decay rate (with the definition for U_1) is

$$1/\tau = \frac{C_1}{C_{12}^2 R_2} \tag{2.22}$$

In order to find C_{12} we make use of the reciprocity of mutual capacitance

$$C_{12} = C_{21} \tag{2.23}$$

and write

$$\begin{aligned} V_1 \simeq& \frac{q_2}{C_{21}} \\ V_1 =& E_1 d_1 \\ V_1 =& E_2(r) d_1 \end{aligned}$$

to obtain

$$C_{12} = C_{21} = \frac{q_2}{E_2(r) d_1} \tag{2.24}$$

together with $C_1 = \epsilon_o A_1/d_1$ the decay rate is

$$1/\tau = \frac{\epsilon_o A_1 d_1^2 E_2^2(r)}{d_1 q_2^2 R_2} \tag{2.25}$$

The energy in the second capacitor $U_2 = \frac{q_2^2}{2C_2} = \frac{\epsilon_o}{2}\int E^2\,\mathrm{d}V$ allows us to remove q_2 from equation 2.25.

$$1/\tau = \frac{V_1}{C_2 R_2}\frac{E_2^2(r)}{\int E^2\,\mathrm{d}V} \tag{2.26}$$

Finally we use $Q_2\omega_o = 1/R_2C_2$ to arrive at

$$1/\tau = V_1\omega_o Q_2\chi \tag{2.27}$$

This can be seen to match the result of the last section if one allows some phenomenological or effective volume

$$V_1 = \frac{4e^2}{\epsilon_o m\omega_o^2} \tag{2.28}$$

2.4.4 Comparison with the quantum result

Beginning with Fermi's Golden Rule (equation 2.1) we attempt to derive the cavity enhanced cooling rate.

$$\Gamma = 2\pi\rho(E)\frac{|<f|H|i>|^2}{\hbar} \tag{2.29}$$

The perturbing Hamiltonian results from a dipole interaction:

$$H = exE(x) \tag{2.30}$$

with e the electron charge, x the charge's position and $E(x)$ the electric field at that location. Expressing the position operator as a sum of raising and lowering operators ($x = \sqrt{\hbar/2m\omega_o}[a_+ + a_-]$), allows us to compute the emission and absorption rates:

$$\begin{aligned}\Gamma_{emission} =& \frac{\pi\rho e^2 E^2(x)}{m\omega_o}(l+1)\\ \Gamma_{absorption} =& \frac{\pi\rho e^2 E^2(x)}{m\omega_o}l\end{aligned}$$

where l is the quantum number for the harmonic oscillator excitation and we have used $a_-|l>=\sqrt{l}|l-1>$ and $a_+|l>=\sqrt{l+1}|l+1>$.

The cooling rate is

$$\begin{aligned}\Gamma =&\Gamma_{emission} - \Gamma_{absorption}\\ =&\frac{\pi\rho e^2 E^2(x)}{2m\omega_o}\\ =&\frac{\pi e^2 E^2(x)}{2m\omega_o\hbar\Delta\omega}\\ =&\frac{\pi Q e^2 E^2(x)}{2m\omega_o^2\hbar}\end{aligned}$$

where we have used the density of states appropriate for a cavity resonance.

$$\begin{aligned}\rho =&\frac{1}{\hbar\Delta\omega}\\ =&\frac{Q}{\hbar\omega_o}\end{aligned}$$

Following [7] we normalize the electric field according to the number of photons in the cavity. We perform the rescaling $E^2 \to E^2/n$ with

$$n\hbar\omega_o = \frac{\epsilon_o}{2}\int E^2\,\mathrm{d}V. \tag{2.31}$$

The cooling rate becomes

$$\begin{aligned}\Gamma =&\frac{\pi Q e^2 E^2(x)}{\hbar m\omega_o^2}\frac{2\hbar\omega_o}{\epsilon_o\int E^2\,\mathrm{d}V}\\ =&\frac{2\pi Q e^2}{\epsilon_o m\omega_o}\chi\end{aligned}$$

which matches the classical expression up to a factor of $\pi/2$.

Chapter 3

The Bulge Cavity

This chapter of the thesis describes a microwave cavity which has been shown to cool electrons at a collaborative plasma experiment at Berkeley. A description of the Berkeley apparatus can be found in [47].

The Penning trap at Berkeley is designed in the style of that used at ALPHA and often used as a testing ground for new plasma techniques. Absent from the experiment at Berkeley are many of the strict design requirements necessary for a full antihydrogen experiment. This relaxation allows us to design a so called bulge resonator compatible with the open tubular geometry of this style of Penning trap. The resonator is shown in figure 3.5.

3.1 Resonances of a cylindrical cavity

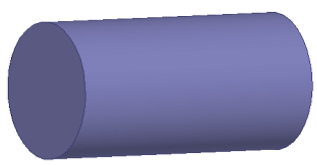

Figure 3.1: The right circular cylinder represents the inner space of a metallic container.

The resonator described in this section strongly resembles a simple cylindrical cavity (figure 3.1). Therefore, throughout our study we make use of the nomenclature surrounding this geometry. Additionally, we often revert to thinking about the right circular cylinder when testing simple ideas or developing intuition about the behaviour of the more complicated cavity resonances to be presented in later sections. Accordingly, a short section is now devoted to electromagnetic resonances inside a conducting cylinder.

Beginning from the Helmholtz equation ($\nabla^2\vec{E} + k^2\vec{E} = 0$) for electric and magnetic fields, one may split the Laplacian operator into parts as

$$\nabla^2 \to \nabla_T^2 + \frac{\partial^2}{\partial z^2} \tag{3.1}$$

where ∇_T^2 represents the transverse Laplacian in the cylindrical coordinates r and ϕ. Assuming that these electromagnetic waves propagate axially, the z dependence satisfies

$$\frac{\partial^2\vec{E}(r,\phi,z)}{\partial z^2} = -\beta^2\vec{E}(r,\phi,z) \tag{3.2}$$

and the Helmholtz equation becomes

$$\nabla_T^2\vec{E} = k_c^2\vec{E} \tag{3.3}$$

where the cut-off wavevector has been defined $k_c^2 = k^2 - \beta^2$.

By using Maxwell's equations ($\nabla \times \vec{E} = -i\omega\vec{H}$ and $\nabla \times \vec{H} = i\omega\epsilon\vec{E}$) together with tedious algebra, one may show that all field components can be expressed in terms of the axial fields only.

$$\begin{aligned}
E_r &= -\frac{i}{k_c^2}\left(\beta\frac{\partial E_z}{\partial r} + \frac{\omega\mu}{r}\frac{\partial H_z}{\partial \phi}\right) \\
E_\phi &= \frac{i}{k_c^2}\left(-\frac{\beta}{r}\frac{\partial E_z}{\partial \phi} + \omega\mu\frac{\partial H_z}{\partial r}\right) \\
H_r &= \frac{i}{k_c^2}\left(\frac{\omega\epsilon}{r}\frac{\partial E_z}{\partial \phi} + \beta\frac{\partial H_z}{\partial r}\right) \\
H_\phi &= -\frac{i}{k_c^2}\left(\omega\epsilon\frac{\partial E_z}{\partial r} + \frac{\beta}{r}\frac{\partial H_z}{\partial \phi}\right)
\end{aligned} \tag{3.4}$$

Therefore, a solution to

$$\nabla_T^2 E_z = k_c^2 E_z \tag{3.5}$$

together with the correct boundary conditions for the cylinder will yield complete field solutions to cavity resonances.

These solutions generally fall into two categories: transverse electric (TE) waves and transverse magnetic (TM) waves. The former have $E_z = 0$ and the latter have $H_z = 0$. Separation of variables shows that, for the TE waves,

$$H_z = (AJ_n(k_c r) + BN_n(k_c r))\,(C\cos(n\phi) + D\sin(n\phi)) \tag{3.6}$$

where J_n and N_n are the nth order Bessel functions of the first and second kind respectively. Applying boundary conditions allows us to reduce this expression considerably. $B = 0$ since fields must be finite at the origin ($r = 0$) and $D = 0$ by a judicious choice of the origin for ϕ.

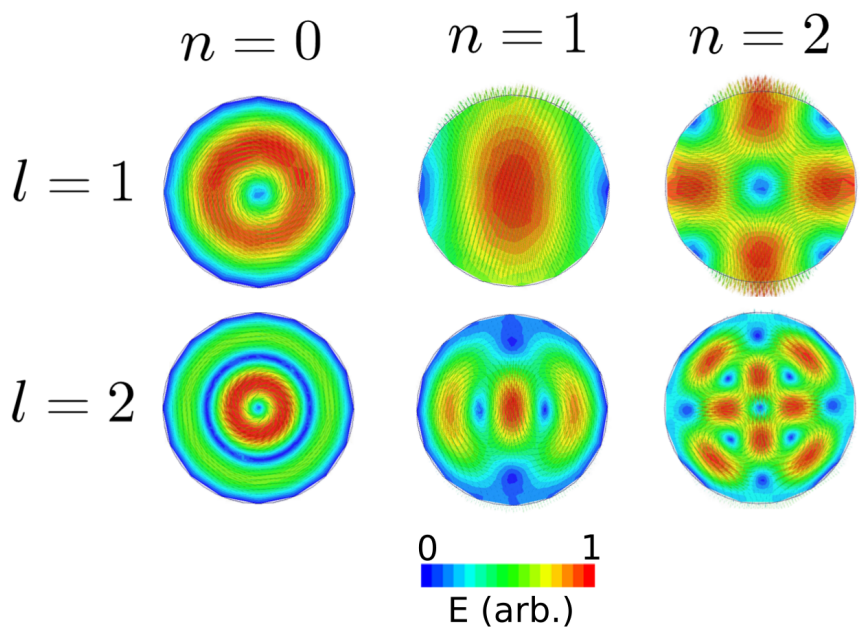

Figure 3.2: Electric fields for transverse electric resonances of a cylindrical cavity: TE_{01} , TE_{11} ,TE_{21}, TE_{02}, TE_{12}, TE_{22}. The above field contours are taken for $\sin(\beta z) = 1$.

The conducting boundary conditions on the radius of the cylinder ($E_\phi = 0$ at $r = a$) gives

$$k_c = \frac{p'_{nl}}{a}$$

where p'_{nl} is the zero of of the relevant Bessel function derivative ($J'(p'_{nl}) = 0$). Imposing the axial boundary conditions on equations 3.4

$$
\begin{aligned}
H_z &= AJ_n(k_c r)\cos(n\phi)\left(A_L \exp(-i\beta z) + A_R \exp(+i\beta z)\right) \\
E_r \propto E_\phi &\propto i\left(A_L \exp(-i\beta z) + A_R \exp(+i\beta z)\right) \\
H_r \propto H_\phi &\propto i\left(-\beta A_L \exp(-i\beta z) + \beta A_R \exp(+i\beta z)\right),
\end{aligned}
$$

gives $A_R = -1/2$ and $A_L = 1/2$. As a result $E_r \propto E_\phi \propto \sin(\beta z)$ with an "axial wavevector" $\beta = \frac{m\pi}{L}$.

Finally, the solutions take the form

$$
\begin{aligned}
H_z &= AJ_n(k_c r)\cos(n\phi)\sin(m\pi z/L) \\
H_\phi &= \frac{n\beta}{k_c^2 r} AJ_n(k_c r)\sin(n\phi)\cos(m\pi z/L) \\
H_r &= \frac{\beta}{k_c} AJ_n'(k_c r)\cos(n\phi)\cos(m\pi z/L)
\end{aligned}
$$

$$
\begin{aligned}
E_r &= -i\frac{\omega\mu n}{k_c^2 r} AJ_n(k_c r)\sin(n\phi)\sin(m\pi z/L) \\
E_\phi &= -i\frac{\omega\mu}{k_c} AJ_n'(k_c r)\cos(n\phi)\sin(m\pi z/L)
\end{aligned}
$$

where the factor of i in the electric field expressions represents a $\pi/2$ phase shift (in time) relative to the magnetic fields. The fields of a specific cavity resonance are completely determined by the three wavenumbers: n, l, and m. It is common, therefore, to denote cavity resonances with the notation TE_{nlm}. These field patterns are shown in figure 3.2 for a handful of resonances.

The frequency of such a resonance can be written

$$
f_{lnm} = c\sqrt{\left(\frac{p'_{nl}}{2\pi a}\right)^2 + \left(\frac{m}{2L}\right)^2}
$$

The corresponding solutions for TM modes (shown in figure 3.3) are

$$H_\phi = -i\frac{\omega\epsilon}{k_c}AJ_n'(k_c r)\cos(n\phi)\cos(m\pi z/L)$$
$$H_r = -i\frac{n\omega\epsilon}{k_c^2 r}AJ_n(k_c r)\sin(n\phi)\cos(m\pi z/L)$$

$$E_z = AJ_n(k_c r)\cos(n\phi)\cos(m\pi z/L)$$
$$E_r = \frac{\beta}{k_c}AJ_n'(k_c r)\cos(n\phi)\sin(m\pi z/L)$$
$$E_\phi = \frac{\beta n}{k_c^2 r}AJ_n(k_c r)\sin(n\phi)\sin(m\pi z/L)$$

with

$$f_{nlm} = c\sqrt{\left(\frac{p_{nl}}{2\pi a}\right)^2 + \left(\frac{m}{2L}\right)^2}$$

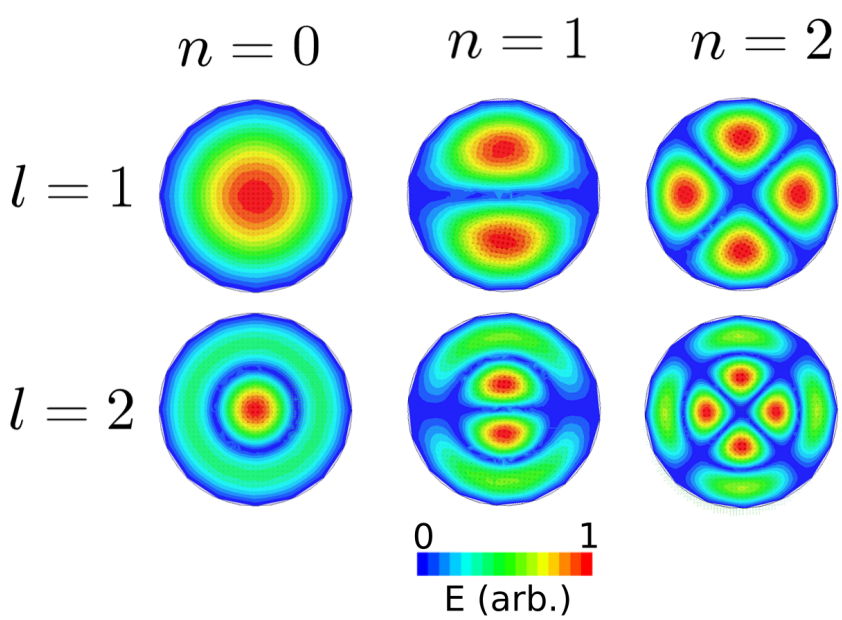

Figure 3.3: Electric fields of TM_{nlm} resonances of a cylindrical cavity. : TM_{01} , TM_{11} ,TM_{21}, TM_{02}, TM_{12}, TM_{22}. The fields point axially out of the page. The above field contours are taken for $\sin(\beta z) = 1$.

The axial variation for a few of these modes is shown in figure 3.4.

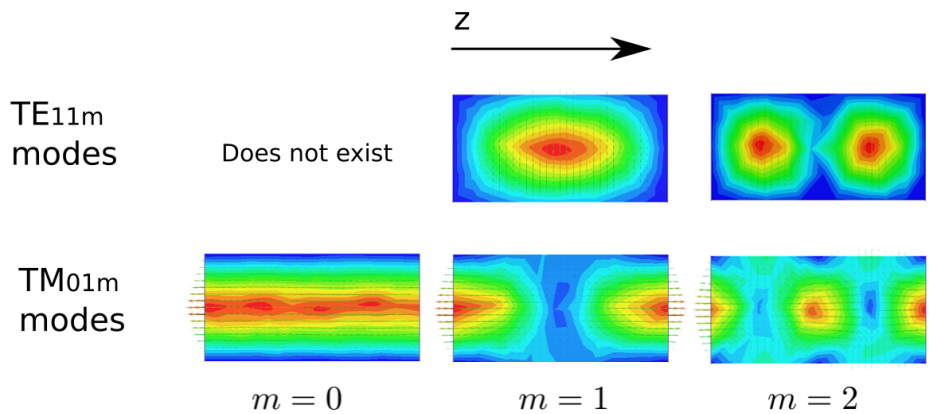

Figure 3.4: Axial dependence of TE and TM modes.

3.2 Bulge design

Our bulge resonator maintains the cylindrical symmetry of the right circular cylinder (above), but removes the traditional axial boundary conditions. Instead we create some localized region where a microwave mode can propagate, surrounded by regions where propagation is forbidden. To achieve this, the inner radius swells across three electrodes from small end regions to a larger central region. In the central region a mode can propagate, while in the end regions this same mode is beyond cut off and must decay exponentially. Both the outer surfaces of the electrodes and the segmented nature of the cavity were designed to be compatible with the existing Penning trap at Berkeley.

The inner bulge surface is parametrized as

$$r = -1.25\text{mm}\cos(t) + 11.25\text{mm}$$
$$z = \frac{L}{2\pi}t + b$$

where $L = 75.6$ mm, b is a constant that places the maximum radius in the middle of the central electrode and $t \in (0, 2\pi)$. Detailed drawings are included in appendix A.

This geometry was chosen to produce a high Q resonance near the electron cyclotron frequency at 1 Tesla (28 GHz). A high Q dictates a high emission rate according to the Purcell effect. In order to couple to the cyclotron motion the resonance must also have strong transverse electric fields

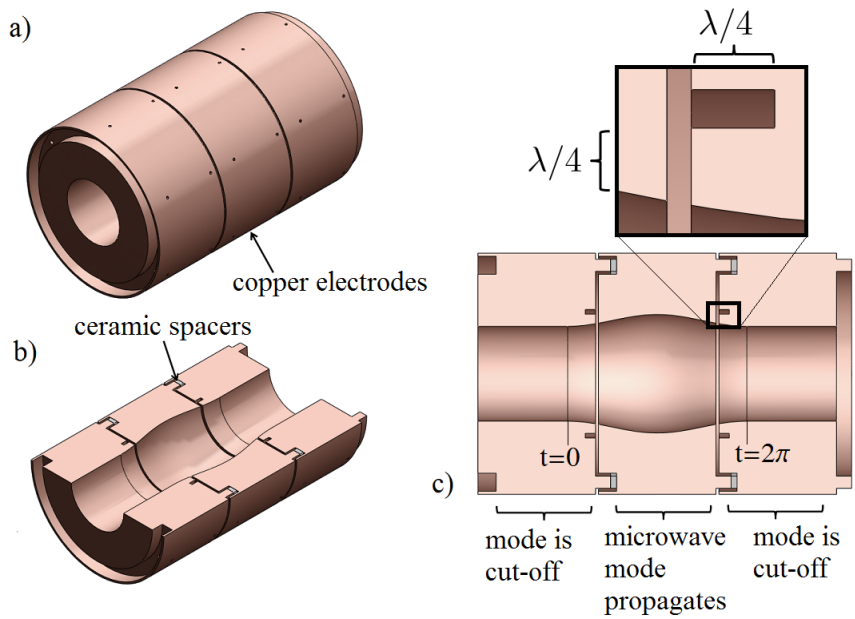

Figure 3.5: Profiles of the bulge resonator are shown. a) shows an isometric outer view of three electrodes; b) the same view in cross-section with electrically isolating ceramics labelled; c) shows another cross-section labelled according to regions which trap microwaves versus regions in which propagation of these modes is forbidden. The inset of (c) shows the choke structure which prevents microwave leakage through the gaps between electrodes.

at the location of the plasma. For on-axis plasmas this limits useful resonances to the set of TE_{1lm} and TM_{1lm} modes. Additionally, higher order (higher l) TE modes are generally preferred since they produce the most favourable fill factors (χ, equation 2.17). We also note that an appropriately smooth evolution of the inner radius is required. Sharp steps in the radius may case so-called mode conversion, leakage of microwave energy from the cavity, and consequent lowering of the resonance Q.

3.3 Simulations of resonant fields and frequencies

Although we use the right circular cylinder to guide our intuition about microwave resonances in this structure, the exact boundary conditions for this geometry are significantly more complicated and make analytical solutions for the resonant electric and magnetic fields impossible. In order to determine resonant frequencies of this cavity, a commercial microwave simulation program (HFSS) is employed. Using finite element analysis multiple "trapped modes" of the bulge are identified. As expected, resonances resemble those of the right circular cylinder. Figure 3.6 shows field patterns of the TE_{131} mode identified via simulation. The axial dependence of the magnitude of the electric field is shown in figure 3.7 where one sees that the mode is well localized within the bulge region.

Gaps between electrodes (as well as the choke structure of section 3.6) are not shown but were included and found to have little effect on the resonances. Opened axial faces of end electrodes are approximated to have free space boundary conditions ($Z = 377\,\Omega$). The radial face is modelled as a general conductor having the resistivity of our alloy (see section 3.4 and appendix B). A summary of the simulation results for cavity modes observed to cool electrons is in table 3.1.

3.4 Lowering the cavity Q

An attempt to lower the Q may seem contrary to our desire for strong cooling via a high spontaneous emission rate according to equation 2.17. However, this cooling rate prediction was made for a *single* particle interacting with the cavity. To be useful for anti-hydrogen production, *many* positrons must be cooled. Indeed a typical experiment either at Berkeley or ALPHA involves millions or hundreds of millions of leptons.

In light of the many-particle reality, it seems possible that the cavity would be receiving energy from leptons faster than it can dissipate this en-

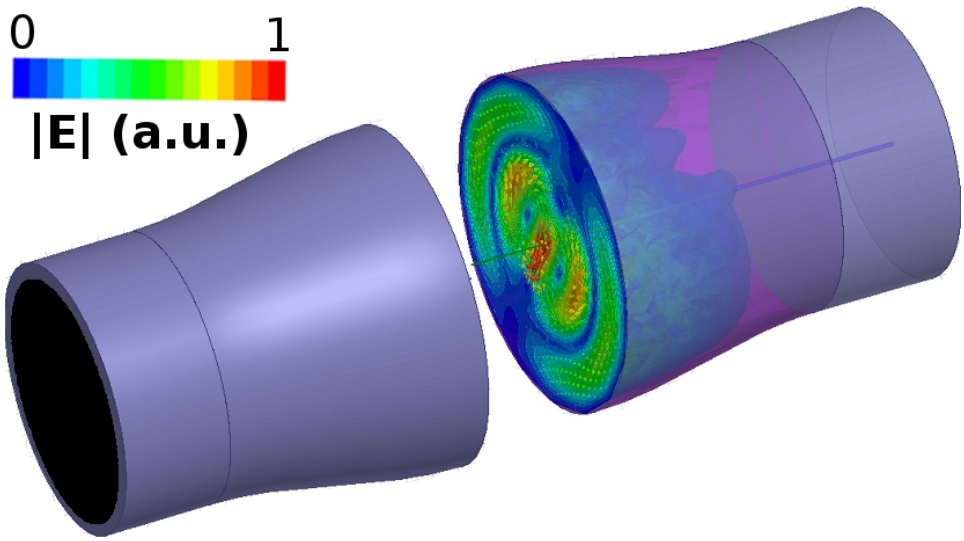

Figure 3.6: Simulated resonant electric fields resembling a TE_{131} mode are shown. The frequency and Q of this mode were near 33 GHz and 4000 respectively.

Cavity Mode	f_o (GHz)	Q	χ (10^6) m^{-3}	τ (ms) (equation 2.17)
TE_{121}	21.8	1580	1.66	6.2
TE_{123}	25.3	1090	0.99	17.4
TE_{131}	34.3	2660	3.20	2.9
TE_{132}	36.5	2200	2.46	5.2
TE_{133}	38.4	1440	2.10	9.2
TE_{134}	40.1	1300	1.63	14.0

Table 3.1: A summary of the simulated cavity resonances. Only the TE_{131} was characterized experimentally. Its measured frequency and Q were $f_o =$ 33.80 GHz and $Q \simeq 2500$. $\chi = E_o^2 / \int E^2 \, \mathrm{d}V$ is the fill factor (equation 2.18).

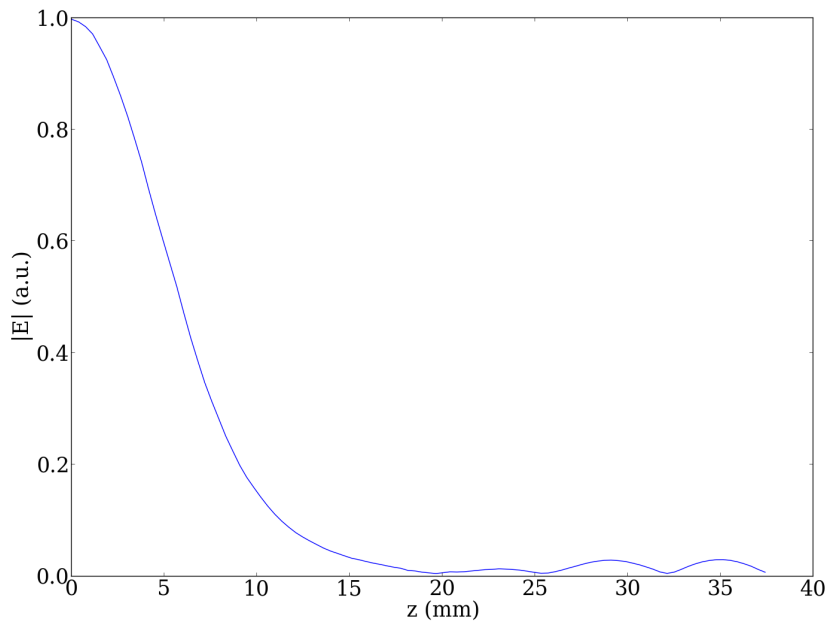

Figure 3.7: $|E(r = 0)|^2$, the simulated on-axis electric field magnitude is shown as a function of the axial coordinate z.

ergy. A deeper analysis of this effect can be found in chapter 4 and by Povilus in [47], both of which make predictions for the maximum number of leptons a cavity can cool. Both of these analyses conclude that, in order to cool a large number of electrons, the cavity Q needs to be appropriately lowered so as to remove energy from the lepton-cavity coupled system faster.

Energy loss from our cavity is set by two primary mechanisms: leakage out the axial end faces, and resistive losses in the metallic cavity walls.

Ideally, radiation should not be able to couple into or out of our cavity. Such coupling would allow room temperature blackbody radiation from removed parts of the experiment to affect the equilibrium temperature of the plasmas. One expects a copper cavity of our size, with no leakage, to have a $Q \simeq 10^4$. That the measured (and simulated) Q of this cavity is only $\simeq 10^3$ indicates that microwave leakage is significant. Unfortunately, reducing loss by this mechanism would require a redesign of the cavity geometry.

The second energy loss mechanism, resistive losses in the cavity, can be affected by coating the inner face of the copper cavity with a resistive alloy[8]. Isaac Martens of the Bizzotto Electro-chemistry group at UBC intervened here to electroplate the inner face of the resonator with a Nichrome-like alloy. Nichrome (nickel-chromium) is a metallic alloy with a temperature independent conductivity a factor of about 100 lower than room temperature copper.

If resistive losses dominated the resonator Q, we would expect a reduction in Q by a factor

$$\sqrt{\frac{\sigma_{\text{Nichrome}}}{\sigma_{\text{copper}}}} \simeq 10 \tag{3.7}$$

However, since microwave leakage is not negligible, we see some intermediate reduction and achieve $Q \simeq 2200$ in both simulation and experiment. (This represents reduction by a factor of $\simeq 2$ from the case of a bare copper cavity wall: $Q = 4500$).

We note that it was not obvious beforehand that this method for lowering the Q would work. Discussion is in appendix B

[8] Attempts to lower the cavity Q by use of a coupling loop (see, for example, figure 3.11) terminated by a cold load, were attempted but not used. Simulations showed that this kind of local perturbation caused severe reduction of the fill factor due to generation of unwanted waveguide modes.

3.4.1 Anti-static coatings

Nichrome, like copper, will oxidize. The oxide will be poorly conducting and may hold a static charge which could compromise the cylindrical symmetry of the trap. This has the potential to induce diocotron instabilities [58] which threaten our control of the plasma. Therefore, as is common with any Penning trap apparatus, the surfaces exposed to the plasmas must be coated in some non-oxidizing material. Usually gold is electroplated onto the trap electrodes.

Gold

Coating the inner surface of our microwave cavity with gold would also raise the cavity Q thus counteracting the effect of the nichrome. We investigated whether or not a thin layer of gold could be used as an anti-static coating without shielding cavity modes from resistive losses which are desired in the underlying nichrome layer. Calculations and experimental confirmation are left to an appendix, but our conclusion is that a thin gold layer (thinner than the skin depth) would be acceptable. At 30 GHz the skin depth of gold is $\simeq$ 450 nm and results (see figure B.4) show that a gold layer of 100 nm would not change the surface resistance unbearably.

Graphite

Another solution for anti-static coatings exists: colloidal graphite. Graphite is preferable since it does not require difficult electroplating processes. Also, the shielding effect which occurs with a gold anti-static layer is negligible. Manufacturer specifications [52] indicate a graphite (Acheson Aerodag G) resistivity of

$$\rho_g \simeq 3 \times 10^{-2}\,\Omega \cdot \mathrm{m} \tag{3.8}$$

which implies a skin depth at 30 GHz of $\simeq 0.5$ mm. As a test of the graphite's low temperature resistivity, we applied about 1 μm of graphite to a glass tube and measured the sheet resistance in a liquid helium bath. The results are shown in table 3.2.

	300 K	4 K
R_s kΩ/square	24	89

Table 3.2: Measured sheet resistance of Aerodag G at room-temperature and at 4 K.

An increase in the resistivity of a factor of about 3.5 is seen at low temperatures. This is consistent with literature results [36]. Since the anti-static layer is much thinner than the skin depth, its effect on the microwave losses in the cavity will be negligible.

For this cavity we choose the graphite anti-static coating. The final inner surface of the bulge cavity is shown in figure 3.8 with nichrome and graphite layered on top of copper.

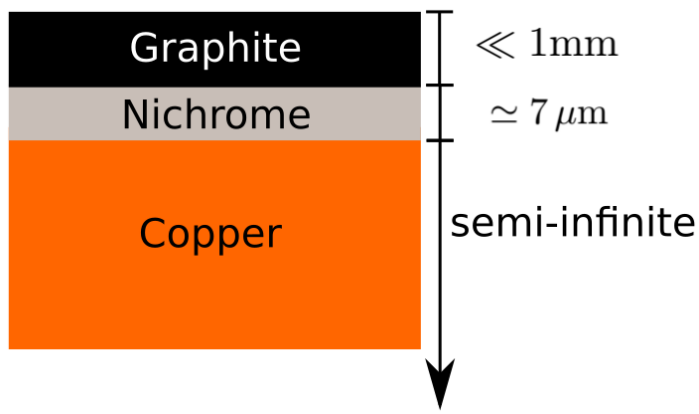

Figure 3.8: The layered inner surface of the bulge cavity is shown. A nichrome like alloy was electroplated to the bulk copper in an effort to lower the cavity Q. Colloidal graphite was added on the outermost layer as an electrostatic shield.

3.4.2 Magnetism

The nichrome-like alloy displays considerably higher magnetic susceptibility than standard 80/20 nichrome. This is not too surprising in light of an elemental analysis conducted by Isaac Martens which revealed that the alloy is principally nickel (and $< 1\%$ chromium). Once plated to the inner cavity wall we magnetize the alloy with an ion pump magnet ($B \simeq 1200$ Gauss). After the magnet is removed we used a Hall probe to measure the on-axis magnetic field resulting from the alloy (see set-up in figure 3.9)

Figure 3.10 shows the magnetic field fit to the model discussed in chapter 6.

Equation 6.9 provides an estimate for the alloy thickness:

$$t \simeq 7\,\mu\text{m} \tag{3.9}$$

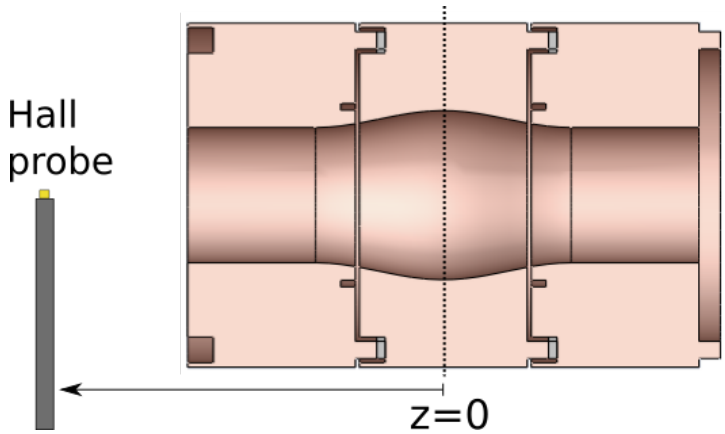

Figure 3.9: The set up for measurements of the magnetic field resulting from a nichrome-like alloy plated to the inner surface of the cavity.

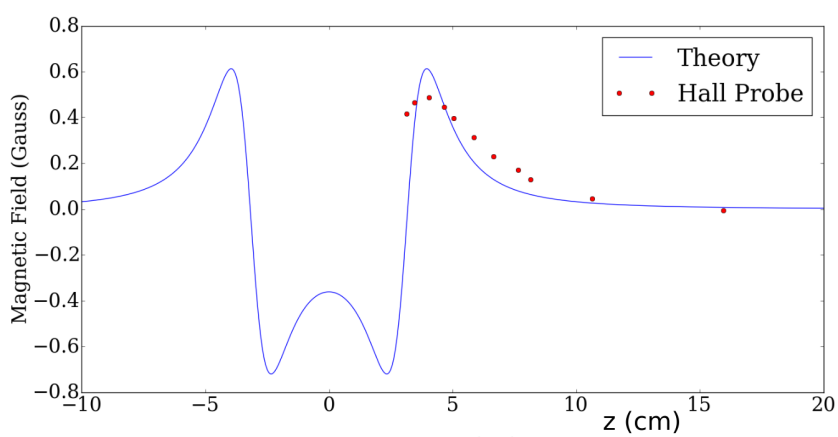

Figure 3.10: Hall probe measurements of the on-axis magnetic field are plotted with a fit to the model of chapter 6.

3.5 Cavity fill factor χ

We measure the cavity fill factor by inserting a small dielectric bead inside the cavity (see figure 3.11) and employing cavity perturbation analysis.

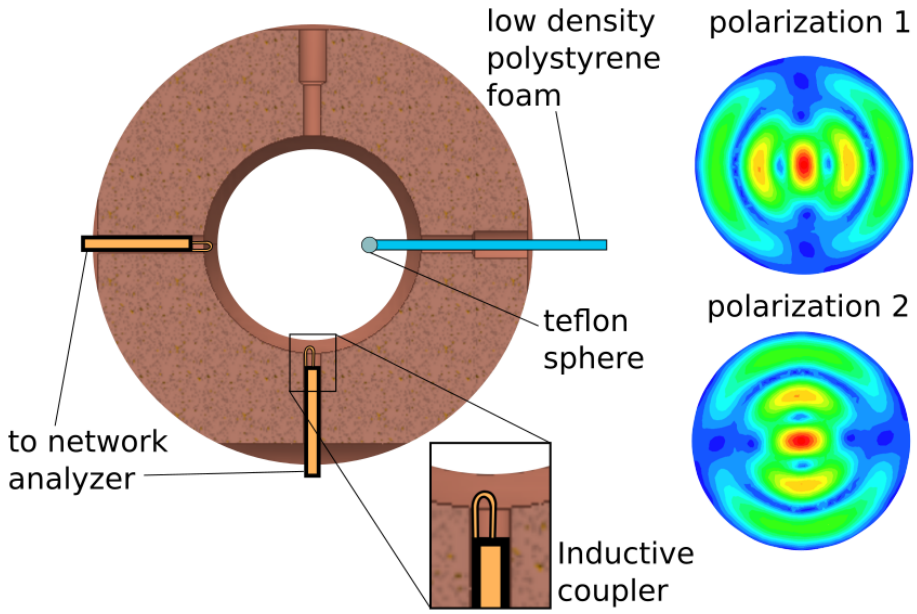

Figure 3.11: A small teflon bead is inserted into the cavity. The changes in frequency of two resonances are monitored via inductive coupling to a network analyzer. The frequency shifts allow us to map the electric field of these modes.

Following Waldron [55] we have

$$\frac{\partial\omega}{\omega_o} = \frac{-3(\epsilon-1)V_1}{2(\epsilon+2)}\frac{E_o^2}{\int E^2\,\mathrm{d}V} \tag{3.10}$$

where $\partial\omega$ is the shift in resonance frequency due to the presence of a small dielectric sphere, ω_o is the unperturbed resonance frequency, V_1 is the dielectric volume, and ϵ is the relative permittivity of the perturbing teflon.

This, combined with the definition for the fill factor $\frac{E_o^2}{\int E^2\,\mathrm{d}V}$ (section 2.4) gives

$$\chi = -\frac{\partial\omega}{\omega_o}\frac{2(\epsilon+2)}{3(\epsilon-1)V_1} \tag{3.11}$$

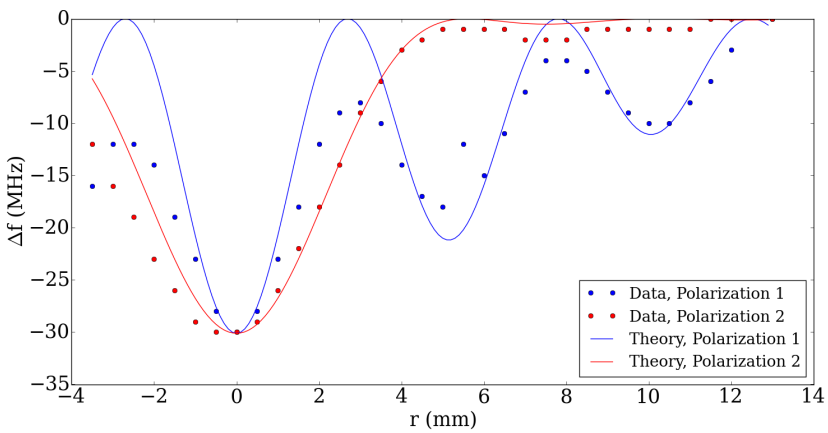

Figure 3.12: The frequency shift of two orthogonal cavity resonances as a function of the radial position of a small perturbing teflon bead.

Using the frequency shift at $r = 0$ we obtain

$$\chi = 3.2 \times 10^6\,\mathrm{m}^{-3} \tag{3.12}$$

in good agreement with the simulated result from table 3.1.

3.6 Chokes

Chokes are $\lambda/4$ structures conventionally used in microwave waveguides to prevent radiation leakage at joints where two guides have been connected. At such a joint electrical contact is typically poor and this structure serves to "fake" good contact. We employ the structure to prevent microwaves from leaking radially at the gaps between electrodes: see the inset in figure 3.5 (c)

Transmission line theory provides some intuition for the working mechanism of a choke. The input impedance (Z_{in}) of a lossless transmission line of characteristic impedance Z_0, terminated with a load impedance Z_L as in figure 3.13, is

$$Z_{in} = Z_0 \frac{Z_L + iZ_0 \tan(2\pi l/\lambda)}{Z_0 + iZ_L \tan(2\pi l/\lambda)} \tag{3.13}$$

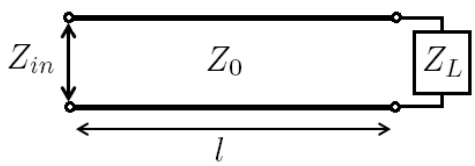

Figure 3.13: A transmission line schematic with input impedance Z_{in}, characteristic impedance Z_0, and load impedance Z_L labelled. If the length (l) is tuned correctly, Z_L can be transformed to desired values at Z_{in}.

In the limit $l = \lambda/4$, we have $Z_{in} \to Z_0^2/Z_L$. If the load is a short circuit ($Z_L = 0$) the input impedance is infinite. On the other hand if the load is an open circuit ($Z_L \to \infty$) then the input impedance is zero. We therefore see that $\lambda/4$ is a special length for a transmission line. A short circuit at this distance is transformed into a open circuit . Similarly, an open circuit is transformed into a short. Transforms of this type (see figure 3.14) simulate electrical contact between electrodes for a range of microwave frequencies (centred on c/λ).

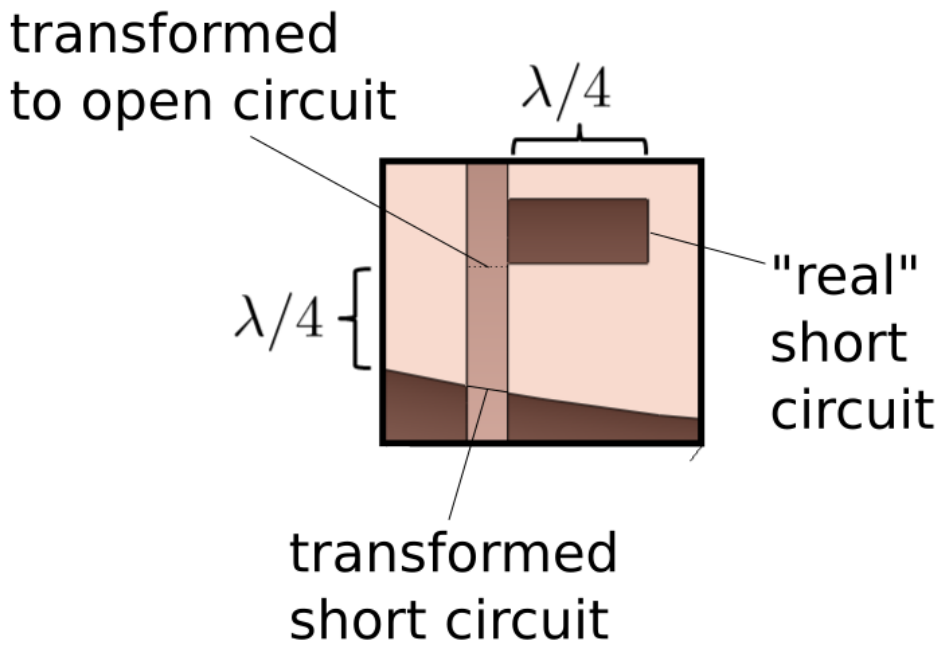

Figure 3.14: The metal bottom of the $\lambda/4$ groove acts as a short which is transformed twice to the edge of the cavity where it serves to simulate electrical contact.

Chapter 4

Simulations of N Coupled Resonators: Cavity and Electrons

The purpose of this chapter is to investigate the cooling of many electrons by a single cavity. In the case of a single electron the description of section 2.4 is valid. To be useful as a cooling technique at ALPHA, the method must be able to cool large numbers of positrons simultaneously. However, there exists a certain number of particles above which the cooling effectiveness of the cavity begins to diminish. This occurs when the rate of energy entering the cavity (due to the combined cyclotron radiation from all leptons) starts to perturb the equilibrium thermal excitation of the relevant cavity mode.

Here we develop a classical circuit model to describe the many body cooling process. This simplified model neglects much of plasma physics: in particular the z motion, as well as the magnetron motion of the particles. In spite of this, we predict that our cavity can effectively cool 10^4 - 10^5 electrons.

4.1 The circuit model

We model N electrons in cyclotron motion coupled to a dissipative microwave cavity resonance as N RLC circuits inductively coupled to one lossy RLC resonator as in figure 4.1. The requirement of low loss in our electron resonators relative to the cavity can be expressed as $R_i/R_0 \ll 1$ or $Q_i/Q_0 \gg 1$ where Q is the circuit quality factor.

For electrons directly coupled to the cavity (but not to each other) we can write the circuit equations as

$$0 = \frac{q_0}{C_0} + \dot{q_0}R_0 + \ddot{q_0}L_0 + \sum_{i=1}^{N} M_i\ddot{q_i} \tag{4.1}$$

and

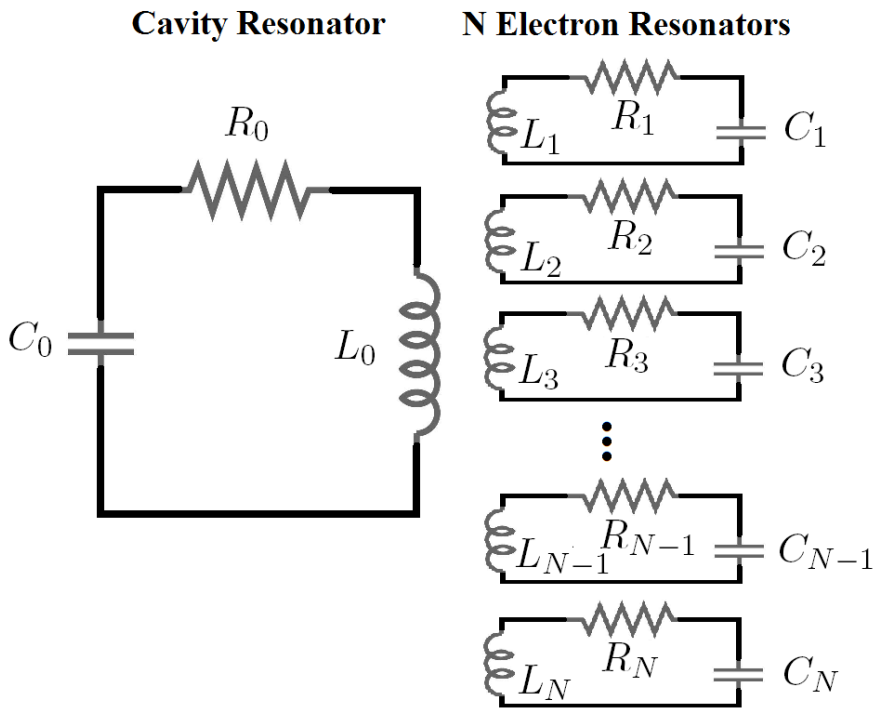

Figure 4.1: N RLC circuits (model electrons) with low R_i, inductively coupled to one lossy (high R_0) RLC circuit (a microwave cavity resonator).

$$0 = \frac{q_i}{C_i} + \dot{q}_i R_i + \ddot{q}_i L_i + M_i \ddot{q}_0 \tag{4.2}$$

where M_i is the mutual inductance between the ith “electron”-circuit and the "cavity" circuit, and q_i is the charge on its capacitor. q_0 represents the charge on the “cavity”-circuit capacitor.

Dividing through by the inductances and using

$$\begin{aligned} \omega &= \frac{1}{\sqrt{LC}} \\ Q &= \frac{\omega L}{R} \end{aligned} \tag{4.3}$$

we can rewrite equations 4.1 and 4.2 as

$$0 = \omega_0^2 q_0 + \frac{\omega_0}{Q_0}\dot{q}_0 + \ddot{q}_0 + \sum_{i=1}^{N} k_i \ddot{q}_i \tag{4.4}$$

$$0 = \omega_i^2 q_i + \frac{\omega_i}{Q_i}\dot{q}_i + \ddot{q}_i + k_i \ddot{q}_0 \tag{4.5}$$

with a coupling parameter $k_i = M_i/L_i$.

Substituting 4.5 into 4.4 to eliminate $\ddot{q}_i$

$$\begin{aligned} 0 &= \omega_0^2 q_0 + \frac{\omega_0}{Q_0}\dot{q}_0 + \ddot{q}_0 - \sum_{i=1}^{N} k_i \left(\omega_i^2 q_i + \frac{\omega_i}{Q_i}\dot{q}_i + k_i \ddot{q}_0\right) \\ &= \omega_0^2 q_0 + \frac{\omega_0}{Q_0}\dot{q}_0 + (1 - N k_i^2)\ddot{q}_0 - \sum_{i=1}^{N} k_i \left(\omega_i^2 q_i + \frac{\omega_i}{Q_i}\dot{q}_i\right) \end{aligned} \tag{4.6}$$

gives us a solution for $\ddot{q}_0$. Setting all coupling constants equal to each other, $k_i = k$, we have

$$\ddot{q}_0 = \frac{-\omega_0^2 q_0 - \frac{\omega_0}{Q_0}\dot{q}_0 + \sum_{i=1}^{N} k \left(\omega_i^2 q_i + \frac{\omega_i}{Q_i}\dot{q}_i\right)}{1 - N k^2} \tag{4.7}$$

substituting this into 4.5 we get an analogous equation for $\ddot{q}_i$

$$\begin{aligned} \ddot{q}_i &= -\omega_i^2 q_i - \frac{\omega_i}{Q_i}\dot{q}_i - k\ddot{q}_0 \\ \ddot{q}_i &= -\omega_i^2 q_i - \frac{\omega_i}{Q_i}\dot{q}_i - k\left(\frac{-\omega_0^2 q_0 - \frac{\omega_0}{Q_0}\dot{q}_0 + \sum_{j=1}^{N} k \left(\omega_j^2 q_j + \frac{\omega_j}{Q_j}\dot{q}_j\right)}{1 - N k^2}\right) \\ \ddot{q}_i &= \frac{k\omega_0}{1 - N k^2} q_0 - \sum_{i \neq j} \frac{k^2 \omega_j^2}{1 - N k^2} q_j - \left(\frac{k^2 \omega_i^2}{1 - N k^2} + \omega_i^2\right) q_i + \frac{k\omega_0}{(1 - N k^2) Q_0}\dot{q}_0 \\ &\quad - \sum_{i \neq j} \frac{k^2 \omega_j}{(1 - N k^2) Q_j}\dot{q}_j - \left(\frac{k\omega_i}{(1 - N k^2) Q_i} + \frac{\omega_i}{Q_i}\right)\dot{q}_i \end{aligned} \tag{4.8}$$

We may now solve the system of coupled differential equations as an eigenvalue matrix problem.

Defining a vector

$$\vec{q} = \begin{pmatrix} q_0 \\ q_1 \\ q_2 \\ \vdots \\ q_{N-1} \\ q_N \\ \dot{q}_0 \\ \dot{q}_1 \\ \dot{q}_2 \\ \vdots \\ \dot{q}_{N-1} \\ \dot{q}_N \end{pmatrix} \tag{4.9}$$

and assuming that the time dependence of each charge follows $q_i = \mathrm{e}^{\alpha t}$, then there are $2(N+1)$ eigenvalues (α) which are the solution to

$$\dot{\vec{q}} = \alpha \vec{q} = A\vec{q} \tag{4.10}$$

A is a matrix whose components are found as coefficients in equations 4.7 4.8. The decay rates and frequencies are then $\mathrm{Re}(\alpha)$ and $\mathrm{Im}(\alpha)$ respectively.

Once the eigenvalues are known the general solution is

$$q_p(t) = \sum_{l=0}^{N} c_l v_{p,l} \mathrm{e}^{\alpha_l t} \tag{4.11}$$

where $v_{p,l}$ is the pth component of the lth eigenvector, α_l is the corresponding eigenvalue, and c_l is a constant set by the initial conditions.

4.1.1 Results

We define a cavity decay (α_c) rate as the average of the two fastest decay rates ($\mathrm{Re}(\alpha)$) and a electron decay rate (α_e) as the average of the remaining $\mathrm{Re}(\alpha)$. The decay times are

$$\tau_c = \frac{1}{\alpha_c}$$
$$\tau_e = \frac{1}{\alpha_e}$$

ω_0	$2\pi \times 30$GHz
Q_0	1000
Q_i	10^9

Table 4.1: Typical simulation parameters.

An example simulation result for these decay times as a function of the number of electrons coupled to the cavity is shown in figure 4.2. We chose resonant frequencies and quality factors (table 4.1) to resemble the physical case of electrons in a 1 Tesla magnetic field.

The resonant frequencies of the electrons were chosen from a normal distribution centred around ω_0 and with standard deviation $\sigma \approx \frac{\omega_0}{10Q_0}$. The coupling parameter k was chosen such that, for the single electron case ($N = 1$),

$$\tau_e \approx 100\tau_c. \tag{4.12}$$

This condition is satisfied for k between 10^{-4} and 10^{-5}. This choice was made since, to first order, we expect overloading when $\tau_e = \tau_c N$, and since $N = 100$ requires a comfortable amount of computational power for a reasonable desktop computer.

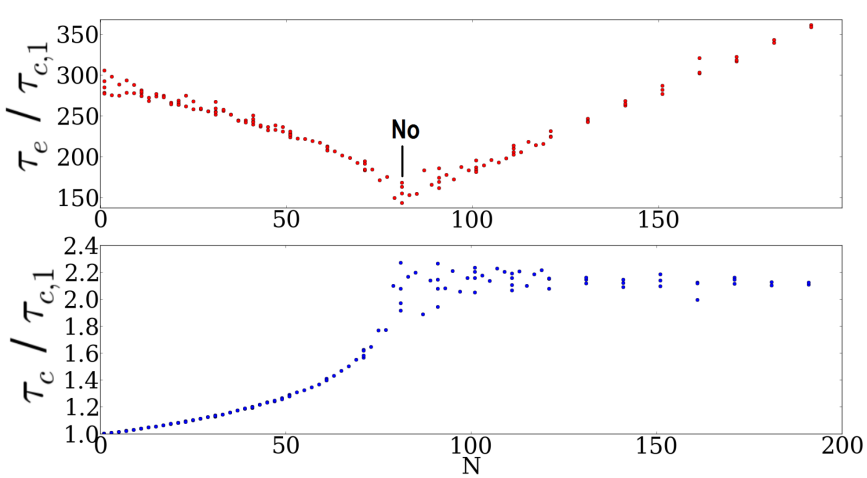

Figure 4.2: Decay times for N electrons coupled to a microwave resonance as a function of N. The result is normalized to the single particle decay time for the cavity.

The result in figure 4.2 shows overload to occur just below $N = 100$.

4.1.2 Overloading analysis

In terms of energy conservation, overloading will occur when the power dissipated in the cavity is less than that dissipated by the electrons

$$\begin{aligned} P_c &< NP_e \\ \frac{E}{\tau_c/2} &< N\frac{E}{\tau_e/2} \\ \tau_c &> \frac{\tau_e}{N} \end{aligned} \tag{4.13}$$

as in the last section. This gives an overload number N_o

$$N_o = \frac{\tau_e}{\tau_c} \tag{4.14}$$

However since τ_c and τ_e are both functions of N (as is obvious when looking at figure 4.2), the overload number must be determined self-consistently:

$$N_o = \frac{\tau_e(N_o)}{\tau_c(N_o)} \tag{4.15}$$

In addition to this complication, τ_e and τ_c may also depend on all the other parameters in the problem k, σ, ω_0, Q_0, and Q_i. It would therefore be easier if we knew N_o in terms of the single particle decay times which can be calculated from theory according to equation 2.17.

We may relate the single electron decay time to that at overload through empirical trends present in the simulations.

The electron decay time at overload is approximately half that as for the single electron case[9], while the cavity decay time at overload is about twice that as for the single electron case (This trend is shown for various couplings, k, in figure 4.3).

$$\begin{aligned} \tau_e(N_o) =& \frac{\tau_{e,1}}{2} \\ \tau_c(N_o) =& 2\tau_{c,1} \end{aligned}$$

We may write the single electron cavity decay time using $Q_c = \frac{\omega_0}{2\alpha_c}$

$$\tau_{c,1} = \frac{2Q_0}{\omega_0} \tag{4.16}$$

[9]We note that this result is dubious: Why should the cavity be not be able to cool a single particle as well as some intermediate number?

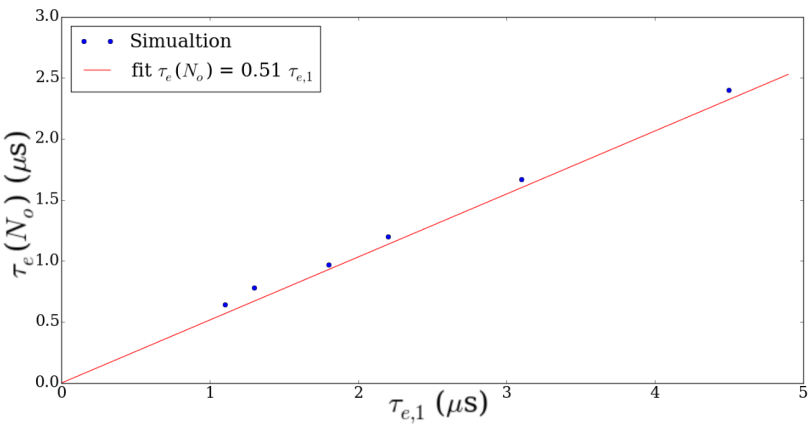

Figure 4.3: Decay times at overload versus single particle decay times

Therefore the overload number is

$$\begin{aligned} N_o &= \frac{\tau_{e,1}}{4\tau_{c,1}} \\ N_o &= \frac{\tau_{e,1}\omega_0}{8Q_0} \end{aligned} \tag{4.17}$$

This prediction is plotted versus the overload number read off from simulation results in figure 4.4.

Next we use the cavity cooling equation for a single electron (equation 2.17 with a factor of 2 inserted to account for the doubly degenerate resonance of this cavity)

$$\begin{aligned} \tau_{e,1} &= \frac{3\epsilon_o B}{16eQ_0\chi} \\ \tau_{e,1} &= \frac{3\epsilon_o m\omega_0}{16e^2Q_0\chi} \end{aligned} \tag{4.18}$$

for fill factor χ and magnetic field $B = m\omega_0/e$.

The overload number is

$$N_o = \frac{3\epsilon_o m\omega_0^2}{128e^2Q_0^2\chi} \tag{4.19}$$

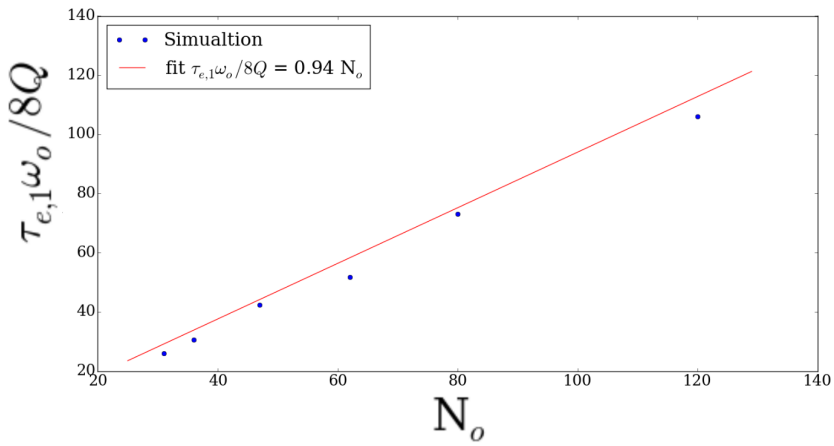

Figure 4.4: Predicted overload number versus overload result from simulation.

This overload number is plotted as a function of Q in figure 4.5

The overload number is calculated in table 4.2 for cavity resonances described in chapter 3.

Cavity Mode	$N_o(10^4)$
TE_{121}	3.4
TE_{123}	15.9
TE_{131}	1.4
TE_{132}	3.6
TE_{133}	9.4
TE_{134}	17.0

Table 4.2: Cavity resonance overload predictions.

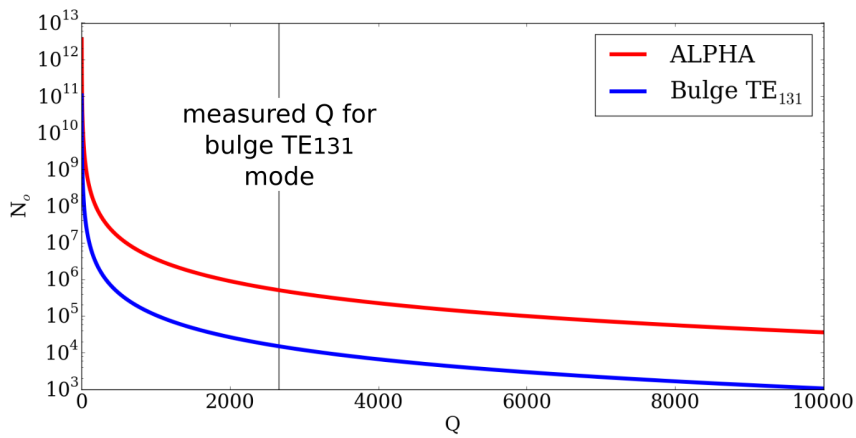

Figure 4.5: Overloading numbers for the ALPHA cavity and the Berkeley cavity as a function of cavity Q. For the Berkeley Cavity, $\omega_0 = 2\pi \times 34$GHz and $\chi = 3.2 \times 10^6\,\mathrm{m}^{-3}$ was used. For the ALPHA cavity the parameters are $\omega_0 = 2\pi \times 25$GHz and $\chi = 5.1 \times 10^4\,\mathrm{m}^{-3}$. The ALPHA Q was 6000, giving $N_o = 490{,}000$, while a Berkeley $Q = 2660$ gives $N_o = 14{,}000$.

4.2 Averaging theory and the rotating frame

4.2.1 General formulation

In non-linear dynamics, averaging theory is a well known and powerful tool for solving complex systems. The general system

$$\ddot{x} + x + \delta h(x, \dot{x}) = 0 \tag{4.20}$$

can be recast in a "rotating frame" with the transformations

$$\begin{aligned} x &= \rho(t)\cos(t + \phi(t)) \\ y &= \dot{x} = -\rho(t)\sin(t + \phi(t)) \end{aligned} \tag{4.21}$$

where the amplitude and phase (ρ and ϕ) are both functions of time. At first glance this seems incorrect. With the second transform defining y, did we not neglect time derivatives of ρ and ϕ? Actually Equation 4.21 is a definition and we will shortly return to impose the correct differential equation on our new variables.

We impose

$$\begin{aligned} \dot{y} &= -x - \delta h(x,y) \\ y &= \dot{x} \end{aligned} \tag{4.22}$$

Then,

$$\begin{aligned} \rho^2 &= x^2 + y^2 \\ \rho\dot{\rho} &= \dot{x}x + \dot{y}y \\ \rho\dot{\rho} &= yx - y(x + \delta h(x,y)) \\ \rho\dot{\rho} &= -\delta h(x,y)y \end{aligned} \tag{4.23}$$

Now substitute the rotating frame transform for y

$$\rho\dot{\rho} = \delta h(x,y)\rho\sin(t+\phi) \tag{4.24}$$

to obtain the equation of motion for ρ

$$\dot{\rho} = \delta h(x,y)\sin(t+\phi). \tag{4.25}$$

We are now in a position to employ averaging theory on this rotating frame variable ρ

4.2.2 Simple example: a single damped harmonic oscillator

First, a simple example is shown to illustrate the elegance of this technique. A damped harmonic oscillator obeys

$$\ddot{x} + x + \delta\dot{x} = 0 \tag{4.26}$$

for which $h(x,y) = y$

The equation of motion is now

$$\dot{\rho} = -\delta\rho\sin^2(t+\phi) \tag{4.27}$$

and by averaging over one cycle ($<\sin^2(t+\phi)>= 1/2$) we obtain a familiar result

$$\dot{\rho} = -\frac{\delta}{2}\rho \tag{4.28}$$

The solution for ρ is an exponential

$$\rho \propto \mathrm{e}^{-\frac{\delta}{2}t} \tag{4.29}$$

so that the amplitude or envelope of the oscillator decays at a rate $\delta/2$ as we know that it should using simpler methods.

4.2.3 N coupled harmonic oscillators

We now move on to the system of interest: many coupled oscillators.

As before we create new variables from the rotating frame transformation:

$$\begin{aligned} x &= q_0 = \rho(t)\cos(\omega_0 t + \phi(t)) \\ y &= \dot{q}_0 = -\omega_0\rho(t)\sin(\omega_0 t + \phi(t)) \\ a &= q_i = r_i(t)\cos(\omega_i t + \theta(t)) \\ b &= \dot{q}_i = -\omega_i r(t)\sin(\omega_i t + \theta(t)) \end{aligned} \tag{4.30}$$

Next we apply the differential equations of the system:

$$\begin{aligned} y &= \dot{x} \\ b &= \dot{a} \end{aligned} \tag{4.31}$$

along with equations 4.7 and 4.8

to

$$
\begin{aligned}
\rho^2 &= x^2 + y^2 \\
r_i^2 &= a_i^2 + b_i^2 \\
\\
\omega_0 t + \phi &= \tan^{-1}(-\frac{y}{\omega_0 x}) \\
\omega_i t + \theta_i &= \tan^{-1}(-\frac{b_i}{\omega_i a_i})
\end{aligned}
\tag{4.32}
$$

Below are the equations of motion in the rotating frame for a single electron

$$
\begin{aligned}
\dot{\rho} &= -\frac{\omega_0 \rho}{2Q_0(1-k^2)} + \frac{k\omega_1^2}{1-k^2} r \left[\frac{s_0 s_1}{Q_1} - s_0 c_1\right] \\
\dot{r} &= -\frac{\omega_i r}{2Q_1(1-k^2)} + \frac{k\omega_0^2}{\omega_1(1-k^2)} \rho \left[\frac{s_0 s_1}{Q_0} - c_0 s_1\right] \\
\dot{\phi} &= \frac{\omega_0 k^2}{2(1-k^2)} + \frac{k\omega_1^2}{\omega_0(1-k^2)} \frac{r}{\rho} \left[\frac{c_0 s_1}{Q_1} - c_0 c_1\right] \\
\dot{\theta} &= \frac{\omega_1 k^2}{2(1-k^2)} + \frac{\omega_0^2 k}{\omega_1(1-k^2)} \frac{\rho}{r} \left[\frac{s_0 c_1}{Q_0} - c_0 c_1\right]
\end{aligned}
\tag{4.33}
$$

and the averaging has been lumped into the factors

$$
\begin{aligned}
s_0 s_i &=< \sin(\omega_0 t + \phi)\sin(\omega_i t + \theta_i) >= \frac{\omega_0}{2\pi}\int_{t-\pi/\omega_0}^{t+\pi/\omega_0} \sin(\omega_0 t + \phi)\sin(\omega_i t + \theta_i)\,\mathrm{d}t \\
s_0 c_i &=< \sin(\omega_0 t + \phi)\cos(\omega_i t + \theta_i) >= \frac{\omega_0}{2\pi}\int_{t-\pi/\omega_0}^{t+\pi/\omega_0} \sin(\omega_0 t + \phi)\cos(\omega_i t + \theta_i)\,\mathrm{d}t \\
c_0 s_i &=< \cos(\omega_0 t + \phi)\sin(\omega_i t + \theta_i) >= \frac{\omega_0}{2\pi}\int_{t-\pi/\omega_0}^{t+\pi/\omega_0} \cos(\omega_0 t + \phi)\sin(\omega_i t + \theta_i)\,\mathrm{d}t \\
c_0 c_i &=< \cos(\omega_0 t + \phi)\cos(\omega_i t + \theta_i) >= \frac{\omega_0}{2\pi}\int_{t-\pi/\omega_0}^{t+\pi/\omega_0} \cos(\omega_0 t + \phi)\cos(\omega_i t + \theta_i)\,\mathrm{d}t
\end{aligned}
\tag{4.34}
$$

Weak coupling	$k \ll 1$
loss-less electrons	$Q_1 \gg 1$
On resonance	$\omega_0 = \omega_1 = \omega_i$
"cold" cavity, "hot" electrons	$\rho \ll r$
Arbitrary initial cavity phase	$\phi = 0$

Table 4.3: Simplifying limits for the rotating frame system.

Next I will impose the limits from table 4.3 in order to simplify the model and draw insights about the system.

Mathematically, the phase dynamics for this single particle limiting case obeys

$$\dot{\theta} \simeq 0$$
$$\dot{\phi} \propto -k\omega_o \frac{r}{\rho} c_0 c_1,$$

so that $\dot{\phi} = 0$ when $c_0 c_1 = 0$. Therefore, the oscillator phases will evolve to an equilibrium at

$$\phi - \theta \to \pi/2, 3\pi/2, 5\pi/2 \ldots \tag{4.35}$$

The single particle amplitude equations are reduced to

$$\dot{\rho} \simeq -\frac{\rho\omega_0}{2Q_0(1-k^2)} \pm \frac{kr\omega_i^2}{2(1-k^2)\omega_0}$$
$$\dot{\rho} \simeq -\frac{\rho\omega_0}{2Q_0(1-k^2)}$$

and

$$\dot{r} \simeq -\frac{r\omega_i}{2Q_1(1-k^2)} \mp \frac{k\rho\omega_0^2}{2(1-k^2)\omega_i}$$
$$\dot{r} \simeq \mp \frac{k\rho\omega_0^2}{2(1-k^2)\omega_i}$$

For the N electron problem, the equations of motion are

$$
\begin{aligned}
\dot{\rho} &= -\frac{\rho\omega_0}{2Q_0(1-Nk^2)} + \frac{k}{\omega_0(1-Nk^2)}\sum_{i=1}^{N}\omega_i^2 r_i\left[\frac{s_0 s_i}{Q_i} - s_0 c_i\right] \\
\dot{r}_i &= -\frac{r_i\omega_i}{2Q_i}\left(1+\frac{k^2}{1-Nk^2}\right) + \frac{k\omega_0^2}{\omega_i(1-Nk^2)}\rho\left[\frac{s_0 s_i}{Q_0} - c_0 s_i\right] \\
&\quad + \frac{k^2}{\omega_i(1-Nk^2)}\sum_{j\neq i}^{N}\omega_j^2 r_j\left[-\frac{s_j s_i}{Q_j} + s_i c_j\right] \\
\dot{\phi} &= \frac{\omega_0 N k^2}{2(1-Nk^2)} + \frac{k}{1-Nk^2}\sum_{i=1}^{N}\frac{\omega_i^2 r_i}{\omega_0\rho}\left[\frac{c_0 s_i}{Q_i} - c_0 c_i\right] \\
\dot{\theta}_i &= \frac{\omega_i k^2}{2(1-Nk^2)} + \frac{k\omega_0^2}{\omega_i(1-Nk^2)}\frac{\rho}{r_i}\left[\frac{s_0 c_i}{Q_0} - c_0 c_i\right] + \frac{k^2}{1-Nk^2}\sum_{j\neq i}^{N}\frac{\omega_j^2 r_j}{\omega_i r_i}\left[-\frac{s_j c_i}{Q_j} + c_i c_j\right]
\end{aligned}
\tag{4.36}
$$

By integrating these equations numerically, we confirm the phase predictions of equation 4.35. Figure 4.6 shows the phase and amplitude behaviour for the single particle case. Figure 4.7 shows the same result for $N = 5$ electrons. For the latter case, the phase dynamics is unclear. In the limit of large electron numbers however, equation 4.36 suggests that the cavity phase will evolve such that

$$
\sum_{i=1}^{N} c_0 c_i \to 0 \tag{4.37}
$$

Unfortunately solving for large numbers of electrons in the time domain is not computationally feasible. Inferences about the large N electron cooling time and/or phase dynamics have therefore not been attempted.

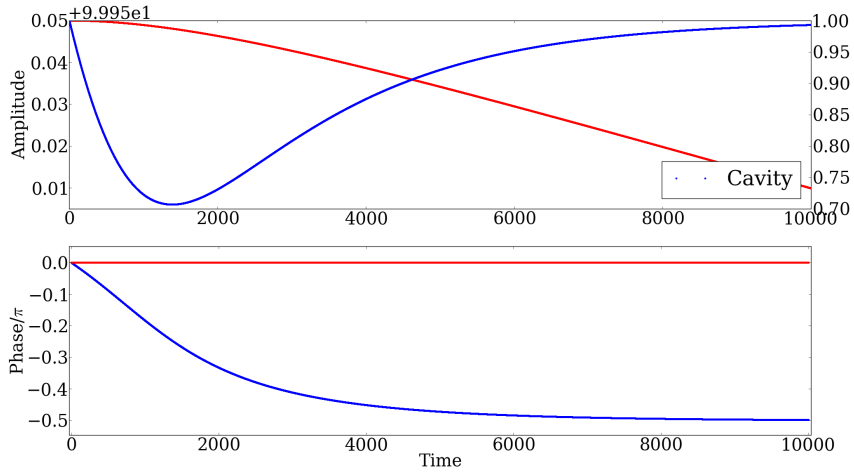

Figure 4.6: The phases and amplitudes of one electron (red, left scale) coupled to a cavity (blue).

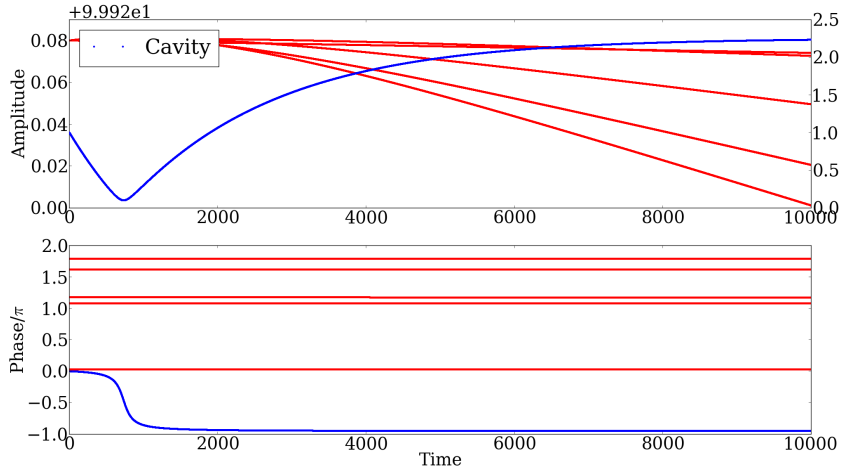

Figure 4.7: The phases and amplitudes of five electrons (red, left scale) coupled to a cavity (blue). The electrons were given uniformly random initial phases (between 0 and 2π)

Chapter 5

Laser Pass - Microwave Stop Tubes

The ALPHA apparatus has been upgraded so as to include apertures which allow lasers access to the anti-hydrogen region 5.1. These 14.3 mm ID copper tubes act as waveguides and direct the microwave band of room temperature black body radiation towards the cryogenic region of the experiment. In particular this radiation will cause resonant heating of positrons which could result in a devastating reduction in anti-hydrogen production. This chapter describes a design which allows laser light through but which attenuates the unwanted microwave radiation.

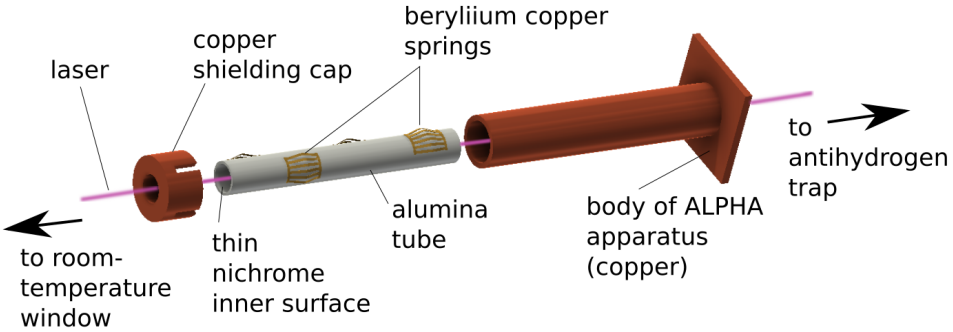

Figure 5.1: An exploded view of a laser pass tube. Optical spectroscopy necessitates use of windows and apertures to allow laser light to interact with trapped anti-hydrogen. These windows allow room temperature blackbody radiation to propagate into the experiment and causes unwanted heating of positron plasmas.

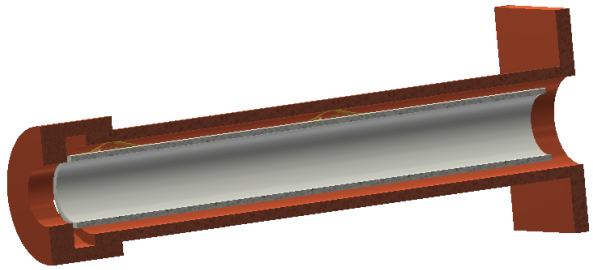

Figure 5.2: An assembled view of a laser pass tube.

5.1 Theory of operation

The design for the laser-pass tubes was inspired by a well known result from classical electromagnetism (see, for example [48]). As in figure 5.3, if a thin resistive sheet is placed a distance of $\lambda/4$ from a conducting plane then a normally incident plane wave will be 100% absorbed if the sheet impedance is matched to free space ($Z_{sheet} = Z_o$).

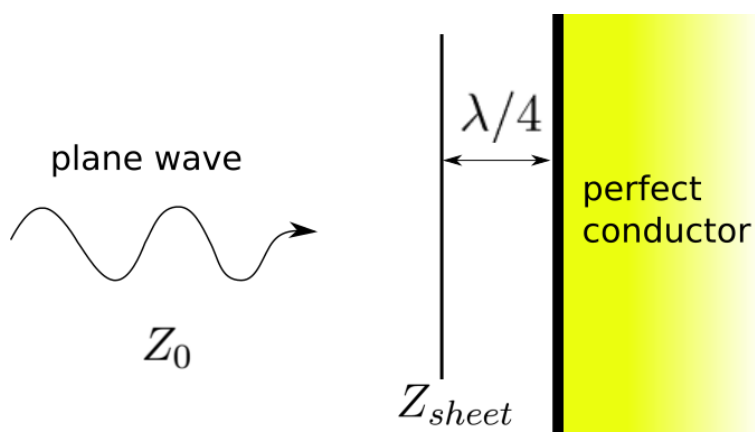

Figure 5.3: A plane wave incident on a good conductor can be perfectly absorbed if a thin sheet with surface impedance (Z_{sheet}) matched to free space (Z_o) is placed a distance $\lambda/4$ from the conductor.

An analogy with transmission line theory explains the mechanism for this absorption. We have already seen in section 3.6 that $\lambda/4$ is a special length

for a transmission line. At that length a short (like the conducting plane in figure 5.3) is transformed into an open circuit. Any object placed at this distance is therefore "in parallel" with an open circuit, or infinite impedance. The plane wave will therefore not use this branch of the "circuit" and see only the impedance presented by the thin resistive sheet.

If the sheet has the impedance of free space (Z_o) then no reflections occur:

$$S_{11} = E_{reflected}/E_{incident} = \frac{Z_{sheet} - Z_o}{Z_{sheet} + Z_o} \tag{5.1}$$

The above geometry achieves 100% absorption only for normal incidence and only at one frequency. However, by modifying to a tubular geometry (figure 5.4 we allow nearly all the radiation to be incident at a glancing angle. The angle of incidence modifies the $\lambda/4$ requirement and complicates the attenuation analysis. A distribution of incident angles will produce a distribution of resonantly absorbed frequencies. Perhaps because of this, we observe that the filter is effective over a wider range of frequencies rather than just one.

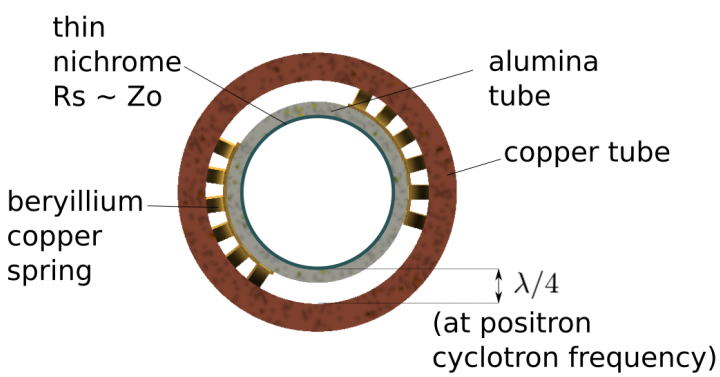

Figure 5.4: The $\lambda/4$ requirement wrapped onto a cylindrical geometry. The gap between the alumina tube is exaggerated to allow visualization of the beryllium-copper springs used for heat contact. The assembled gap is 0.5 mm.

5.2 Fabrication

Thin nichrome films are deposited on the inner face of an alumina tube via a thermal evaporation process.

A tungsten filament tightly wrapped in nichrome wire is threaded through the alumina tube. This apparatus is placed in a moderate vacuum of about 10^{-5} Torr and high a current is run through the filament heating the nichrome. Hot atoms evaporate from the nichrome wire and are deposited on the cooler polished alumina surface.

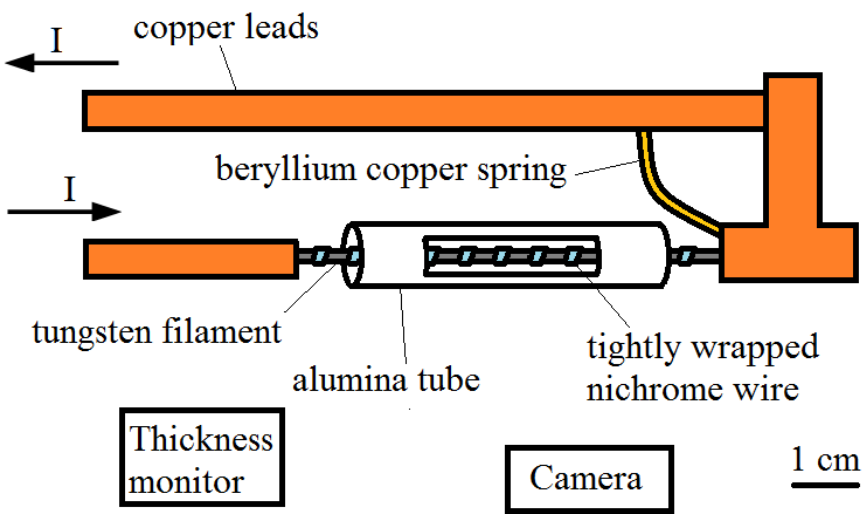

Figure 5.5: A cartoon of the apparatus used to deposit a thin nichrome layer onto the inner surface of a long, narrow alumina tube. A high current is passed through a tungsten filament which evaporates atoms from the nichrome wire.

The narrowness of the alumina tube (inner diameter 11 mm) means that the hot tungsten filament is necessarily very close to the target surface during deposition. This presented a number of challenges to be overcome.

Firstly, the nichrome generally deposited unevenly on the alumina. Normally during vapour deposition, the filament is placed far from the target surface such that the particle flux at the target location is nearly uniform. To mitigate this effect great care was taken to place the filament at the center of the tube: even a small displacement from center results in an uneven

deposition. However, even if carefully centred, the filament will sag or distort its shape and position once heated. To reduce this sagging, the filament was placed under tension using a spring such that once hot and deformable, the filament stretched and roughly maintained its orientation.

Secondly, the alumina tube reflected outgoing thermal radiation back towards the filament creating a furnace effect. This caused the temperature inside the tube to be very sensitive to currents applied to the filament. As a result the filament would often overheat and melt. [10]

Lastly, a quartz crystal oscillator is commonly used as a thickness monitor. The crystal oscillation frequency will change as material is deposited on its surface. If this oscillator is placed near the target sample an accurate measure of the deposition thickness can be obtained. In our geometry however, the alumina target shields the thickness monitor from the nichrome source essentially "blinding" the sensor.

These last two problems were solved by implementing a common web-cam as a sensor. The sensor is capable of detecting relative deposition rates as well as changes in temperature. Figure 5.6 shows the red, green and blue pixel intensities recorded in our camera during a typical nichrome deposition. Abrupt jumps in this signal correspond to increases in current. The subsequent decay in transmitted light intensity indicates nichrome deposition on the inner surface of the alumina tube. As expected, higher decay rates in the transmission signal are associated with higher currents which produce hotter filaments with faster deposition rates.

The absolute thickness of deposited nichrome for these filters is not known. However, the technique could be calibrated to produce such a measurement. The thickness can be inferred from measurements of the nichrome surface resistance and correlated with the deposition time as well as the exponential decay rate of the transmitted light.

[10] Molten nickel is known to attack tungsten [5] quickly, so we suspect that once the nichrome has melted, a nickel tungsten alloy forms. This alloy could have a melting point lower than either nichrome or tungsten. Formation of such an alloy would explain the sudden liquefaction of the filament.

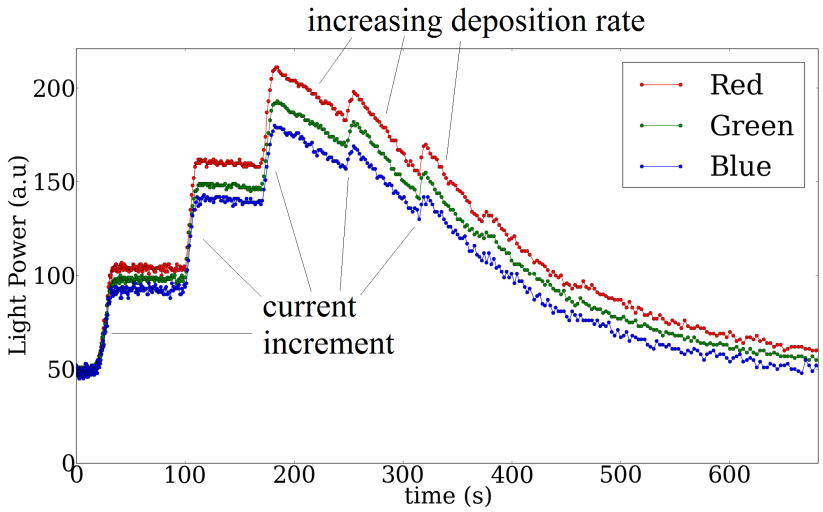

Figure 5.6: CCD pixel values for red, green, and blue are recorded during a thermal evaporation of nichrome onto the inner surface of an alumina tube.

5.3 Microwave attenuation

Microwave transmission through a cylindrical waveguide which incorporates a “laser-pass tube” is characterized using the apparatus shown in figure 5.7. Two large cavities serve as input/output ports for microwave power from a network analyser. The cavities are connected with a cylindrical waveguide which matches laser aperture dimensions at ALPHA and which can house our microwave filtering tube. The cavities are designed to approximate free-space and irregular conductors are placed inside to help randomize the microwave mode structure thereby approximating microwave thermal radiation. The transmitted microwave power is measured both with the microwave filtering tube in place and absent from the apparatus. To determine the effect of the filter, the former scenario is normalized to the latter. The power transmitted through the filter (relative to an empty waveguide) is shown in figure 5.8

Additionally, the surface resistance of the nichrome film deposited on the inner face of one of the alumina tubes was measured using a Ohmmeter. The nichrome surface deposited in 5.6 had a surface resistance of $R_s = 200 \pm 40\Omega$/square. Using standard resistivity values for nichrome and the relationship $\rho = R_s t$ one can approximate the thickness of the nichrome deposition at $t \simeq 7$ nm.

5.4 Thermal conductivity measurement

Absorbing thermal microwaves will cause heating of the ceramic tubes. We must therefore test the thermal conductance of the beryllium copper springs which connect the alumina tube to the surrounding copper tube at 4 K.

We silver epoxy the springs to a mock laser tube made from aluminium. The aluminium tube is inserted into a copper tube with the same inner diameter as at ALPHA. The copper tube is placed in thermal contact with a liquid helium bath at about 4 K. The void between the aluminium tube and copper is pumped to a vacuum pressure of about 10^{-5} Torr. The set up can be viewed in figure 5.9.

Two resistors are fixed with good thermal contact to the aluminium tube. R1 is a "Heater" resistor and R2 is a thermometer. The heater is a thin metal film type resistor and its resistance does not change much with temperature. R1 is a ceramic core resistor whose resistance depends strongly on temperature thus allowing inference of temperature from a resistance measurement.

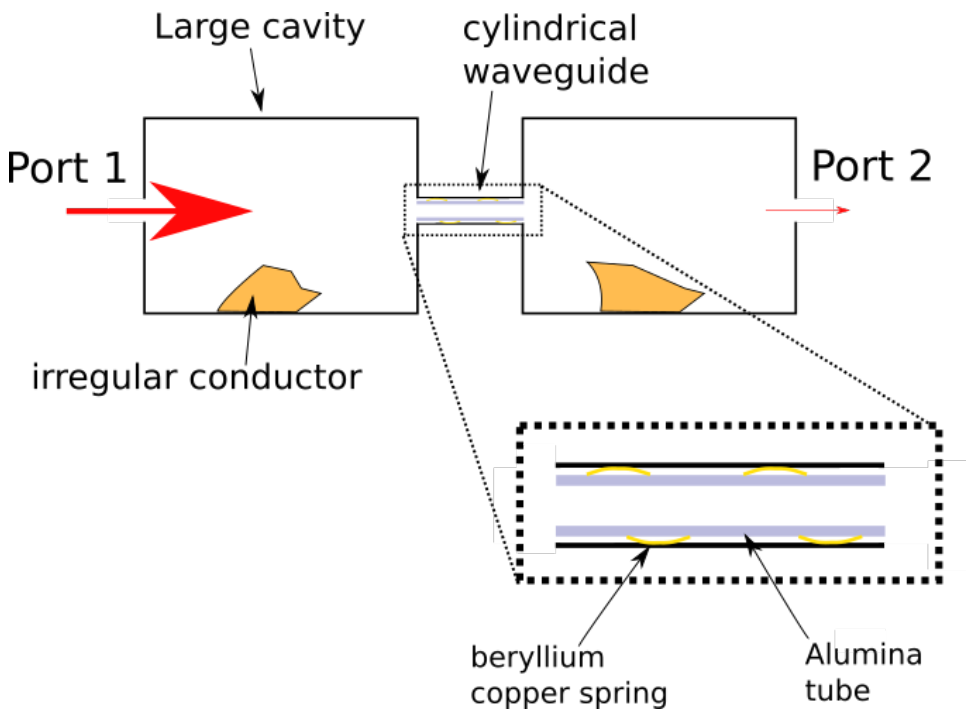

Figure 5.7: The apparatus used to measure microwave transmission through a "laser-pass tube". Two large cavities serve to randomize the microwave mode structure in an attempt to approximate free-space thermal radiation. Transmission through the laser pass tube is normalized to that of the empty waveguide.

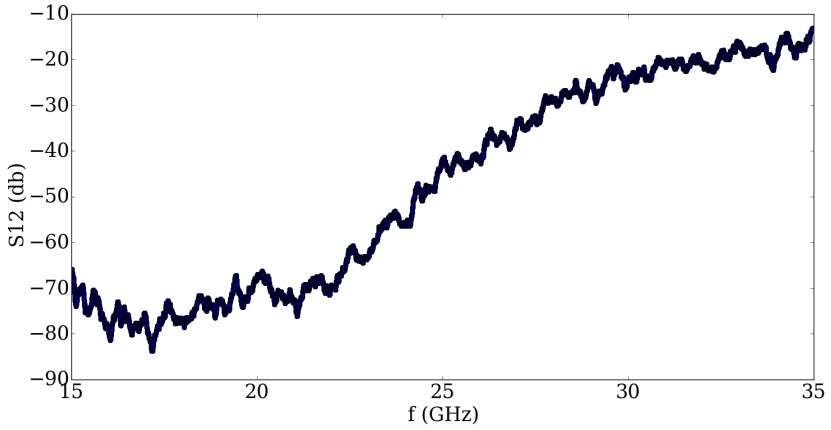

Figure 5.8: The microwave power transmitted through the laser pass tube.

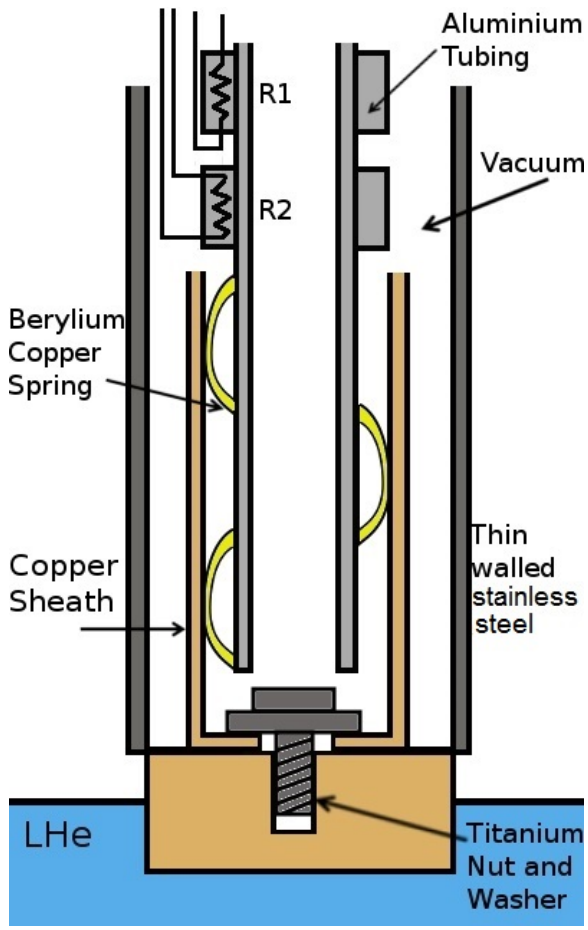

Figure 5.9: Thermal contact experiment set-up.

5.4.1 Results

By applying different voltages to the heater resistor, we vary the heat load to be conducted to the surrounding liquid helium bath via the beryllium copper springs. When a heat load is applied a new, higher, equilibrium temperature is reached. Once in equilibrium we abruptly remove the heat load and the part is allowed to cool to near 4 K. An exponential fit to this temperature decay is performed with the fit function

$$T - 4.2\text{K} = \Delta T_o \mathrm{e}^{-t/\tau} \tag{5.2}$$

where T is temperature, t is the time since the heat load is removed, ΔT_o is the temperature change of the tube at $t = 0$, and τ is the characteristic cooling time of the part.

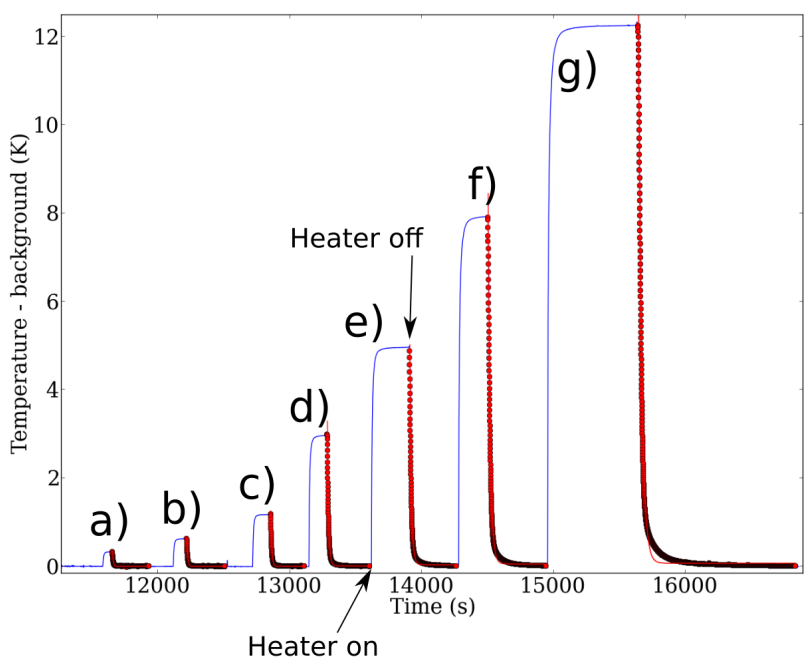

Figure 5.10: Different voltages (heat loads) are applied to the tubes and exponential cooling times are measured from the decay (red dots) which results when the load is turned off and the part comes back to equilibrium with the surrounding liquid helium.

Figure 5.10 shows temperature data for the part while multiple different heat loads are applied and then removed. The results are summarized in table 5.1

Scenario	ΔT_o (K)	τ (s)	Heat load (mW)	Thermal Conductance (mW/K)
a)	0.33	6.2	1.1	3.32
b)	0.62	6.9	2.12	3.42
c)	1.2	7.0	4.33	3.60
d)	3.0	9.1	13.26	4.42
e)	4.9	11.8	27.06	5.52
f)	7.9	16.0	54.25	6.87
g)	12.2	23.5	108.20	8.87

Table 5.1: A summary of the thermal conductance measurements on the laser pass tubes.

These numbers can be compared to the total power incident on the laser aperture according to the Stephan-Boltzmann law

$$P = \sigma T^4 \frac{\Omega}{\pi} \pi r^2 \tag{5.3}$$

where $\sigma = 5.67 \times 10^{-8} \frac{\mathrm{W}}{\mathrm{m^2 K^4}}$ is the Stephan-Boltzmann constant, $T = 300$ K (room temperature), Ω is the solid angle of room temperature surface seen by the laser aperture (conservatively estimated at $\pi/2$), and $r = 11\,\mathrm{mm}$ is the radius of the aperture. The calculation results in $P \simeq 87$ mW. Comparing with the results of table 5.1 we see that the part may heat as much as 10 K if the thermal radiation can be characterized as 300 K radiation. However, given the construction of the ALPHA apparatus, the effective microwave temperature in the region of the tubes is likely to be lower than this.

Chapter 6

Magnetic Electrodes

Great care is taken at ALPHA to remove magnetic materials from the apparatus. Any such material has the potential to become magnetized in some unpredictable way by the many coils regularly turned on or off during a typical antihydrogen production sequence. Field impurities from these materials have the potential to disrupt plasma control, affect antihydrogen dynamics and degrade the magnetic field homogeneity necessary for precision spectroscopy.

This chapter quantifies the magnetic properties of the ALPHA catching trap electrodes. These electrodes are constructed from aluminium and an antistatic coating is achieved with a gold plated surface. Unfortunately gold will not stick well when plated directly onto aluminium, and it is necessary to first plate a intermediate adhesion layer which will stick to both metals. We have discovered that this adhesion layer is magnetic, likely containing nickel.

6.1 Measurement technique

The ALPHA electrodes are placed in a home-built nuclear magnetic resonance (NMR) spectrometer operating at proton resonance frequency of 360 MHz ($\simeq$ 8.5 T) [40]. A 1 mm diameter water NMR probe is placed on the axis of the electrodes and the precession frequency is monitored as a measure of the magnetic field inhomogeneity introduced by the electrode. The spectra were acquired by Carl Michal of the UBC Solid State NMR group using a simple Bloch decay pulse sequence.

By moving the electrodes relative to the probe and monitoring the precession frequency we can map the net magnetic field as a function of position

$$f = \frac{\gamma}{2\pi} B(z) \tag{6.1}$$

With $\gamma = \frac{eg}{2m}$ where g is the gyromagnetic ratio, e the elementary charge, and m the proton mass. For the water probe, the frequency to magnetic field conversion is

$$\Delta B = \frac{f - f_o}{42.58 \times 10^6 \frac{\mathrm{Hz}}{\mathrm{T}}} \tag{6.2}$$

where f_o is the measured precession frequency without electrodes present and ΔB is the field caused by the presence of the electrode.

A sketch of the apparatus is shown in figure 6.1

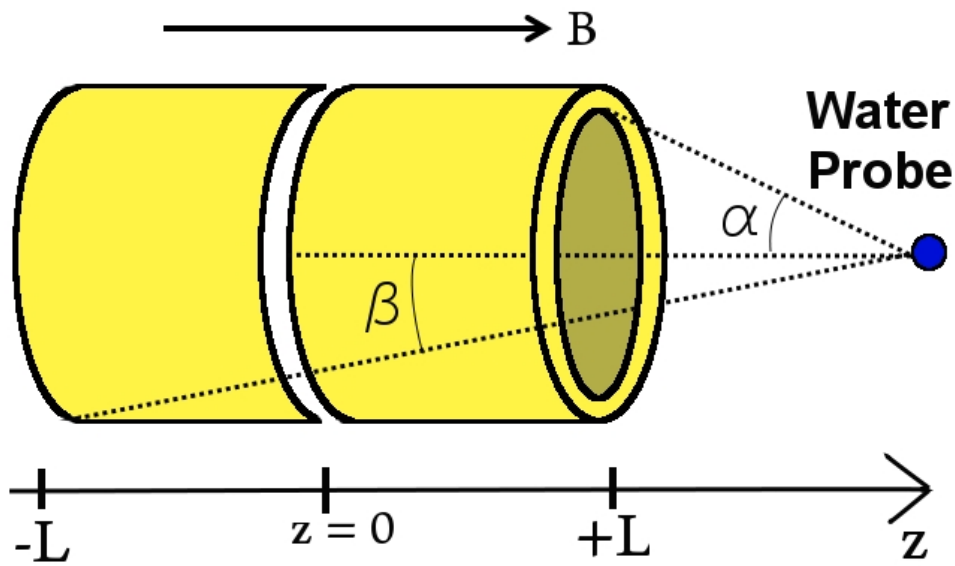

Figure 6.1: A 1 mm diameter water NMR probe is placed on the axis of our electrodes. The precession frequency is used to monitor the magnetic field.

6.2 Model for a thin magnetized tube

A model for the magnetic field of a thin magnetized tube is derived.

The on-axis field for a uniformly magnetized, solid rod is

$$B = \frac{\mu_o M}{2}(\cos\beta - \cos\alpha) \tag{6.3}$$

$$B = \frac{\mu_o M}{2}\left(\frac{z+L}{\sqrt{(z+L)^2 + R^2}} - \frac{z-L}{\sqrt{(z-L)^2 + R^2}}\right) \tag{6.4}$$

For a thin tube, to first order

$$B_{tube} = t\frac{\partial B}{\partial R} = -t\frac{\mu_o M R}{2}\left(\frac{z+L}{[(z+L)^2+R^2]^{3/2}} - \frac{z-L}{[(z-L)^2+R^2]^{3/2}}\right) \tag{6.5}$$

For $R = 2.3$ cm and $L = 1.0$ cm $L = 2.0$ cm (for the case of one and two electrodes respectively) and employing a fit to the two electrode case (there is not enough data for a good fit in the one electrode case) we can plot B_{tube} on top of the data

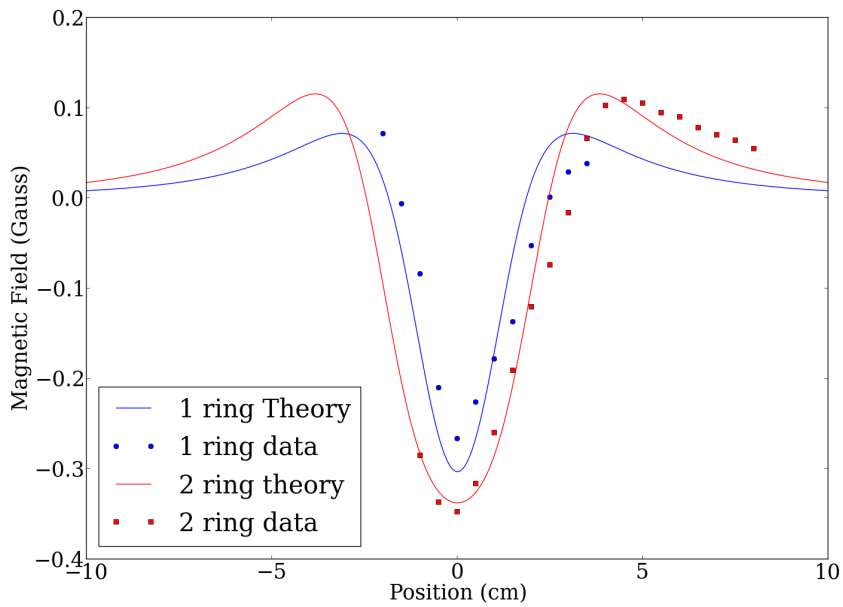

Figure 6.2: The measured extra magnetic field as a function of the axial position of the water probe is fit to the model in equation 6.6.

In figure 6.2 the fit function is

$$B_{tube} = B_o t R\left(\frac{z+L}{[(z+L)^2+R^2]^{3/2}} - \frac{z-L}{[(z-L)^2+R^2]^{3/2}}\right) \tag{6.6}$$

and the result is $B_o t R = 2.4 \pm 0.4$ Gauss·cm^2.

6.3 Approximating the thickness of the nickel strike

Assuming that this field is the result of a thin nickel "strike" layer applied to the aluminium electrodes as a part of the gold plating process, we can determine the thickness of this nickel layer. We take the saturation magnetization for nickel to be

$$B_{sat} = \mu_o M_{sat} = 0.57\,\text{Tesla} \tag{6.7}$$

and use the $z = 0$ field value from equation 6.5

$$B_{tube} = -t\mu_o M_{sat} R \frac{L}{(L^2 + R^2)^{3/2}}. \tag{6.8}$$

Rearranging

$$t = -\frac{B_{tube}}{B_{sat}} \frac{(L^2 + R^2)^{3/2}}{2LR}. \tag{6.9}$$

where the extra factor of 1/2 has been added to account for a strike on each side of the tube (since both sides are gold plated).

From figure 6.4, for two electrodes, we see that $B_{tube} \simeq -0.35 \times 10^{-4}$ Tesla , giving

$$t \simeq 1.9\mu\text{m} \tag{6.10}$$

6.4 Extrapolating to many electrodes

Using equation 6.6 with $z = 0$ and varying L, we can estimate the field inside the magnetized Penning trap at ALPHA. Considering 13 central electrodes with a total length of 27.4 cm ($L = 13.7$ cm) we find

$$B_{tube} = (2.4 \pm 0.4) \times 10^{-2}\text{Gauss} \tag{6.11}$$

The field as a function of tube length is shown in figure 6.4.

6.5 Conclusion

Although the nickel layer seems excessively thick ($\sim 2\mu$m) for the purposes of an adhesion layer between gold and aluminium, the length of the ALPHA Penning trap helps to mitigate the effect by about an order of magnitude.

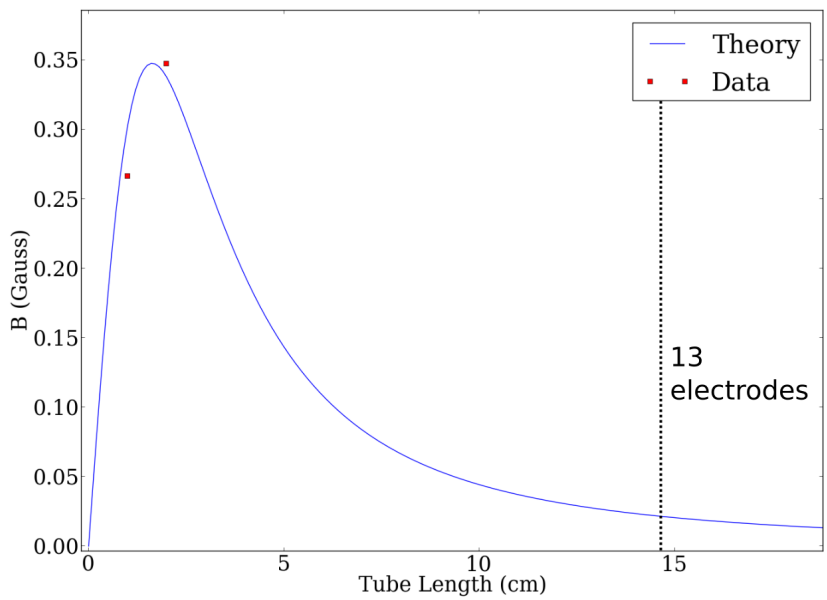

Field vs length of Penning trap.

The expected magnetic field added by such an adhesion layer at ALPHA is ~ 0.05 G. This is to be compared with a recent spin-flip measurement at ALPHA with uncertainties governed by magnetic field inconsistencies [18]. That experiment achieved a spin-flip frequency uncertainty of 100 MHz which results from a ~ 3000 G magnetic field anomaly due to pinning of magnetic flux in nearby superconducting wire. Further, the next most limiting field inhomogeneity is ~ 350 G and results from variance in the field of the magnetic minimum trap. Indeed, a 0.05 G magnetic field is small enough to go unnoticed by a precision hyperfine spectroscopy experiment in the style of [28]. A simple solution to this minor problem may be to use colloidal graphite as an anti-static shielding layer (as in chapter 3) in favour of gold.

Chapter 7

Preliminary Observation of Enhanced Cooling of Electrons at Cavity Resonances

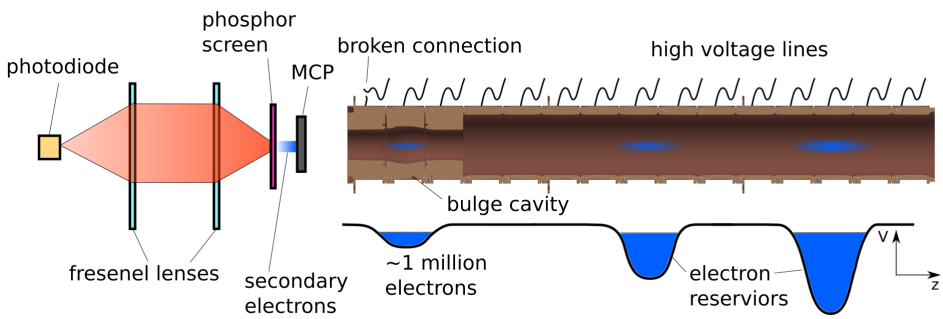

Figure 7.1: A sketch of the Berkeley Experiment with the UBC bulge cavity installed is shown. The broken connection indicated left one of the cavity electrodes floating at some unknown, but seemingly stable voltage. This uncertainty means that the location of the plasma in the cavity is not precisely known.

An experiment is conducted at Berkeley which demonstrates the cooling power of the cavity from chapter 3.

Large plasmas are contained in two storage regions within the Penning trap at Berkeley (see figure 7.1). These reservoirs allow rapid temperature measurements of different plasmas within the bulge cavity. We are therefore able to slowly scan the plasma cyclotron frequency while monitoring the temperature of plasmas which are continually loaded into and ejected from the trap.

A typical sequence goes as follows: A plasma of about one million electrons is loaded from a reservoir into the cavity where cooling occurs. After a specified time (usually 0.5 seconds) this same plasma is ejected onto a

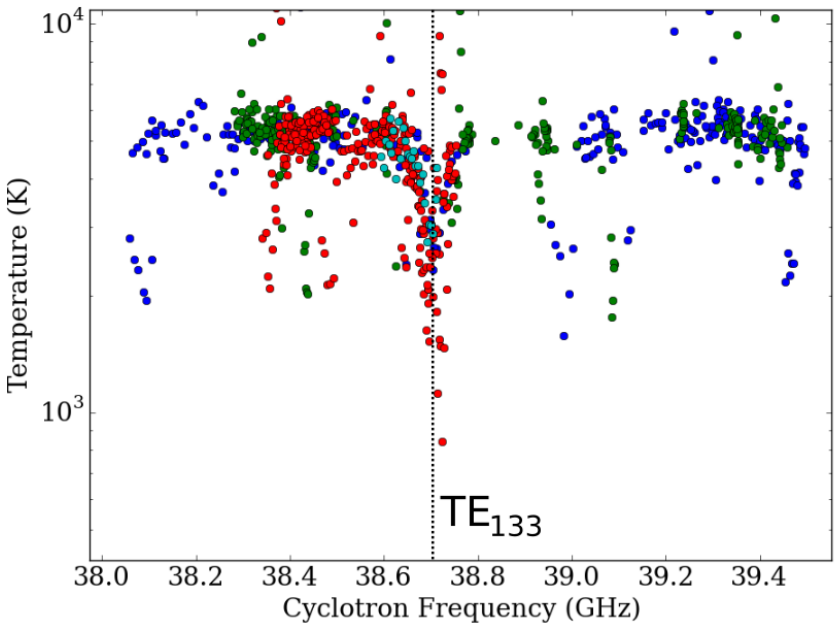

Figure 7.2: Electron plasma temperature is measured as a function of the cyclotron frequency ω_c. When ω_c matches a cavity mode, the temperature is reduced by about an order of magnitude. This particular peak matches the frequency of the TE_{133} mode to better than 1 %. Different field scans (shown in different colours) show that only the temperature drop near the TE_{133} is reproducible.

micro-channel plate (MCP). Secondary electrons leaving the MCP are incident on a phosphor screen which converts these electrons to photons. The emitted light is directed onto a photodiode by Fresnel lenses. From the photodiode signal a plasma temperature can be inferred [11]. The process is then repeated at different cyclotron frequencies.

We observe that, near a cavity resonance, cooling occurs (see figure 7.2).

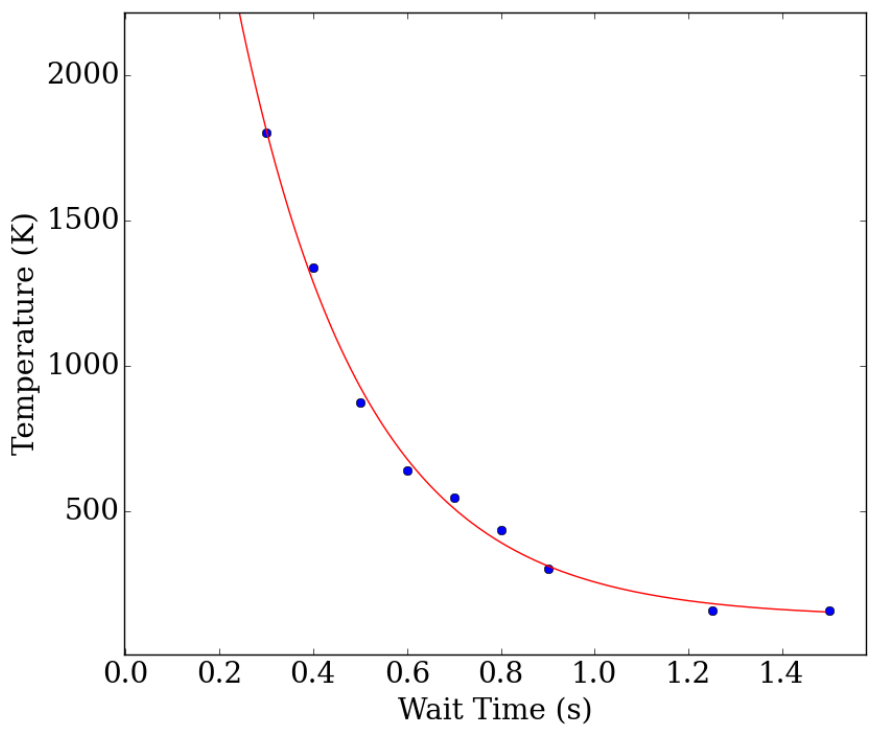

Figure 7.3: Electron plasma are held in the cavity for various times before a temperature measurement is performed. An exponential fit (red) of the form $T(t) = T_o e^{-\Gamma t} + T_f$ allows us to infer the cooling rate.

Once a cavity resonance is identified, we leave the cyclotron frequency constant at the resonance frequency, but vary the amount of time the plasma

[11] The photodiode signal is modelled as resulting from the hottest electrons (which leave the Penning trap first as the electrode voltage is lowered) from a Maxwell-Boltzmann distributed electron plasma. A fit to the photodiode current and the electrode voltage yields the plasma temperature. [47]

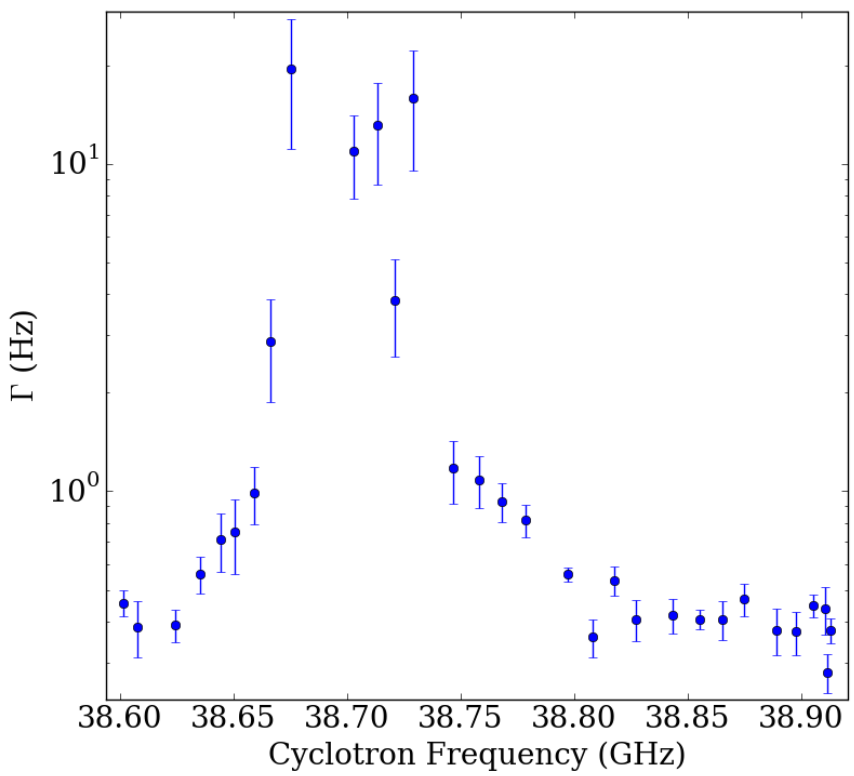

Figure 7.4: Electron plasma cooling rate is measured as a function of the cyclotron frequency ω_c. When ω_c matches a cavity mode, the rate is enhanced. This particular peak matches the frequency of the TE_{133} mode to better than 1 %.

is allowed in the cavity before ejecting to the MCP and performing a temperature measurement. Figure 7.3 shows the plasma temperature versus time spent in the cavity. An exponential fit allows us to infer the plasma cooling rate. Performing this procedure at various cyclotron frequencies in the vicinity of the cavity resonance shows the rate enhancement due to the Purcell effect (figure 7.4).

By scanning the cyclotron frequency and measuring the plasma temperature we were able to identify six cavity resonances with enhanced cooling ability. Figures 7.2, 7.3, and 7.4 focus on the TE_{133} resonance since it was found to have the strongest cooling power. Cooling ability of the remaining detected modes are summarized in table 7.1.

More details on the plasma apparatus and experiment can be found in [47].

Cavity Mode	B (Tesla)	$f_c = \frac{eB}{2\pi m}$ (GHz)	Relative frequency discrepancy %	Cooling Rate Enhancement
TE_{121}	0.775	21.70	-0.18	1.4
TE_{123}	0.91	25.48	-0.12	2
TE_{131}	1.209	33.84	0.21	2
TE_{132}	1.309	36.65	-0.20	4
TE_{133}	1.380	38.64	-0.05	10
TE_{134}	1.443	40.40	-0.35	2.3

Table 7.1: A summary of the observed cooling power of different cavity modes. The relative frequency discrepancy represents the fractional difference between the cyclotron frequency and the measured or simulated cavity resonance frequency (see table 3.1) after a correction for the thermal contraction has been applied.

7.0.1 Outlook

The observed spontaneous emission rate enhancements of order 1 -10 from table 7.1 may seem rather disappointing given that section 2.4 predicted an enhancement factor of $\simeq 1000$. However, one must remember that this prediction was made for the case of a single particle coupled to the cavity. These experiments involved about 10^6 particles and section 4.1.2 predicted that the cavity could not cool more than 10^4 - 10^5 electrons (depending on the mode).

These results come with another flaw: the broken connection to a cavity electrode (see figure 7.1). Since this electrode was floating at some unknown (but seemingly stable) voltage, the exact axial position of any plasma in this experiment is also unknown. This means that the fill factor of section 2.4 needs to be computed as an average weighted by the plasma density. If the plasma happened to be localized near a null in the standing electric field wave, the cooling ability of the cavity would be much reduced.

The results of this chapter, therefore, need to be re-investigated without the hindrance of any floating electrodes within the Penning trap. It is hoped that with greater control over the plasma location, the spontaneous emission rate enhancements provided by this cavity can be improved.

The next step towards increasing the number of trappable antihydrogen atoms at ALPHA involves a cavity redesign. The Penning trap wall at ALPHA is only 1 mm thick and any increase in the thickness would bring matter further into the antihydrogen trapping region. This causes the annihilation of anti-atoms that would otherwise stay trapped and available for experimentation. The loss is very sensitive to this thickness because of the strong radial dependence of the octupole trapping field. An increase in the thickness of only 1 mm would reduce the number of trapped atoms but about 35 %. To overcome this challenge we look to the field of meta-materials where electromagnetic material properties can be chosen by design.

Bibliography

[1] Proceedings of the American Physical Society. *Phys. Rev.*, 69:674–674, Jun 1946.

[2] C. Amole, G.B. Andresen, M.D. Ashkezari, M. Baquero-Ruiz, W. Bertsche, P.D. Bowe, E. Butler, A. Capra, P.T. Carpenter, C.L. Cesar, S. Chapman, M. Charlton, A. Deller, S. Eriksson, J. Escallier, J. Fajans, T. Friesen, M.C. Fujiwara, D.R. Gill, A. Gutierrez, J.S. Hangst, W.N. Hardy, R.S. Hayano, M.E. Hayden, A.J. Humphries, J.L. Hurt, R. Hydomako, C.A. Isaac, M.J. Jenkins, S. Jonsell, L.V. JÃžrgensen, S.J. Kerrigan, L. Kurchaninov, N. Madsen, A. Marone, J.T.K. McKenna, S. Menary, P. Nolan, K. Olchanski, A. Olin, B. Parker, A. Povilus, P. Pusa, F. Robicheaux, E. Sarid, D. Seddon, S. Seif El Nasr, D.M. Silveira, C. So, J.W. Storey, R.I. Thompson, J. Thornhill, D. Wells, D.P. van der Werf, J.S. Wurtele, and Y. Yamazaki. The {ALPHA} antihydrogen trapping apparatus. *Nuclear Instruments and Methods in Physics Research Section A: Accelerators, Spectrometers, Detectors and Associated Equipment*, 735(0):319 – 340, 2014.

[3] A. Angelopoulos, A. Apostolakis, E. Aslanides, G. Backenstoss, P. Bargassa, O. Behnke, A. Benelli, V. Bertin, F. Blanc, P. Bloch, P. Carlson, M. Carroll, E. Cawley, M.B. Chertok, M. Danielsson, M. Dejardin, J. Derre, A. Ealet, C. Eleftheriadis, W. Fetscher, M. Fidecaro, A. Filipcic, D. Francis, J. Fry, E. Gabathuler, R. Gamet, H.-J. Gerber, A. Go, A. Haselden, P.J. Hayman, F. Henry-Couannier, R.W. Hollander, K. Jon-And, P.-R. Kettle, P. Kokkas, R. Kreuger, R. Le Gac, F. Leimgruber, I. MandiÄ, N. Manthos, G. Marel, M. MikuÅŸ, J. Miller, F. Montanet, A. Muller, T. Nakada, B. Pagels, I. Papadopoulos, P. Pavlopoulos, G. Polivka, R. Rickenbach, B.L. Roberts, T. Ruf, M. SchÃfer, L.A. Schaller, T. Schietinger, A. Schopper, L. Tauscher, C. Thibault, F. Touchard, C. Touramanis, C.W.E. Van Eijk, S. Vlachos, P. Weber, O. Wigger, M. Wolter, D. Zavrtanik, and D. Zimmerman. K0 $\bar{K}0$ mass and decay-width differences: CPLEAR evaluation . *Physics Letters B*, 471(2â3):332 – 338, 1999.

[4] M.P. Augustine. Transient properties of radiation damping. *Progress in Nuclear Magnetic Resonance Spectroscopy*, 40:111, 2002.

[5] M. Banning. Neutral density filters of Chromel A. *Journal of the Optical Society of America (1917-1983)*, 37:686, sep 1947.

[6] I.I. Bigi. CP, T and CPT symmetries at the turn of a new millennium. *Nuclear Physics A*, 692(1â2):227 – 242, 2001. Sixth Biennial Conference on Low-Energy Antiproton Physics.

[7] M. Boroditsky, R. Vrijen, T.F. Krauss, Roberto Coccioli, Raj Bhat, and E. Yablonovitch. Spontaneous emission extraction and Purcell enhancement from thin-film 2-D photonic crystals. *Lightwave Technology, Journal of*, 17(11):2096–2112, Nov 1999.

[8] Lowell S. Brown and Gerald Gabrielse. Geonium theory: Physics of a single electron or ion in a Penning trap. *Rev. Mod. Phys.*, 58:233–311, Jan 1986.

[9] Lowell S. Brown, Gerald Gabrielse, Kristian Helmerson, and Joseph Tan. Cyclotron motion in a microwave cavity: Possible shifts of the measured electron g factor. *Phys. Rev. Lett.*, 55:44–47, Jul 1985.

[10] M. Charlton, S. Jonsell, L. V. Jorgensen, N. Madsen, and D. P. van der Werf. Antihydrogen for precision tests in physics. *Contemporary Physics*, 49(1):29–41, 2008.

[11] L.E. Davis and P.A. Smith. Q of a coaxial cavity with a superconducting inner conductor. *Science, Measurement and Technology, IEEE Proceedings A*, 138(6):313–319, Nov 1991.

[12] H. G. Dehmelt and F. L. Walls. "Bolometric" technique for the rf spectroscopy of stored ions. *Phys. Rev. Lett.*, 21:127–131, Jul 1968.

[13] Karl H. Drexhage. Interaction of light with monomolecular dye layers. volume 12 of *Progress in Optics*, pages 163 – 232. Elsevier, 1974.

[14] Amole C. et al. In situ electromagnetic field diagnostics with an electron plasma in a penningâmalmberg trap. *New Journal of Physics*, 16(1):013037, 2014.

[15] B. Aubert et al. *hep-ex/0607103*, 2006.

[16] M. Hori et al. Two-photon laser spectroscopy of antiprotonic helium and the antiproton-to-electron mass ratio. *Nature*, 475:484, 2011.

[17] C. Amole et al. ALPHA Collaboration. Experimental and computational study of the injection of antiprotons into a positron plasma for antihydrogen production. *Physics of Plasmas*, 20(0):043510, 2013.

[18] Amole C. et al.(ALPHA collaboration). Resonant quantum transitions in trapped antihydrogen atoms. *Nature*, 483:439, 2012.

[19] Andresen G.B. et al.(ALPHA collaboration). Trapped antihydrogen. *Nature*, 468:673, 2010.

[20] Andresen G.B. et al.(ALPHA collaboration). Confinement of antihydrogen for 1000 seconds. *Nature*, 7:558, 2011.

[21] Nathan Evetts and Walter Hardy. Frequency, bandwidth and Q measurements of TE_{1lm} and TM_{1lm} modes in a replica of the ALPHA stack. *ALPHA Internal Communication*, 2011.

[22] M. S. Fee, S. Chu, A. P. Mills, R. J. Chichester, D. M. Zuckerman, E. D. Shaw, and K. Danzmann. Measurement of the positronium 1 $^3s_1$–2 $^3s_1$ interval by continuous-wave two-photon excitation. *Phys. Rev. A*, 48:192–219, Jul 1993.

[23] Bo Feng, Mingzhe Li, Jun-Qing Xia, Xuelei Chen, and Xinmin Zhang. Searching for CPT violation with cosmic microwave background data from WMAP and BOOMERANG. *Phys. Rev. Lett.*, 96:221302, Jun 2006.

[24] Timothy Peter Friesen. *Probing Trapped Antihydrogen. In Situ Diagnotics and Observations of Quantum Transitions.* PhD thesis, University of Calgary, 2014.

[25] Gerald Gabrielse and Hans Dehmelt. Observation of inhibited spontaneous emission. *Phys. Rev. Lett.*, 55:67–70, Jul 1985.

[26] P. Goy, J. M. Raimond, M. Gross, and S. Haroche. Observation of cavity-enhanced single-atom spontaneous emission. *Phys. Rev. Lett.*, 50:1903–1906, Jun 1983.

[27] D. Hanneke, S. Fogwell Hoogerheide, and G. Gabrielse. Cavity control of a single-electron quantum cyclotron: Measuring the electron magnetic moment. *Phys. Rev. A*, 83:052122, May 2011.

[28] W. N. Hardy, A. J. Berlinsky, and L. A. Whitehead. Magnetic resonance studies of gaseous atomic hydrogen at low temperatures. *Phys. Rev. Lett.*, 42:1042–1045, Apr 1979.

[29] D. J. Heinzen, J. J. Childs, J. E. Thomas, and M. S. Feld. Enhanced and inhibited visible spontaneous emission by atoms in a confocal resonator. *Phys. Rev. Lett.*, 58:1320–1323, Mar 1987.

[30] D. J. Heinzen and M. S. Feld. Vacuum radiative level shift and spontaneous-emission linewidth of an atom in an optical resonator. *Phys. Rev. Lett.*, 59:2623–2626, Dec 1987.

[31] Helmut Hellwig, Robert F.C. Vessot, Martin W. Levine, Paul W. Zitzewitz, D.W. Allan, and D.J. Glaze. Measurement of the unperturbed hydrogen hyperfine transition frequency. *Instrumentation and Measurement, IEEE Transactions on*, 19(4):200–209, Nov 1970.

[32] R. J. Hughes and B. I. Deutch. Electric charges of positrons and antiprotons. *Phys. Rev. Lett.*, 69:578–581, Jul 1992.

[33] Randall G. Hulet, Eric S. Hilfer, and Daniel Kleppner. Inhibited spontaneous emission by a Rydberg atom. *Phys. Rev. Lett.*, 55:2137–2140, Nov 1985.

[34] John D. Jackson. *Classical Electrodynamics Third Edition*. Wiley, 3 edition, August 1998.

[35] W. Jhe, A. Anderson, E. A. Hinds, D. Meschede, L. Moi, and S. Haroche. Suppression of spontaneous decay at optical frequencies: Test of vacuum-field anisotropy in confined space. *Phys. Rev. Lett.*, 58:666–669, Feb 1987.

[36] Claude A. Klein. Electrical properties of pyrolytic graphites. *Rev. Mod. Phys.*, 34:56–79, Jan 1962.

[37] Daniel Kleppner. Inhibited spontaneous emission. *Phys. Rev. Lett.*, 47:233–236, Jul 1981.

[38] Gerhart Lueders. Proof of the TCP Theorem . *Annals of Physics*, 281(1â2):1004 – 1018, 2000.

[39] S. Maury. The Antiproton Decelerator: AD. *Hyperfine Interactions*, 109(1-4):43–52, 1997.

[40] Carl A. Michal, Kesten Broughton, and Elsa Hansen. A high performance digital receiver for home-built nuclear magnetic resonance spectrometers. *Review of Scientific Instruments*, 73(2):453–458, 2002.

[41] Mario Michan. *Implementation of a coherent Lyman-alpha source for laser cooling and spectroscopy of antihydrogen.* PhD thesis, University of British Columbia, 2014.

[42] C. G. Montgomery, Robert H. Dicke, and Edward M. Purcell. *Principles of microwave circuits / edited by C.G. Montgomery, R.H. Dicke, E.M. Purcell.* Peter Peregrinus on behalf of the Institution of Electrical Engineers London, U.K, 1987.

[43] T. J. Murphy and C. M. Surko. Positron trapping in an electrostatic well by inelastic collisions with nitrogen molecules. *Phys. Rev. A*, 46:5696–5705, Nov 1992.

[44] Susumu Noda, Masayuki Fujita, and Takashi Asano. Spontaneous-emission control by photonic crystals and nanocavities. *Nature Photonics*, 1(8):449–458, AUG 2007.

[45] Christian G. Parthey, Arthur Matveev, Janis Alnis, Birgitta Bernhardt, Axel Beyer, Ronald Holzwarth, Aliaksei Maistrou, Randolf Pohl, Katharina Predehl, Thomas Udem, Tobias Wilken, Nikolai Kolachevsky, Michel Abgrall, Daniele Rovera, Christophe Salomon, Philippe Laurent, and Theodor W. Hänsch. Improved measurement of the hydrogen $1s-2s$ transition frequency. *Phys. Rev. Lett.*, 107:203001, Nov 2011.

[46] T. Petrosky, Chu-Ong Ting, and Sterling Garmon. Strongly coupled matter field and nonanalytic decay rate of dipole molecules in a waveguide. *Phys. Rev. Lett.*, 94:043601, Jan 2005.

[47] Alex Povilus. *Cyclotron-Cavity Mode Resonant Cooling in Single Component Electron Plasmas.* PhD thesis, Berkeley, April 2015.

[48] Simon Ramo, John R. Whinnery, and Theodore V. Van Duzer. *Fields and Waves in Communication Electronics.* Wiley, January 1994.

[49] F. Robicheaux. Atomic processes in antihydrogen experiments: a theoretical and computational perspective. *Journal of Physics B: Atomic, Molecular and Optical Physics*, 41(19):192001, 2008.

[50] J. Tan and G. Gabrielse. Synchronization of parametrically pumped electron oscillators with phase bistability. *Phys. Rev. Lett.*, 67:3090–3093, Nov 1991.

[51] J. Tan and G. Gabrielse. Parametrically pumped electron oscillators. *Phys. Rev. A*, 48:3105–3122, Oct 1993.

[52] Ted Pella Inc. *Graphite Aerosol*, 4 2015.

[53] R. S. Van Dyck, F. L. Moore, D. L. Farnham, P. B. Schwinberg, and H. G. Dehmelt. Microwave-cavity modes directly observed in a Penning trap. *Phys. Rev. A*, 36:3455–3456, Oct 1987.

[54] Robert S. Van Dyck, Paul B. Schwinberg, and Hans G. Dehmelt. New high-precision comparison of electron and positron g factors. *Phys. Rev. Lett.*, 59:26–29, Jul 1987.

[55] R.A. Waldron. *The Theory of Waveguides and Cavities*. Maclaren, 1967.

[56] Herbert Walther, Benjamin T. H. Varcoe, Berthold-Georg Englert, and Thomas Becker. Cavity quantum electrodynamics. *Reports on Progress in Physics*, 69(5):1325, 2006.

[57] C. Weisbuch, H. Benisty, and R. Houdre. Overview of fundamentals and applications of electrons, excitons and photons in confined structures. *Journal of Luminescence*, 85(4):271 – 293, 2000.

[58] W. D. White, J. H. Malmberg, and C. F. Driscoll. Resistive-wall destabilization of diocotron waves. *Phys. Rev. Lett.*, 49:1822–1826, Dec 1982.

[59] D. J. Wineland and H. G. Dehmelt. Principles of the stored ion calorimeter. *Journal of Applied Physics*, 46(2):919–930, 1975.

[60] E. Yablonovitch, T. J. Gmitter, and R. Bhat. Inhibited and enhanced spontaneous emission from optically thin AlGaAs/GaAs double heterostructures. *Phys. Rev. Lett.*, 61:2546–2549, Nov 1988.

[61] Eli Yablonovitch. Inhibited spontaneous emission in solid-state physics and electronics. *Phys. Rev. Lett.*, 58:2059–2062, May 1987.

[62] Yoshihisa Yamamoto, Susumu Machida, and G. Bjork. Micro-cavity semiconductor lasers with controlled spontaneous emission. *Optical and Quantum Electronics*, 24(2):S215–S243, 1992.

Appendix A

Detailed Drawings of a Bulge Resonator

Detailed drawings of the bulge resonator are presented.

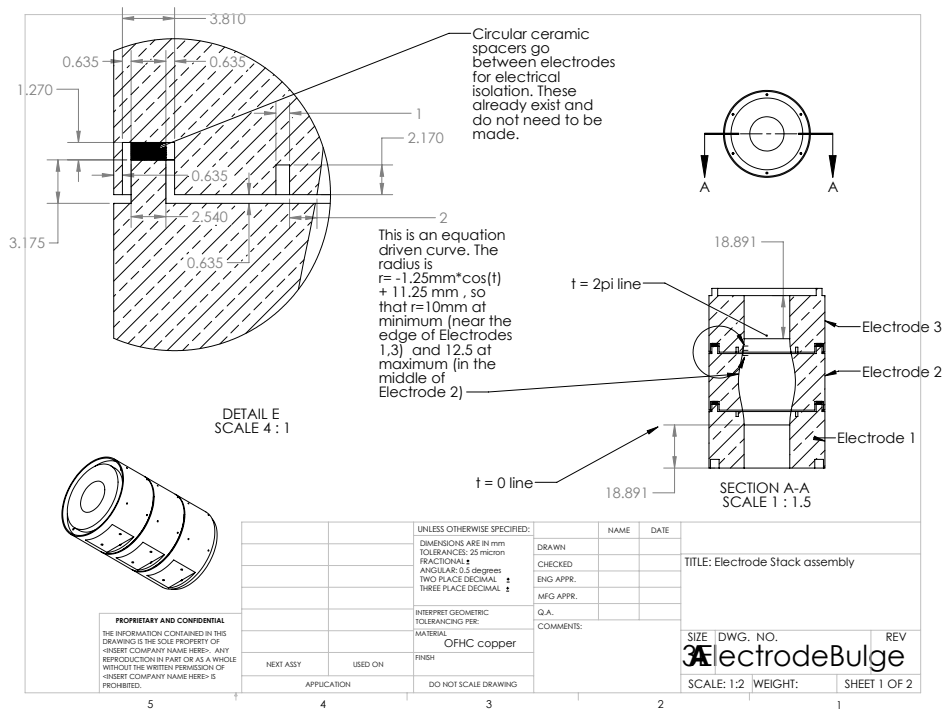

Figure A.1: Detailed bulge cavity drawings

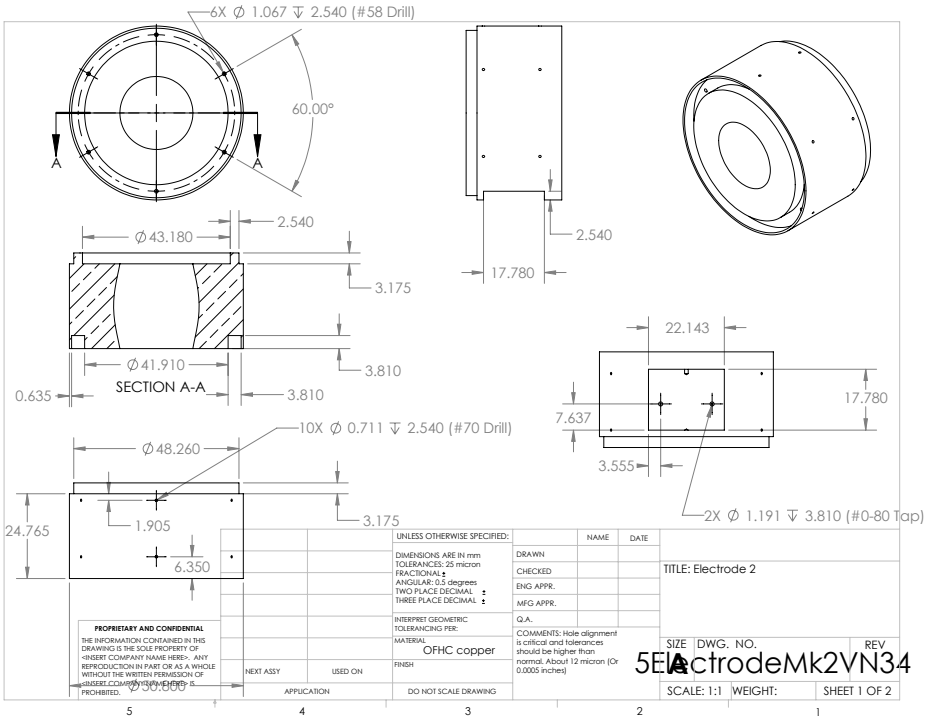

Figure A.2: Detailed drawings of single electrode within bulge cavity.

Appendix B

A Model for Effective Sheet Resistance of Multiple Thin Conducting Layers

B.1 Complex poynting theorem

The time averaged work done by fields on sources (each with assumed time dependence $\mathrm{e}^{i\omega t}$is

$$\frac{1}{2}\int \vec{J}^* \cdot \vec{E}\,\mathrm{d}^3x \tag{B.1}$$

using the complex Maxwell Equations for harmonic fields we have

$$\nabla \times \vec{E} = i\omega\vec{B} \tag{B.2}$$

$$\nabla \times \vec{H} + i\omega\vec{D} = \vec{J} \tag{B.3}$$

together with the vector identity

$$\nabla \cdot (E \times H) = H \cdot (\nabla \times \vec{E}) - E \cdot (\nabla \times \vec{H}) \tag{B.4}$$

Equation B.1 becomes

$$\begin{aligned}
\frac{1}{2}\int \vec{J}^* \cdot \vec{E}\,\mathrm{d}^3x &= \frac{1}{2}\int \vec{E} \cdot (\nabla \times \vec{H}^* - i\omega\vec{D}^*)\,\mathrm{d}^3x \\
&= \int -\nabla \cdot \frac{(\vec{E} \times \vec{H}^*)}{2} - \frac{i\omega}{2}(\vec{E} \cdot \vec{D}^* - \vec{B} \cdot \vec{H}^*)\,\mathrm{d}^3x \\
&= \int -\nabla \cdot \vec{S} - i2\omega(w_e - w_m)\,\mathrm{d}^3x
\end{aligned} \tag{B.5}$$

where the electric and magnetic energy densities are

$$w_e = \frac{1}{4}\vec{E} \cdot \vec{D}^* \tag{B.6}$$

$$w_m = \frac{1}{4}\vec{B} \cdot \vec{H}^* \tag{B.7}$$

Conservation of energy is then expressed via the complex Poynting theorem:

$$\frac{1}{2}\int \vec{J}^* \cdot \vec{E}\,\mathrm{d}^3x - i2\omega \int w_e - w_m\,\mathrm{d}^3x + \oint \vec{S} \cdot \vec{n}\,\mathrm{d}a = 0 \tag{B.8}$$

B.2 Resistance and reactance

For a coaxial input (with current I and voltage V) to a general two terminal, linear, passive electromagnetic system (with impedance Z) as in figure B.1, the power dissipation is

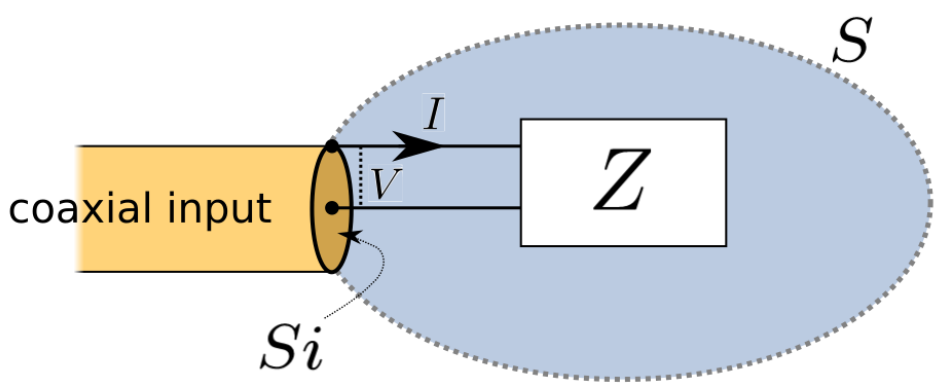

Figure B.1: An arbitrary surface S surrounding a general two terminal electromagnetic structure. $\vec{n}$ is the unit normal vector outwards from the surface, and S_i is an input surface occupied by the coaxial line.

$$\frac{1}{2}I^*V = \frac{1}{2}\int \vec{J}^* \cdot \vec{E}\,\mathrm{d}^3x - i2\omega \int w_e - w_m\,\mathrm{d}^3x + \oint_{S-Si} \vec{S} \cdot \vec{n}\,\mathrm{d}a. \tag{B.9}$$

With $V = ZI$ and $Z = R - iX$, the real and imaginary parts of Equation B.9 give us the resistance and reactance (R, X) in terms of field quantities.

$$R = \frac{1}{|I|^2}\mathrm{Re}\left[\int \vec{J}^* \cdot \vec{E}\,\mathrm{d}^3x - i4\omega \int w_e - w_m\,\mathrm{d}^3x + 2\oint_{S-Si} \vec{S}\cdot\vec{n}\,\mathrm{d}a\right] \quad \text{(B.10)}$$

and

$$X = \frac{1}{|I|^2}\mathrm{Im}\left[\int \vec{J}^* \cdot \vec{E}\,\mathrm{d}^3x - i4\omega \int w_e - w_m\,\mathrm{d}^3x + 2\oint_{S-Si} \vec{S}\cdot\vec{n}\,\mathrm{d}a\right] \quad \text{(B.11)}$$

The last term in Equations B.9, B.10 and B.11 relates to escaping radiation and can usually be neglected in the low frequency limit. However, for the case of our bulge cavity, this term represents the dominate loss mechanism: leakage out the open ends of the resonator.

Disregarding this for the moment, the expressions for R and X can be approximated in the low frequency limit

$$R = \frac{1}{|I|^2}\int \sigma|E|^2\,\mathrm{d}^3x \quad \text{(B.12)}$$

$$X = \frac{4\omega}{|I|^2}\int (w_e - w_m)\,\mathrm{d}^3x \quad \text{(B.13)}$$

As a side note, dropping the second term in equation B.10 will always be valid at a cavity resonance since the resonance condition can be expressed as $w_e = w_m$ [42].

Up to now the treatment has followed Jackson Section 6.9 [34]. We now look to combine this expression for R with the known solutions for electromagnetic fields near a conducting surface.

B.3 Sheet resistance for a metallic plane

For some tangential magnetic field (H_o) outside a conducting semi-infinite plane occupying $z \geq 0$ the magnetic field inside the metal is

$$H_c = H_o \mathrm{e}^{-z/\delta}\mathrm{e}^{iz/\delta} \quad \text{(B.14)}$$

where $\delta = \sqrt{\frac{2}{\omega\mu\sigma}}$ is the skin depth and σ is the conductivity. Neglecting the displacement current in the conductor as well as x and y derivatives within the ∇ operator, the electric field is found according to

$$\sigma\vec{E}_c = \nabla \times \vec{H}_c \quad \text{(B.15)}$$

$$\vec{E_c} = \sqrt{\frac{\mu\omega}{2\sigma}}(1-i)(\vec{n}\times\vec{H_o})\mathrm{e}^{-z/\delta}\mathrm{e}^{iz/\delta} \tag{B.16}$$

$$|E_c|^2 = \frac{2}{\sigma^2\delta^2}(\vec{n}\times\vec{H_o})^2\mathrm{e}^{-2z/\delta} \tag{B.17}$$

Inserting equation B.17 into equation B.12 and integrating from zero to infinity we obtain a comforting result

$$\begin{aligned}\frac{\mathrm{d}R}{\mathrm{d}A} = Rs &= \frac{(\vec{n}\times\vec{H_o})^2}{|I|^2}\int_0^\infty \frac{2\sigma\mathrm{e}^{-2z/\delta}}{\sigma^2\delta^2}\,\mathrm{d}z \\ &= \frac{2}{\sigma\delta^2}\left[\frac{\mathrm{e}^0-\mathrm{e}^{-\infty}}{2/\delta}\right] \\ &= \frac{1}{\sigma\delta} \\ &= \frac{\rho}{\delta}\end{aligned} \tag{B.18}$$

B.4 Sheet resistance for layered thin metals

Figure B.2: A thin layer of material 1 on top of a thick (semi-infinite) layer of material 2.

We now apply expression B.12 to the case of Figure B.2 : one thin metal (of thickness ξ, conductivity σ_1 and skin depth δ_1) on top of a thick (semi-infinite) metal plane (of conductivity σ_2 and skin depth δ_2). We may write

$$
\begin{aligned}
Rs &= \frac{(\vec{n}\times\vec{H_o})^2}{|I|^2}\left[\int_0^{\xi}\frac{2\mathrm{e}^{-2z/\delta_1}}{\sigma_1\delta_1^2}\,\mathrm{d}z+\int_{\xi}^{\infty}\frac{2\mathrm{e}^{-2z/\delta_2}}{\sigma_2\delta_2^2}\,\mathrm{d}z\right]\\
&= \frac{1-\mathrm{e}^{-2\xi/\delta_1}}{\sigma_1\delta_1}+\frac{1}{\sigma_2\delta_2}(\mathrm{e}^{-2\xi/\delta_2}-\mathrm{e}^{-\infty})\\
&= \frac{1-\mathrm{e}^{-2\xi/\delta_1}}{\sigma_1\delta_1}+\frac{\mathrm{e}^{-2\xi/\delta_2}}{\sigma_2\delta_2}\\
&= R_{s1}(1-\mathrm{e}^{-2\xi/\delta_1})+\mathrm{e}^{-2\xi/\delta_2}R_{s2} \qquad \text{(B.19)}
\end{aligned}
$$

The expression satisfies our expectations for limiting cases. Namely,

$$
\begin{aligned}
\lim_{\xi\to\infty} Rs &= R_{s1}\\
\lim_{\xi\to 0} Rs &= R_{s2} \qquad \text{(B.20)}
\end{aligned}
$$

An effective conductivity can be derived from equation B.19 by setting

$$Rs=\frac{1}{\sigma_e\delta_e}=\sqrt{\frac{\omega\mu}{2\sigma_e}} \qquad \text{(B.21)}$$

and solving for σ_e. After some algebra we arrive at

$$\sigma_e=\frac{\sigma_1\sigma_2}{(\sqrt{\sigma_2}(1-\mathrm{e}^{-2\xi/\delta_1})+\sqrt{\sigma_1}\mathrm{e}^{-2\xi/\delta_2})^2} \qquad \text{(B.22)}$$

Like the surface resistance R_s the effective conductivity still depends on frequency via the skin depths δ_1 and δ_2.

Two cases of primary interest to the experiment will now be explored via direct observation.

B.4.1 Observation

This model is tested using a coaxial resonator as in figure B.3. The center conductor of the resonator is electroplated with thin layers of a second metal and the resonance Q allows us to infer the surface resistance. The Q of such a resonator is [55, 11]

$$Q=\frac{\omega_o\mu_o L\ln(a/b)}{R_{sa}\frac{L}{a}+R_{sb}\frac{L}{b}} \qquad \text{(B.23)}$$

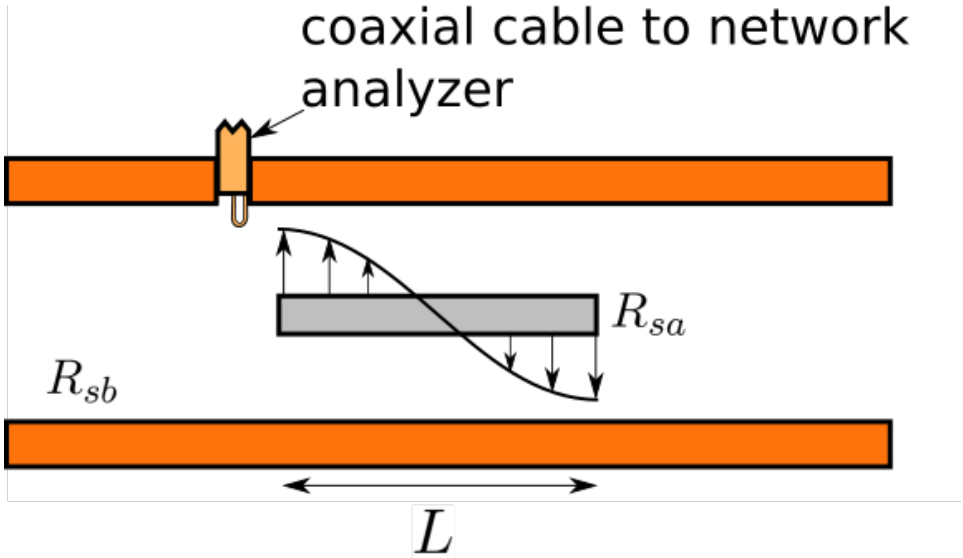

Figure B.3: A short center conductor placed in a long metallic tube will act as a coaxial resonator. The electric fields of the first harmonic are sketched on the center conductor. An inductive loop coupler allows us to measure the frequency and Q of the resonance using a network analyser. Knowledge of the Q allows us to infer the surface resistance of the inner conductor.

where L is the length of the center conductor, a is its radius, R_{sa} is its surface resistance, b is the radius of the outer conductor, R_{sb} is its surface resistance, and $\omega_o/2\pi$ is the mode frequency.

Using B.19 for R_{sa} we can make a prediction for the Q of these modes as a function of the thickness of the electro-deposited top metallic layer on the center conductor. The result, for gold electroplated onto nichrome is in figure B.7. For a nichrome-like alloy plated onto copper, see figure B.8.

B.4.2 Thin gold on thick nichrome

Firstly we inquire about the sheet resistance of a thick layer of nichrome underneath a thin layer of gold (figure B.4). Our aim here is to test the possibility of lowering the Q of a resonant mode (at about 30 GHz) inside our bulge cavity while maintaining good electrostatic shielding for plasmas. The thin gold layer will shield the plasmas from oxide layers on the nichrome that may acquire static charges. However, if the gold is thick enough, it will also shield the relevant microwave mode from excess losses occurring in the

Figure B.4: A thin layer of gold on top of a thick (semi-infinite) layer of Nichrome.

nichrome and thus prevent the lowering of the mode Q. Figures B.5 and B.6 show the predicted effective surface resistance and conductivity for a layer of gold (of thickness z) over top of a thick layer of nichrome.

Figure B.7 shows the measured Q of four different resonance from the cavity of figure B.3 as a function of the thickness of electroplated gold. A fit to the conductivity of gold was allowed since the deposition is likely porous and uneven. The fit conductivity for gold was always 60% - 80% of the accepted value.

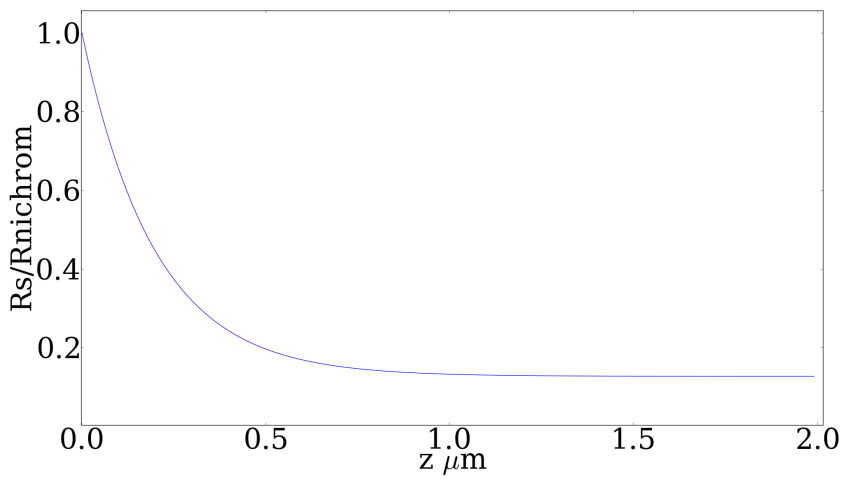

Figure B.5: Effective surface resistance for a layer of gold (thickness z) over top of a thick layer of Nichrome. The result is normalized to the sheet resistance of Nichrome at 30 GHz ($R_{s,nichrom} = 422\text{m}\Omega$) and approaches the sheet resistance of gold ($R_{s,gold} = 54\text{m}\Omega$) for large z. The skin depths of gold and nichrome at 30 GHz are 450 nm and 3.5 μm respectively.

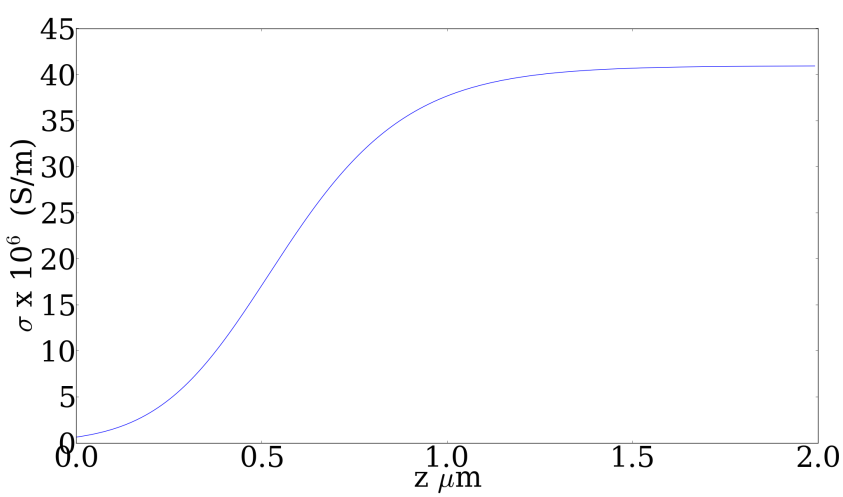

Figure B.6: Effective conductivity for a layer of gold (thickness z) over top of a thick layer of nichrome.

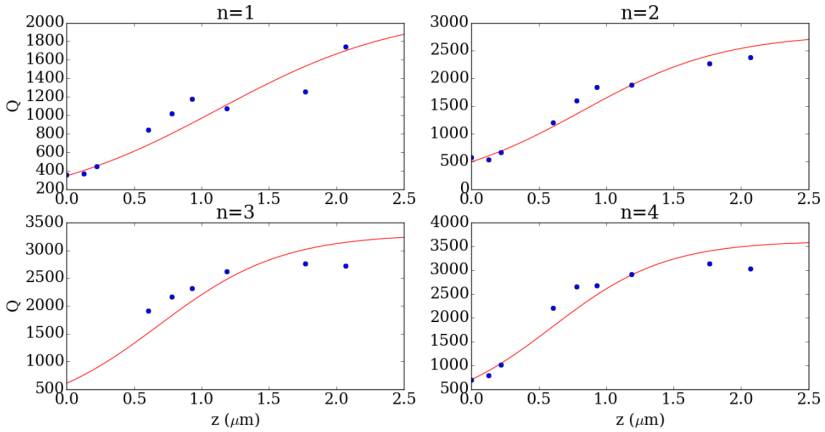

Figure B.7: The measured Q's (blue) for various cavity resonances as a function of the thickness of an electroplated gold layer on the inner conductor (see figure B.3). A fit for the conductivity of gold was allowed since the deposition is likely porous and uneven. The fit conductivity for gold was always 60% - 80% of the accepted value. The best fit models are in red.

B.4.3 Thin nichrome on thick copper

Estimate of alloy conductivity

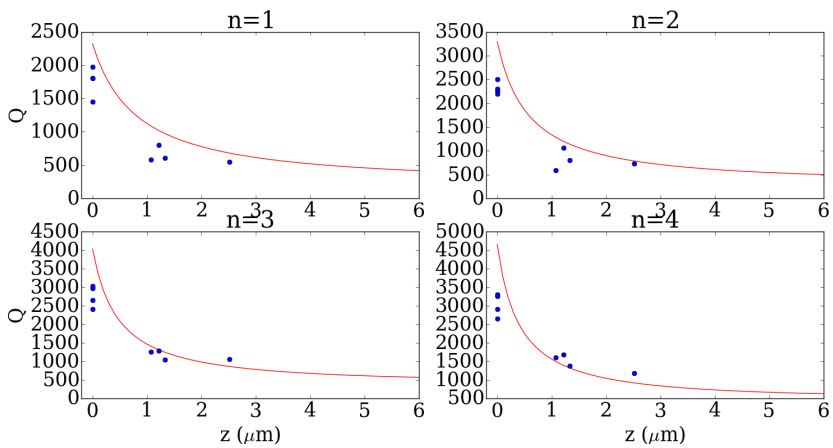

Figure B.8: The measured Q's for various cavity resonances as a function of the thickness of an electroplated "nichrome" layer on a copper inner conductor (see figure B.3). The fit is poor for small z suggesting the presence of a heavy oxide layer on the copper outer conductor.

After the fact it was discovered that our electroplated nichrome actually contained very little chromium (<5 %). However, a measurement of a cavity Q at both room-temperature and liquid nitrogen temperatures gave identical values to 5% . This leads us to believe that the electroplated metal is acting as an electrical alloy.

To estimate the conductivity of this alloy the coaxial resonator of figure B.3 is utilized, this time with a copper center conductor onto which we plate our nichrome-like alloy.

Again the cavity Q's are measured as a function of the thickness of deposited alloy. This data is fit to the theoretical Q (equation B.23) using the our model for effective surface resistance of metallic layers (equation B.19). The best fit conductivity for this alloy is

$$\sigma_{alloy} \simeq 4.5 \times 10^5 \mathrm{S/m}, \tag{B.24}$$

slightly lower than, but more or less in agreement with the accepted value for nichrome: $\simeq 6.6 \times 10^5$S/m. The data along with the best fit model is

shown in figure B.8. The fit is poor for small z indicating that our value for the conductivity of copper ($\sigma_c = 5.8 \times 10^7$S/m) may be too low, possibly due to a heavy oxide layer on the outer conductor.

Both model and data show that a nichrome layer of 5 - 6 μm would be enough to minimize a resonator Q by this method.

Sheet resistance at 10 kHz

We want to check that diocotron waves [58] are not excited as a result of introducing resistive materials to the Penning trap. We model the effective sheet resistance for a surface of nichrome (thickness z) over a thick copper layer. The result is plotted in Figure B.4.3. We see immediately that even a very thick nichrome layer will not change the surface resistance much at 10 kHz.

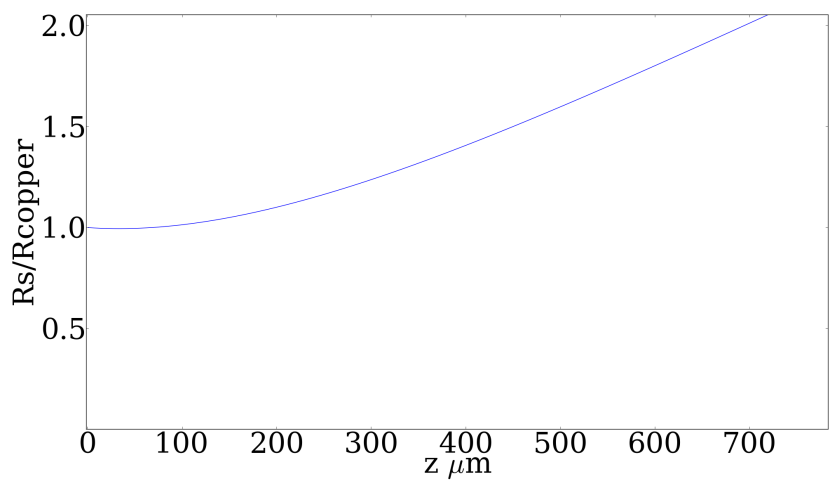

Effective surface resistance for a layer of nichrome(thickness z) over top of a thick layer of Copper. The result is normalized to the sheet resistance of copper at 10 kHz ($R_{s,copper} = 26\mu\Omega$). The skin depths of nichrome and copper at 10 kHz are 6 mm and 650 μm respectively.

B.4.4 Conclusions

To achieve an increased surface resistance at 30 GHz we electroplate about 7μm of the nichrome-like alloy to the inner face of the bulge cavity. The model and data presented in this appendix show that a nichrome layer of 5

- 6 μm is enough to minimize the resonator Q. Q measurements performed at liquid nitrogen temperatures show that the alloy has a temperature independent conductivity about the same as nichrome despite there being very little chromium present in the alloy.

To provide an anti-static shielding layer we utilize colloidal graphite. However, this appendix has investigated the practicality of a gold electrostatic shielding layer. We find that this gold layer must have a thickness less than about 100 nm to maintain resistivity introduced by the underlying alloy.

Meanwhile the surface resistance at 10 kHz would not appreciate considerably due to the presence of the nichrome unless the nichrome layer had a thickness comparable to or greater than a millimetre.